Ultra-wideband based Communications and Localization in Wireless Sensor Networks

Vom Fachbereich Elektrotechnik und Informatik der
Universität Siegen
zur Erlangung des akademischen Grades

Doktor der Ingenieurwissenschaften
(Dr.-Ing.)

genehmigte Dissertation

von

M.Sc. Tech. Gustave Franck Tchere

1. Gutachter: Prof. Dr.-Ing. habil. O. Loffeld
2. Gutachter: Prof. Dr.-Ing. H. Roth
Vorsitzender: Univ.-Prof. Dr. Christoph Ruland

Tag der mündlichen Prüfung: 28.10.2010

Acknowledgments

This work was conducted under the framework of the International Postgraduate Programme (IPP) Multi Sensorics of the Center for Sensorsystems (ZESS) and the Research Center for Multidisciplinary Analysis and Applied System Optimization (FOMAAS) at the University of Siegen.

I would like to take this opportunity to express my greatest thanks to all of you who have supported me in various ways. It is a great pleasure for me to express my sincere gratitude to Prof. Dr.-Ing. habil. Otmar Loffeld, who supervised this work. During the last three years, I have been inspired by his broad knowledge of applied estimation theory, his brilliant insights and his scientific rigorousness. I am also grateful to Prof. Dr.-Ing. Hubert Roth, who is my second supervisor. I have benefitted from his useful comments and advice throughout my thesis work. I would like to extend my gratefulness to Dr.-Ing. Stefan Knedlik for his continuous encouragement and support during the wireless sensor network related activities. It was a pleasure for me working with him.

I am grateful to the thesis committee for their careful reading of this manuscript.

I would like to express my gratitude to all colleagues in the Center for Sensor Systems (ZESS) and members of International Postgraduate Programme (IPP), especially to M.Sc. Pakorn Ubolkosold and M.Sc. Miao Zhang for numerous discussions on both scientific and non-scientific matters and their friendly helps with various problems. I am grateful to Silvia Niet-Wunram, Renate Szabó and Ira Dexling, and for their excellent administrative services.

Finally, I dedicate this thesis to my parents and friends, whose unconditional love and support has been a great source of inspiration to me.

Kurzfassung

Die Hauptbeweggründe für das Verwenden von Ultrabreitband (UWB) Kommunikationssysteme ist ihre Fähigkeit für das Bereitstellen drahtloser Kommunikationen mit hoher Kapazität, sowie die Verwendbarkeit der Technologie, um UWB Signale mit verhältnismäßig niedriger Komplexität einzuführen und zu erzeugen. Nicht kohärente Empfänger ohne die Schätzung des Kanals sind vorgeschlagen worden, um die UWB Technologie attraktiv für die Anwendungen zu machen, in denen niedrige Kosten und niedrige Stromaufnahme eine wichtige Rolle spielen, wie es bei drahtlosen Sensor-Netzen (WSNs) der Fall ist. Die Signalübermittlung der Sendereferenz (TR), in Verbindung mit einem Autokorrelations - Empfänger (AcR) sind in diesem Kontext besonders verwendbar. Die große Bandbreite der UWB Technologie liefert nicht nur die Möglichkeit, um mit einer sehr hohen Datenrate zu übertragen, sondern auch sehr genaue zeitliche und räumliche Informationen, die für exakte Schätzung der Zeitverschiebung verwendet werden können. Das UWB Impuls-Radio (IR) verwendet Sub-Nanosekunden - Impulse, die eine hoch auflösende Fähigkeit in der Zeitdomäne liefern und ist dadurch attraktiv für die genaue drahtlose Lokalisation. In der Tat macht seine Fähigkeit, Mehrwegbestandteile zu beheben möglich, genaue Positionsbestimmung ohne die Notwendigkeit komplizierter Schätzungsalgorithmen zu erhalten. Dieses erleichtert viele Anwendungen wie das Position-bewußte Sensor-Netzwerk.

Diese Doktorarbeit trägt zur Entwicklung der UWB Technologie für Kurzstrecken niedriger bis zu durchschnittlicher Datenraten der WSN Anwendungen bei. TR-UWB Empfänger niedriger Komplexität werden zunächst unter Annahme Gauß'scher Rauschmodelle analysiert, danach werden äquivalente nicht lineare System- und Rauschmodelle betrachtet. Beide Ansätze führen zu der Leistungsanalyse der Bit Fehler, die auch in dieser Dissertation dargestellt werden. Die TR-UWB Systeme wurden als Polynome nichtlinearer Systeme modelliert. Da die Statistiken des Funkkanals in der Systemmodellierung sowie in der Leistungsanalyse verwendet werden, werden passende Kanalmodelle für UWB Impuls-Radiosysteme in dieser Doktorarbeit besprochen.

Weiter wird die Synchronisierung angesprochen. Zu diesem Zweck wird eine neue datengestützte Zeiterfassungstechnik für die Rahmen-Niveau Synchronisierung der DTR-UWB Systeme vorgeschlagen. Sie basiert auf dem Einfügen der parallelen Integration-and-dump Schaltkreise innerhalb der Impuls-Paare der Korrelatorzweige, um die Energieerfassung bei der Präsenz der Zeitverschiebung beträchtlich zu verbessern. Außerdem wird ein einfacher Algorithmus für die Feinsynchronisierung der TR-UWB Systeme, keine Intersymbolstörung annehmend, vorgeschlagen. Er verwendet die Energie, die mit der Symbolrate

gesammelt wird und verringert so beträchtlich die Implementierungskomplexität. Wenn der Taktzeitfehler bekannt ist, sind Schätzungsprobleme der Zeitverschiebung analog zu Entfernungsmessungsproblemen, und der vorgeschlagene Algorithmus kann leicht als neue Abstandmaßtechnik verwendet werden. Es wird in dieser Dissertation gezeigt, dass der Entfernungsansatz eine Lokalisierungsauflösung im Zentimeterbereich mit TR-UWB Systemen bei Datenraten bis zu 5 Mb/s erlaubt.

Executive Summary

The key motivations for using ultra-wideband (UWB) communication systems are their capability for providing high capacity wireless communications, as well as the availability of technology to implement and generate UWB signals with relatively low complexity. Non-coherent receivers with no channel estimation have been proposed to make the UWB technology attractive for applications where low cost and low power consumption are playing an important role, as in the case of wireless sensor networks (WSNs). Transmitted Reference (TR) signaling, in combination with an autocorrelation receiver (AcR) is especially suitable in this context. The large bandwidth of UWB technology does not only provide the possibility to transmit at a very high data rate, but also provides very accurate temporal and spatial information that can be used for precise timing offset estimation. UWB Impulse Radio (IR) uses sub-nanosecond pulses which provide a high resolution capability in the time domain, making it attractive for accurate wireless localization. Indeed, its ability to resolve multipath components makes it possible to obtain accurate location estimates without the need for complex estimation algorithms. This facilitates many applications such as location-aware sensor networking.

This thesis presents several contributions towards developing UWB technology for short-range low to medium data rate WSN applications. First, different low complexity TR-UWB receivers are thoroughly analyzed, using the Gaussian approximation on the noise terms in the receiver statistics, and then using the equivalent system and noise models of these receivers. Both approaches lead to the bit error performance analysis, which is also presented in this thesis. The TR-UWB systems were modelled as polynomial nonlinear systems. Since the statistics of the radio channel are used in the system modelling as well as in the performance analysis, appropriate channel models for UWB impulse radio systems are discussed in this thesis.

Further, synchronization issues are addressed. To this end, a novel data-aided timing acquisition technique for frame-level synchronization of DTR-UWB systems is suggested. It is based on incorporating parallel integration-and-dump circuits within pulse-pair correlator branches to improve considerably the energy capture in the presence of timing offset. Moreover, a simple algorithm for fine synchronization of low complexity TR-UWB systems, assuming no inter-symbol interference, is proposed. It uses energy collected at the symbol rate, thus reducing considerably the implementation complexity. If the hardware clock timing error is known, timing offset estimation problems are analogical to ranging problems, and the proposed algorithm can readily be used as a new distance measurement technique. It is shown, in this thesis, that the proposed ranging approach allows localization accuracy in the centimeter range using TR-UWB systems with data rates up to 5 Mb/s.

Contents

List of Figures

List of Tables

Abbreviations

AcR	Autocorrelation Receiver
ADC	Analog-to-Digital Converter
A-GPS	Aided Global Positioning System
APDP	Average Power Delay Profile
AOA	Angle of Arrival
ASIC	Application Specific Integrated Circuit
BER	Bit Error Rate
BPF	Band Pass Filter
BPPM	Biorthogonal Pulse Position Modulation
BPSK	Binary Phase Shift Keying
CEPT	European Conference of Postal and Telecommunications Administrations
CIR	Channel Impulse Response
CMOS	Complementary MetalOxideSemiconductor
CRC	Cyclic redundancy check
CRLB	Cramér-Rao Lower Bound
DAA	Detection-and-Avoidance
dB	Decibel
DDP	Dominant direct path
DLL	Dynamic-link Library
DP	Dual-Pulse
DTI	Discrete Time-invariant
DTR	Differential Transmitted Reference
DOA	Direction of Arrival
e.g.	Abbreviation for exempli gratia (for example)
EIRP	Equivalent Isotropically Radiated Power
ETSI	European Telecommunications Standards Institute
FBO	Feedback Block-oriented
FCC	Federal Communications Commission
FIFO	First In, First Out
FIR	Finite Impulse Response
FT	Fourier Transform
GHz	Gigahertz
GNSS	Global Navigation Satellite System
GPS	Global Positioning System

Hz	Hertz
I&D	Integrate-and-dump
i.e.	Abbreviation for id est (that is)
IF	Intermediate Frequency
IFI	Infinite Impulse Response
IIR	Inter-frame Interference
IMU	Inertial Measurement Unit
IPP	International Postgraduate Programme
IR	Impulse Radio
ISI	Inter-symbol Interference
kb/s	Kilobit per second
kHz	Kilohertz
LDC	Low-Duty-Cycle
LOS	Line-of-sight
LS	Least Square
LSE	Least Square Error
LTI	Linear Time Invariant
MA	Multi-user Access
MAC	Medium Access Control
MAI	Multiple Access Interference
Mb/s	Megabit per second
MHz	Megahertz
ML	Maximum Likelihood
MSE	Mean Square Error
MU	Multiuser
NBI	Narrowband Interference
NDDP	Non-dominant Direct Path
NLOS	Non-line-of-sight
NMEA	National Marine Electronics Association
OOK	On-off Keying
PAM	Pulse Amplitude Modulation
PC	Personal Computer
pdf	Probability Density Function
PDP	Power Delay Profile
PPM	Pulse Position Modulation
PSD	Power Spectral Density
PVT	Position, Velocity and Time
RF	Radio Frequency
RMS	Root Mean Square
RSS	Received Signal Strength
SI	Spherical-interpolation
SNR	Signal-to-Noise Ratio
TAIP	Trimble ASCII Interface Protocol

TDOA	Time-difference of Arrival
TH	Time Hopping
TOA	Time of Arrival
TR	Transmitted Reference
TSIP	Trimble Standard Interface Protocol
UART	Universal Asynchronous Receiver/Transmitter
UDP	Undetected Direct Path
UWB	Ultra-Wideband
WPAN	Wireless Personal Area Network
w.r.t.	With respect to
WSN	Wireless Sensor Network
ZESS	Center for Sensor Systems

Mathematical Symbols

$\lvert \cdot \rvert$	Absolute value
$\lfloor \cdot \rfloor$	Floor function
$\lceil \cdot \rceil$	Ceiling function
$(\cdot)^T$	Transpose
$\forall$	For all
$\propto$	Proportional to
$\otimes$	Kronecker product
!	factorial
!!	double factorial
$\mapsto$	maps to
c_k^j	TH code sequence of the k^{th} user
∂	Partial differentiation
$\delta(\cdot)$	Dirac delta function
$\mathrm{diag}(\cdots)$	Diagonal matrix
$\mathsf{E}\{\cdot\}$	Expectation
$e^{(\cdot)}$, $\exp(\cdot)$	Exponential
E_b	Bit energy
E_s	Symbol energy
f	Frequency
f_c	Center frequency
$\mathcal{H}$	Homomorphism
$h(t)$	Channel impulse response
$\mathbf{i}_N$	All-ones vector of length N
$\mathbf{I}_N$	Identity matrix of size $N \times N$
$\mathcal{L}\{(\cdot)\}$	Linear operator
$\log(\cdot)$	Logarithm to base 10
$\ln(\cdot)$	Natural logarithm
N_{cr}	Number of pulse-pair correlators
N_f	Number of frames in a symbol
$n(t), \nu(t)$	White Gaussian noise
$Q(\cdot)$	Complementary Gaussian cumulative distribution function
$R_\nu(t)$	Noise autocorrelation function
$r(t)$	Received signal

σ^2	Noise variance
$s_i(t)$	Transmitted signal containing the i^{th} symbol
t	Time
τ	Delay
τ_m	Optimal modulation index in M-ary PPM
t_m	Pulse parameter
T_f	Frame duration
T_m	Channel maximum excess delay
T_s	Symbol duration
T_ω	Pulse duration
T_s	Symbol duration
var$\{\cdot\}$	Variance
$\omega(t)$	Gaussian pulse
$\mathbf{x}$	Vector
$\mathbf{X}$	Matrix
$z[i]$	Decision variable
$\mathbb{Z}$	Field of integers

Chapter 1

Introduction

1.1 Ultra-Wideband Technology

1.1.1 UWB History and Regulatory Issues

The term ***U**ltra-**W**ide**B**and* or *UWB* signal has come to signify a number of synonymous terms such as impulse, carrier-free, baseband, time domain, nonsinusoidal, orthogonal function and large-relative-bandwidth radio/radar signals. According to modern definition [1], UWB characterizes transmission systems with instantaneous spectral occupancy in excess from 500 MHz, or *fractional bandwidth* of more than 20 %. The fractional bandwidth is defined as B/f_c, where $B = f_H - f_L$ denotes the -10 dB bandwidth and center frequency $f_c = (f_H + f_L)/2$ with f_H being the upper frequency of the -10 dB emission point and f_L the lower frequency of the -10 dB emission point. UWB systems with $f_c > 2.5$ GHz need to have a -10 dB bandwidth of at least 500 MHz, while UWB systems with $f_c < 2.5$ GHz need to have a fractional bandwidth of at least 0.20.

Contributions to the development of a field addressing UWB radio frequency (RF) signals commenced in the late 1960's with the pioneering contributions of Harmuth at the Catholic University of America, Ross and Robbins at Sperry Rand Corporation, Paul van Etten at the USAF's Rome Air Development Center and in Russia [2]. The Ross and Robbins (R&R) patents (1972-1987) pioneered the use of UWB signals in a number of application areas, including communications and radar and also using coding schemes. After the 1970s, the only innovations in the UWB field came from improvements in particular instantiations of subsystems, but not in the overall system concept itself, nor even in the overall subsystems' concepts. The basic components were known, e.g., pulse train generators, pulse train modulators, switching pulse train generators, detection receivers and wideband antennas.

In 1994, T.E. Mc Ewan invented the Microwave Impulse Radar (MIR) which provided, for the first time a UWB operating at ultra low power, besides being extremely compact and inexpensive [3]. This was the first UWB radar to operate on only microwatts of battery drain.

The UWB radar and communications approach is a shift in emphasis with respect to the use of the available time-bandwidth-power product. As the signal duration decreases, the

bandwidth increases and the signal-to-noise ratio (SNR) per frequency decreases. Moreover, the SNR per frequency decreases below the threshold of frequency selective receivers, which is a major argument made by UWB proponents that UWB systems are able to operate in the presence of frequency selective receivers without interference. The methods used to reliably receive a UWB signal with such low SNR per frequency are:

- a high sampling rate receiver to capture in a non-synchronous way all the signal energy in a minimum number of sampling bins, summing across all the signal bandwidth which implies a receiver front-end open to that instantaneous ultra-wide bandwidth and thus also open to noise; or
- signal averaging or matched filtering which lowers the data rate; or
- counteracting the low power per frequency by increasing to high signal transmit power, which implies interference to other receivers.

As in the case of more conventional communications systems, the UWB wireless system designer must balance trade-offs among high bandwidth efficiency, low transmission peak power, low complexity, flexibility in supporting multiple rates and reliable performance as expressed in bit error rates. A UWB radar system is more unconventional than a UWB communications system, not only in system components, but also in the physics involved in the signal-target interactions. Indeed, conventional radars use signals longer in distance length than the distance length of the target, thus the target is a point scatterer. In the UWB radar case, the transmitted signal is shorter in distance length than the target, so the target is not a point scatterer.

Even though the concept on which UWB transmission is based is the overlay of low-power signals over existing spectrum and the peaceful coexistence with narrow-band systems already in operation, UWB devices will emit radiation as any other radio system. In order to minimize the level of interference and to coordinate its ordered deployment, a set of regulations is necessary to indicate limits and restrictions in the implementation of this technology and introduction into the real market. The Federal Communications Commission (FCC) in the United States released a huge frequency band 3.1 - 10.6 GHz with equivalent isotropically radiated power (EIRP) below -43 dBm, where UWB radios overlaying coexistent RF systems can operate using low-power ultra-short information bearing pulses. The applications of UWB technology approved by the FCC today include communications (short-range very high speed broadband communications, covert communication links), vehicular radar systems, imaging systems and distance measurement systems (localization at centimeter-level accuracy, precision navigation and asset tracking). The FCC's spectral masks assigned to these applications are listed in Tab. 1.1.

In particular, the FCC's assigned bandwidth and spectral mask for indoor communications is illustrated in Fig. 1.1. Far from being universally accepted and welcomed by everyone, the FCC's initial work raised the discussion levels also in Europe, where very important coexistence studies started in early 2000, first in the CEPT (European Conference of Postal and Telecommunications Administrations) working group SE24 and ETSI (European Telecommunications Standards Institute) working group TG31a, and later also in the newly formed working group TG3. The recommended spectral mask for Europe

Frequency GHz	Indoor Comm.	Hand held Comm.	Low Frq. Imaging	High Frq. Imaging	Med. Frq. Imaging	Vehic. Radar
0.96 - 1.61	-75.3	-75.3	-65.3	-65.3	-53.3	-75.3
1.61 - 1.9	-53.3	-63.3	-53.3	-53.3	-51.3	
1.9 - 1.99		-61.3				
1.99 - 3.1	-51.3			-51.3	-41.3	-61.3
3.1 - 10.6	-41.3	-41.3		-41.3		
10.6 - 22			-51.3			
22 - 29	-51.3	-61.3		-51.3	-51.3	-41.3
29 - 31						-51.3
> 31						-61.3

Table 1.1: FCC spectral mask for UWB systems (EIRP in dBm).

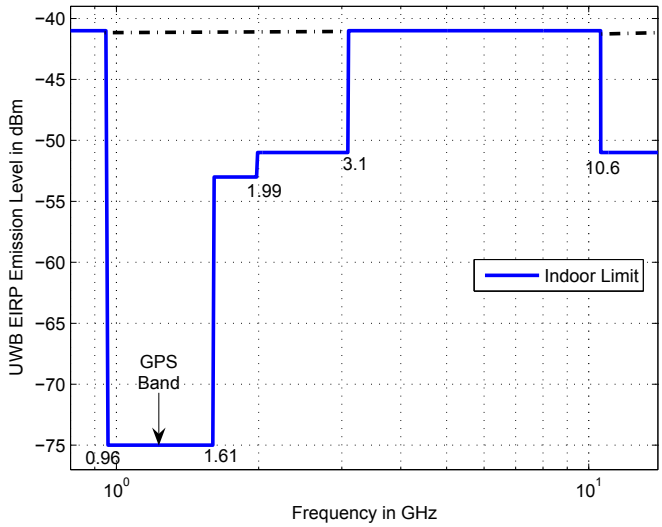

Figure 1.1: FCC spectral mask for indoor commercial applications.

is shown in Fig. 1.2, where power levels are equivalent to those of the FCC regulations in the frequency band 3.1 - 10.6 GHz. However, European regulators have introduced the concept of "*Detection-and-Avoidance*" (DAA) technology to ensure coexistence with existing wireless communications technologies [4]. It means that UWB devices operating in the 3.1-4.2 GHz band should be fitted with DAA systems, which automatically search for nearby broadband wireless signals and then switch frequency to prevent interference. DAA is not required in the 4.2-4.8 GHz band until 2010, and no DAA is required in the 6-10.6 GHz band.

In parallel to the regulatory efforts, another fundamental part of the introduction of this new technology into the market was the definition of an industry inter-operability standard

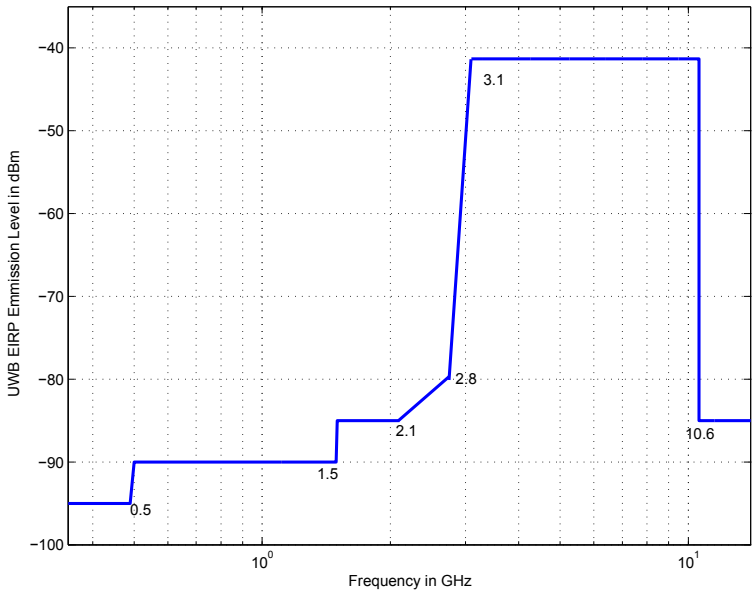

Figure 1.2: Proposed spectral mask for Europe.

based on the best properties of UWB technology. Given the nature of UWB systems, which can be suitable for high-speed links, low to medium data rate and positioning applications, standardization efforts were carried out in parallel in two international standardization groups: the IEEE 802.15.3a (late 2001) and in the IEEE 802.15.4a (late 2003).

1.1.2 Basics of UWB Techniques

Shape and Spectrum of UWB Signals

Impulse Radio (IR) based UWB systems rely on ultra-short sub-nanosecond waveforms that can be free of sine-waves carriers and do not require Intermediate Frequency (IF) processing because they can operate at baseband. Generally adopted spectrum shapers $\omega(t)$ for UWB communications include the *Gaussian pulse*, the *Gaussian monocycle* (first derivative of Gaussian pulse), and the *Gaussian doublet* (second derivative of the Gaussian pulse), as depicted in Fig. 1.3, along with their Fourier Transforms (FT). The reason behind the popularity of these pulses is twofold:

- Gaussian pulses come with the smallest possible time-bandwidth product of 0.5, which maximizes range-rate resolution and
- the Gaussian pulses are readily available from the antenna pattern [5].

Let T_ω be the duration of the transmitted pulse $\omega(t)$. With T_ω at the sub-nanosecond scale, $\omega(t)$ occupies an UWB with bandwidth $B \approx 1/T_\omega$. The mathematical expression of

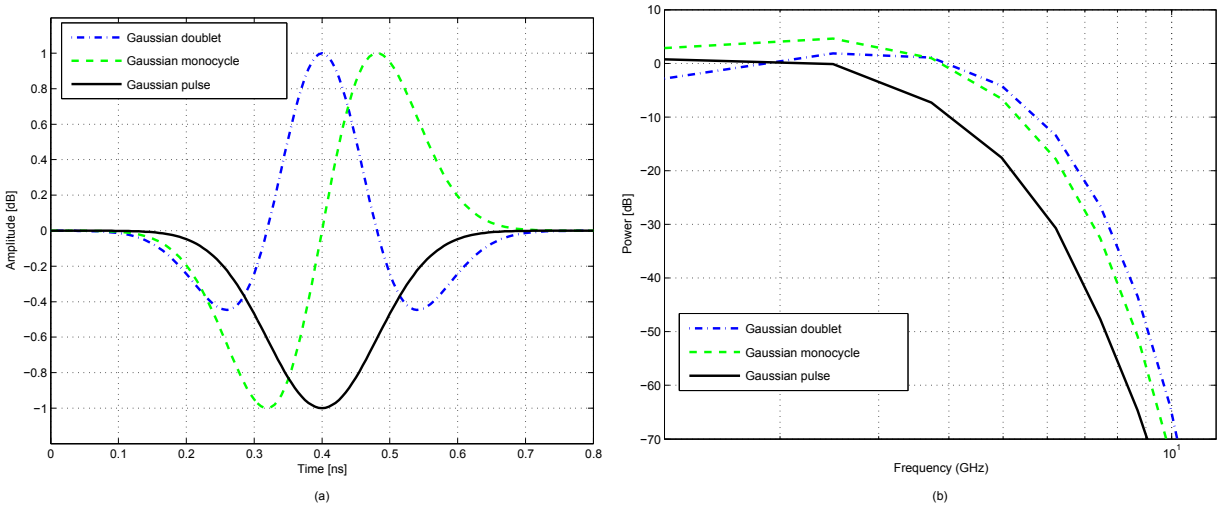

Figure 1.3: (a) Adopted pulse shapes in UWB communications; (b) Fourier transform of the pulse shapes. Pulse duration: $T_\omega = 0.7$ ns.

the Gaussian pulse, Gaussian monocycle and the Gaussian doublet are given, respectively, as

$$\omega_g(t) = K_1 e^{-2\pi(t/t_m)^2}, \tag{1.1}$$

$$\omega_{g_1}(t) = d\omega_g(t)/dt = K_1 \frac{-4\pi t}{t_m^2} e^{-2\pi(t/t_m)^2}, \tag{1.2}$$

and

$$\omega_{g_2}(t) = d^2\omega_g(t)/dt^2 = \frac{-4\pi K_1}{t_m^2}\left(1 - \frac{4\pi t^2}{t_m^2}\right) e^{-2\pi(t/t_m)^2}, \tag{1.3}$$

where t_m is the pulse parameter. It can be seen that by utilizing one of the properties of the pulses (i.e., by differentiating or integrating them) another pulse can be created, with the order of the pulse being one more or less than the original pulse, respectively. In this thesis, the energies associated with the Gaussian pulse and its derivatives are expressed analytically as

$$E_g = \frac{K_1^2 t_m}{2}, \tag{1.4}$$

$$E_{g_1} = \frac{K_1^2 \pi}{t_m}, \tag{1.5}$$

and

$$E_{g_2} = \frac{6\pi^2 K_1^2}{t_m^5}. \tag{1.6}$$

The derivations can be found in Appendix II.

UWB Modulation Techniques

Being real, baseband UWB transmissions neither have to entail frequency modulation nor phase modulation. Consequently, symbol values can be transmitted by modulating the position and/or the amplitude of $\omega(t)$.

In M-ary Pulse Position Modulation (PPM), M distinctly delayed pulses are employed, $\left\{\omega(t-\tau_m)_{m=0}^{M-1}\right\}$, each representing one symbol value. Generally, the modulation indices τ_m are chosen such that $\tau_m = m\tau$ with $\tau \geq T_\omega$, which corresponds to orthogonal PPM. In binary PPM, the delay τ can also be chosen to minimize the correlation $\int \omega(t)\omega(t-\tau)dt$ [6]. As bandwidth efficiency drops with increasing modulation size M, PPM is suitable for power-limited applications. In fact, PPM was almost exclusively adopted in the early development of UWB radios because negating ultrashort pulses were difficult to implement. Biorthogonal pulse position modulation (BPPM) was introduced in [7]. It is shown that N-ary BPPM has better performance than N-ary PPM with the same throughput and half the computational complexity.

Another modulation scheme that does not require pulse negation is the so termed On-Off Keying (OOK), where symbol "1" is represented by transmitting a pulse, and "0" by transmitting nothing. The main advantage of the OOK scheme is its ease of physical implementation.

As pulse negation became easier to implement, Pulse Amplitude Modulation (PAM) attracted more attention. In particular, when $M = 2$, *antipodal* pulses are used to represent binary symbols, as in Binary Phase Shift Keying (BPSK) or *bipolar signaling*. The bit error rate (BER) performance of the BPSK scheme is superior to that of the OOK since OOK has a smaller symbol separation (transmitted symbols 0 and 1) compared to BPSK (transmitted symbols 1 and -1). The different modulations schemes are illustrated in Fig. 1.4 for a bit sequence $b = \{1, 0, 1\}$.

Multiple Access Techniques

To allow for multi-user access (MA) to the UWB channel, Time Hopping (TH) was introduced [6]. With TH, each pulse is positioned with each frame duration T_f according to a user-specific TH sequence c_j^k. Specifically, dividing each frame into N_c chips each of duration T_c, the kth user's TH code $c_j^k \in [0, N_c - 1]$ corresponds to a time shift of $c_j^k T_c$ during the kth frame [8]. A typical TH-PPM transmitted waveform from the kth user is given by

$$s_k(t) = \sum_{j=0}^{+\infty} \omega(t - jT_f - c_j^k T_c - \tau b^k_{\lfloor j/N_f \rfloor}), \tag{1.7}$$

where N_f is the number of pulses transmitted per symbol and $\lfloor x \rfloor$ is the *floor* function of a real number x. It is defined as $\lfloor x \rfloor = \max\{n \in \mathbb{Z} | n \leq x\}$. With TH codes, MA is achieved by altering the pulse position from frame to frame, according to the sequence c_j^k.

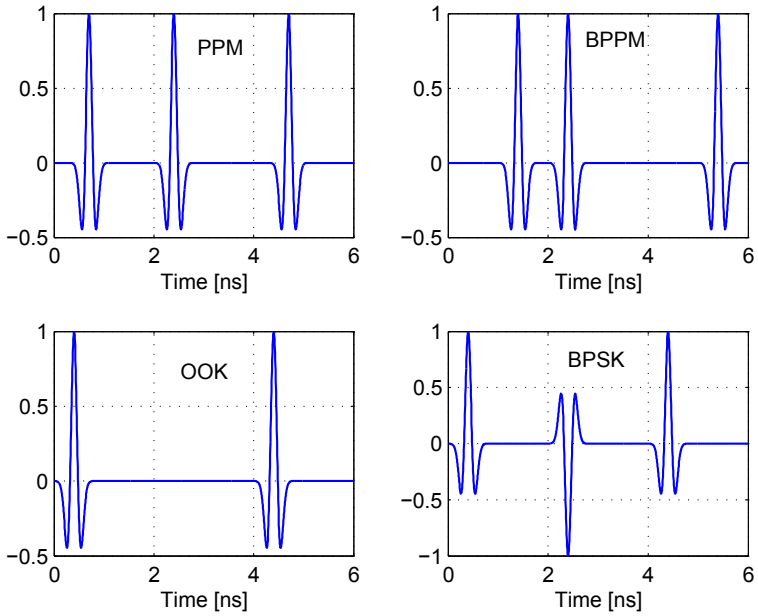

Figure 1.4: UWB modulation schemes.

Fig. 1.5 depicts a TH-PPM transmitted waveform, where $N_f = 10$, $T_f = 10$ ns, $T_c = 0.1$ ns and the code sequence is given by $c_j = \{0, 5.3, 0.4, 3, 7.3, 0.8, 5, 1.6, 1.8, 0\}$, $j = \{0,1,\cdots,9\}$.

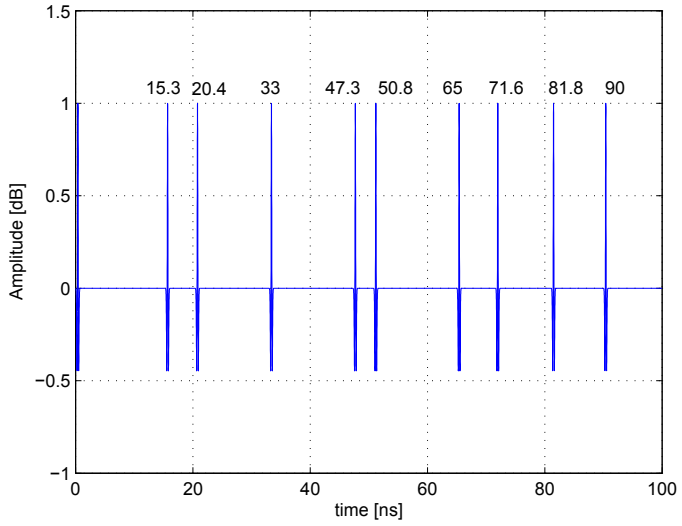

Figure 1.5: Typical TH-PPM waveform.

In addition to facilitating multiple access, spreading codes also shape the transmit spectrum, as shown in Fig. 1.6.

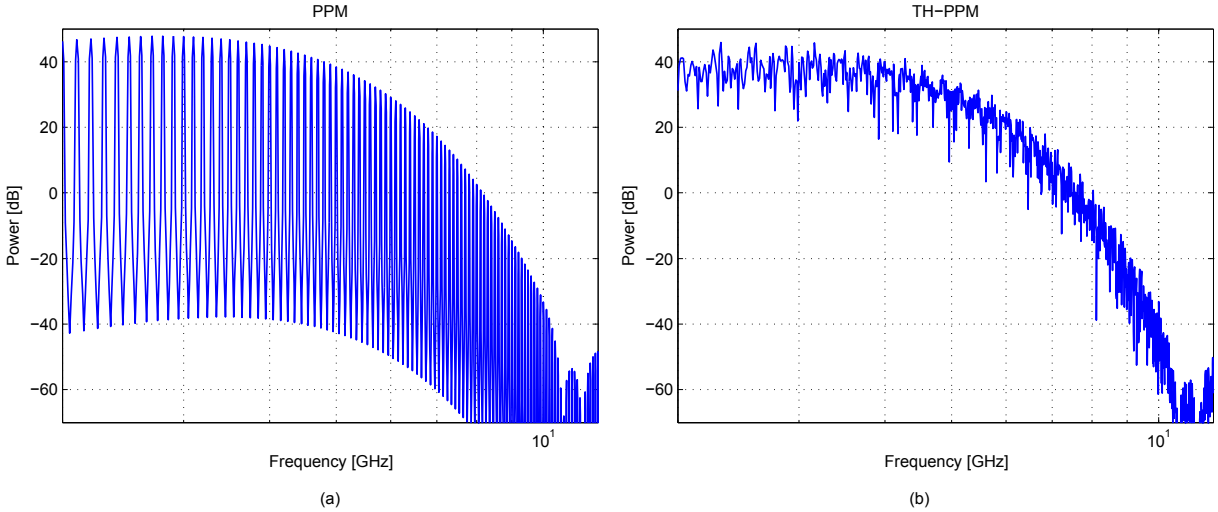

Figure 1.6: Transmit power spectral density (PSD) corresponding to (a) no spreading code, (b) random TH codes.

Applications

- *Wireless Personal Area Networks (WPANs):* Also known as in-home networks, WPANs address short-range (within 10 - 20 m) ad hoc connectivity among portable consumer electronics and communication devices. UWB technology emerges as a promising physical layer candidate for WPANs, because it offers high-rates over short-range, with low cost, high power efficiency and low duty cycle.

- *Wireless Sensor Networks (WSNs):* WSNs consist of a large number of nodes spread across a geographical area. Key requirements for WSNs operating in challenging environments include low cost, low power, and multi-functionality. Emerging applications of UWB are foreseen for sensor networks as well. Such networks combine low to medium rate communications with positioning capabilities. UWB signaling is especially suitable in this context because it allows centimeter accuracy in ranging, as well as low-power and low-cost implementation of communication systems. These features allow a new range of applications, including logistics (package tracking), security applications (localizing authorized persons in high-security areas), medical applications (monitoring of patients), family communications/supervision of children, search and rescue missions (communications with fire fighters, or avalanche/earthquake victims), control of home appliances, and military applications [9]. High data-rate UWB communication systems are well motivated for gathering and exchanging a vast quantity of sensory data in a timely manner.

- *Radar Systems:* UWB-based sensing has the potential to improve the resolution of conventional proximity and motion sensors. Relying on the high ranging accuracy and target differentiation capability enabled by UWB, intelligent collision-avoidance and cruise-control systems may be envisioned. These systems can also improve airbag deployment and adapt suspension/braking systems depending on road conditions. UWB technology can also be integrated into vehicular entertainment and navigation systems by downloading high-rate data from airport off ramp, road-side gas station UWB transmitters [10].

- *Imaging Systems:* Different from conventional radar systems where targets are typically considered as point scatterers, UWB radar pulses are shorter than the target dimensions. UWB reflections off the target exhibit not only changes in amplitude and time shift but also changes in the pulse shape. As a result, UWB waveforms exhibit pronounced sensitivity to scattering relative to conventional radar signals. This property has been readily adopted by radar systems [2] and can be extended to additional applications, such as underground, through-wall and ocean imaging, as well medical diagnostics and border surveillance devices [11].

1.1.3 Open Research Problems

UWB is an emerging new technology that is expected to enable low-cost and low-power devices. As already mentioned in 1.1.2, streams of ultra-short pulses (< 1 ns) are used for wireless data transmission instead of a modulated sinusoidal carrier, yielding signals of huge bandwidths (> 1 GHz) but at very low power densities. In principle, the baseband nature of the signal transmission makes the UWB technology suitable for low-cost implementations in standard CMOS (complementary metal-oxide-semiconductor) technology. Indeed, unlike conventional radio systems, the transmitted pulse is able to propagate without the need for an additional RF mixing stage. Then the UWB receiver can bypass the need for complex phase tracking loops. However, before UWB systems can be produced at a large scale and low cost, there are numerous open research issues to be solved.

UWB systems have opened up new dimensions of antenna design. Antennas have become an organic part of RF systems, providing filtering and other custom-designed frequency-dependent properties. The wide bandwidths of UWB antennas present new challenges for design, simulation, and modelling. Optimizing UWB antennas to meet the demands of UWB propagation channels is similarly challenging. Designers are meeting these challenges with novel antenna designs, novel materials and using concepts like polarization diversity, directivity arrays, and electric-magnetic element combinations.

Still more research at fundamental and applied levels is needed to make cheap and power-efficient UWB chips available, going beyond the existing state-of-the-art solutions in several areas of transceiver architecture design and signal processing. Due to the extremely large bandwidth of UWB systems, which prevents direct sampling of the received signal at sufficient accuracy, it is expected that a straight-forward downscaling of signal processing algorithms for conventional receivers will not lead to practical solutions for UWB devices. This implies new algorithms for channel estimation, synchronization and other typical receiver tasks that have to be developed for UWB devices. The derivation of appropriate

system models including the accurate modelling of the multi-path radio channel is as well necessary. Additionally, the shared nature of the medium means that UWB receivers must contend with a variety of interference sources. Traditional interference mitigation techniques are not amenable to UWB due to the complexity of straight-forward translations to UWB bandwidths. Thus, multi-user signal detection, multiple access interference (MAI) cancellation, narrowband interference (NBI) detection and cancellation are open research issues that must be met in order to exploit the potential benefits of UWB systems.

UWB radio technology is a well-suited physical layer candidate for the robust, low power and ubiquitous data communication requirements of WSNs. However, the fundamental role of UWB technology in WSNs is still open and a wide range of research questions continue to present challenges. The characterization of the UWB radio channel in industrial areas and large open spaces has to be addressed. The design of signaling schemes that make efficient use of the channel capacity at low complexity and low power consumption is necessary, as well as efficient medium access control (MAC) protocols for a large number of distributed sensor nodes. The derivation of algorithms to provide location information of wireless sensor nodes and geographic information about the environment has equal interest.

1.2 Ultra-Wideband Wireless Sensor Networks

In this section, the basic challenges in designing WSNs are revisited, followed by the introduction of the UWB approach for radio communications among the sensor nodes in a WSN, that addresses each one of the design challenges. Finally, the overview of our envisaged application is presented.

1.2.1 Wireless Sensor Network Requirements

WSNs have emerged as a new wireless networking paradigm allowing distributed sensing and cooperative communication strategies. They also represent a new generation of real-time embedded systems with different significant communication constraints when compared with traditional networked systems. The main design challenges in WSNs can be categorized into the following areas:

- *Scalability*: As the number of sensor nodes in a WSN increases, scalability imposes difficulties in transferring data. In order to send information to far away nodes, signals with higher transmission power should be employed which can cause inter-node interference or a multi-hop approach need to be considered.

- *Power conservation*: The nodes in WSNs have limited energy resources, so to extend the lifetime of the entire network power conservation in individual nodes is of significant importance. In WSNs, radio communications is the major consumer of energy. Hence, minimizing the radio transmission power or avoiding unnecessary communications can considerably save power in sensor nodes.

- *Synchronization*: During radio communications between different wireless sensor nodes of a WSN, nodes continuously listen to transmissions and consume power

if they are not time synchronized with each other. While global synchronization is unrealistic, especially when there is large sensor population, node-by-node synchronization becomes a necessity in WSN design.

- *Channel estimation*: Channel estimation plays a critical role in WSNs, since sensor nodes communicate over wireless channels and have to overcome the effects of a wireless link, such as noise, multipath effect, intentional jamming and inter-node interference. Estimating the wireless link between a specific transmitter and receiver pair provides directionality and reliable data transfer between the nodes.

- *Self-organization*: When large number of sensor nodes are deployed in remote environments, the ability of individual sensor nodes to self-organize is vital. Self-organization should be done in a way to improve the performance while reducing the power consumption of the entire sensor network.

1.2.2 Ultra-Wideband Approach to Wireless Sensor Networks

WSNs are characterized by devices with low complexity that have limitations on processing power and memory, and severe restrictions on power consumption. By the very nature of the application, traffic in WSNs is often bursty with long periods of no activity (low duty cycle). For event detection operations, a device may remain idle for long periods, then suddenly be required to send significant amounts of information when an event occurs. For devices deployed in the field, this has significant implications for the design of efficient MAC protocols, radio communications technology, and the reliability of information transfer. For devices involved in continuous monitoring, the flow of traffic will be more stable. However, efficient multiple access techniques, reliability, and battery life are still major considerations.

Since 2002, interest in UWB-based applications has increased greatly, especially concerning the use of UWB for WSNs. IR-based UWB technology has a number of inherent properties that are well suited for WSN applications. In particular, UWB-IR systems have potentially low complexity and low cost. This arises from the essentially baseband nature of the signal transmission. Unlike conventional radio systems, the UWB transmitter produces a very short time domain pulse that is able to propagate without the need for an additional RF mixing stage. The RF mixing stage translates the signal to a frequency that has desirable propagation characteristics. The signal will propagate well without need for additional upconversion and amplification. The UWB receiver also does not require the reverse process of downconversion. Again, this means a local oscillator in the receiver can be omitted, which means the removal of associated complex delay and phase tracking loops.

Using UWB technology for inter-node communication in WSNs will offer not only low complexity and cost factors, but also provide high performance for communication over the wireless channels in spite of multipath distortions. Furthermore, transmission of short duration UWB pulses requires much lower power compared to strong narrowband signal transmission. In UWB-based WSNs, nodes can only communicate with their close-by

neighbors due to low transmission power and avoid the inter-node interference issue that exists in narrowband techniques.

Despite all the benefits that UWB technology offers to the design of WSNs, it can create a unique set of challenges too. Employing the low powered UWB pulses for inter-node communications, introduces the scalability problem in WSNs. As the distance between nodes or the number of nodes increases, weak UWB pulses cannot transfer information between nodes in a reliable manner. Also, the short duration of UWB pulses introduces a major challenge in time synchronization for sensor nodes in a wireless network. In order to synchronize sub-nanosecond pulses, very high-speed analog-to-digital converter (ADC) components are needed. Another problem with using UWB technology for WSNs is the performance degradation due to interference from strong narrowband signals that share the spectrum with low powered UWB pulses. Moreover, detection of UWB pulses is commonly performed using classical *matched filtering* technique, where the received signal is correlated with a UWB pulse template. Thus, wireless channel multipath effects on the received signal can significantly degrade the detection process due to low correlation between the predefined template and the distorted received signal.

The challenge posed by synchronization and channel degradation to narrow and low powered UWB pulses has been addressed by the transmitted-reference (TR) signaling which is extensively presented in this thesis. TR receivers correlate the received signal with a delayed replica of itself. Using TR-UWB transceivers for radio communication of WSNs offers simplicity, low transmission power, and capability to reduce the stringent UWB synchronization requirements, as well as channel estimation. On the other hand the performance of TR receivers is considerably limited by the severity of noise-noise products introduced by the correlation of noise in the received signal. Therefore, scalability becomes a major issue in designing WSNs with TR-UWB transceivers. On the other hand, channel estimation is not required with TR-UWB transceivers.
Finally, UWB-IR systems have a very good time domain resolution, allowing for localization and tracking applications [12].

1.2.3 Conceptual Design of the Envisaged Application

The ranging network presented in this subsection can be viewed as a WSN where the physical parameter to be sensed is location. The radio module of each node is based on low-power low-complexity TR-UWB transceivers since sensor nodes are inherently resource constrained: limited processing capabilities, storage capacity, and power consumption. Moreover, they need to be designed with low complexity to meet the low cost requirements.

Within the overall objective of investigating the communication requirements in WSNs our primary focus was the design of some experimental sensor nodes, which are capable of a tremendous diversity of functionality such as sensing capabilities, signal processing, network protocol functions, short-range radio communication at low to medium bit rates (up to 1 Mbps) and localization capabilities. The experimental design of the ZESS sensor nodes, as well as the asynchronous transfer of GPS data to those sensor nodes are described in Appendix VI.

An overview of the different activities involved in our envisaged WSN, with communi-

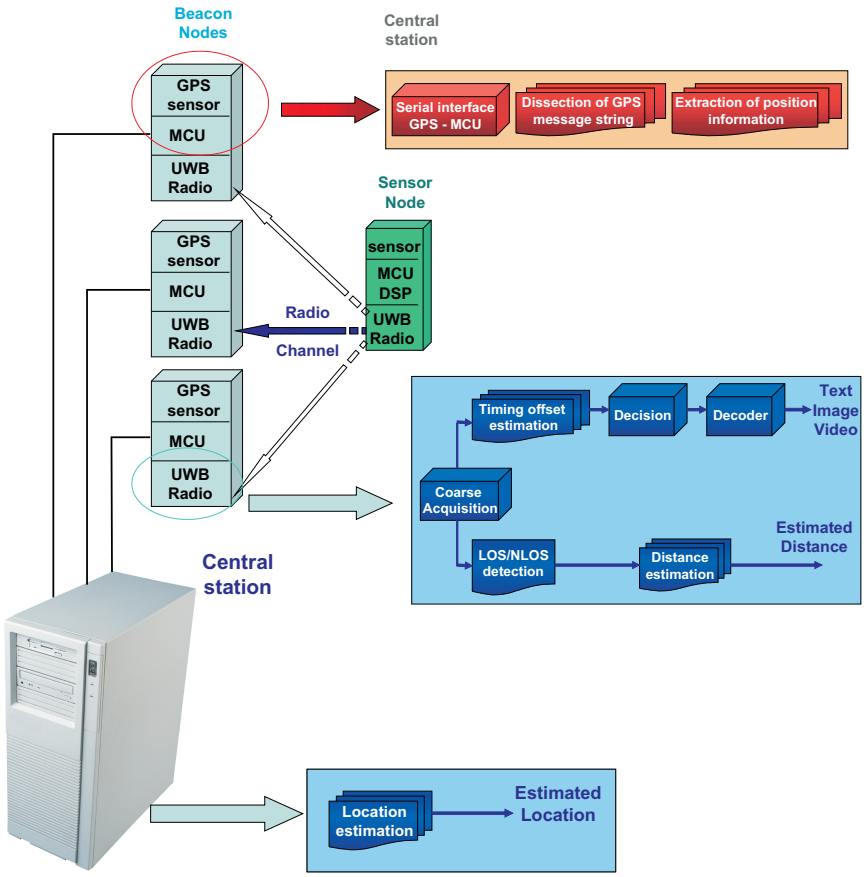

Figure 1.7: UWB based wireless sensor network.

cation and localization capabilities using IR TR-UWB systems, is depicted in Fig. 1.7. In this application, the sensor node communicates with different beacon nodes. The beacon nodes are assumed to be aware of their position by interfacing them with GPS sensors and allowing them to be mobile, or by keeping them at fixed known positions. The signals received at the beacon nodes are processed in order to localize the sensor node. Using a centralized tightly-coupled system architecture, the beacon nodes are connected to a central station, through a wire or wirelessly, where the location of the sensor node is estimated. Tracking of a mobile sensor node is also possible using appropriate tracking algorithms.

The UWB radio module in Fig. 1.7 contains two different subsystems: the data subsystem and the distance measurement subsystem. All the different blocks in both subsystems, that is, coarse acquisition, timing offset estimation, symbol decision, decoding, and distance estimation are thoroughly addressed in this thesis. The line-of-sight (LOS)/non line-of-sight (NLOS) detection, which is beyond the scope of this thesis, is briefly addressed hereafter.

The radio channel presented in Fig. 1.7 may generally have three different profiles.

The first one is the dominant direct path (DDP) case, in which the strongest path of the channel estimate corresponds to the LOS. Those channel profiles, where the first path is not the strongest, however still detectable by an appropriate receiver architecture, are called non-dominant direct path (NDDP). Finally and only regarded as NLOS, in this thesis, are the situations in which the receiver architecture is not able to detect the direct path anymore. This case has been defined as undetected direct path (UDP) and leads to ranging errors. Consequently, NLOS channels are one of the major drawbacks for accurate ranging and localization with UWB technology. To mitigate this drawback, many LOS/NLOS detection algorithms are proposed in the literature. In [13] a simple estimator has been proposed for NLOS detection using the running variance on N subsequent range estimates $\hat{d}_n$. Another LOS/NLOS detection solely uses the estimate of one channel impulse response and therefore introduces no additional delay. The so called confidence metric, as defined in [12] and used for LOS/NLOS detection, is based on the idea that later multipath components should have less power than the direct component in the LOS case and vice versa in the NLOS case. This reasoning is valid for distinguishing between DDP and UDP channel profiles. Some authors have stated that the root mean square (RMS) delay spread could be used as an LOS/NLOS detection method [14], however, they have not investigated the proposal further since no threshold was proposed. Finally, LOS/NLOS detection could be based on the assumption that a sudden decrease of signal-to-noise ratio (SNR) could indicate the movement from a LOS into an NLOS condition, and vice versa. In this case, changes in the power of subsequent maximum paths are detected and normalized. Many of the described algorithms are difficult to apply with real UWB localization systems. For a suitable hypothesis testing of ranging error distributions, many range estimations must be evaluated at the same position to create an error distribution estimate, and valid error distributions for the LOS and NLOS case must be available. Both demands are rather seldom in reality. In addition, the necessity of a statistical significance contrasts the need for a small latency of detection for a robust localization system. Similar obstacles occur when channel estimates are to be tested against predefined channel models. Even if these methods work in real environments, the existence of enough LOS channels in realistic indoor applications is probably quite seldom. Consequently, distance measuring techniques which are less prone to LOS/NLOS conditions are useful.

In this thesis, a novel distance measurement approach based on the modelling of the energy collected at the output of the TR-UWB receivers as a function of delay is proposed. Since the total energy is the sum of signal strengths of each individual path in a multipath environment, this measurement technique takes advantage of the multipath diversity in the channel. Furthermore, the timing requirement in our method is less rigorous than when using time-based distance measuring techniques, and it is more tolerant in UDP cases. This implies that the NLOS/NLOS detection can be omitted while using our distance measurement technique, at the expense of loosing some accuracy in distance measurement. This is the tradeoff complexity/accuracy.

1.3 Goal of the Thesis

The main objective of this doctoral thesis is to present the conceptual design of UWB-IR transceivers that have dual functionality in providing robust, low power data communication and accurate location information in WSNs. The intended application would be the monitoring and localization of wireless sensor nodes within a closed area (indoor and outdoor environments).

The emphasis of this study lays on the physical layer: modelling and analysis of the radio transceivers, simulation of receiver algorithms and characterization of the physical radio link. Wireless transmission using different TR-UWB IR systems allows peak data rates up to 5 Mbit/s and location estimation with around 30 cm accuracy for a transmitter-receiver separation within 10 m. The TR signalling was used due to its simple receiver structure.

1.4 Organization of the Thesis

This doctoral thesis is structured as follows:

- In Chapter 1 the UWB technology was presented highlighting the history behind it and the regulatory issues. The basic techniques in UWB systems were introduced and an insight was provided on the open research issues in this new emerging technology. The envisaged application related to this work was presented. This chapter ends with emphasis on the goal and contributions of this thesis.

- Chapter 2 deals with polynomial nonlinear systems. The Volterra model is also presented in this chapter. Further, the Hammerstein and Wiener models, which are the simplified forms of the Volterra model, are addressed as well.

- Chapter 3 presents an important tool for the design and analysis of communication systems: the radio channel model. Different channel models for UWB applications are revisited.

- Different TR systems are introduced in chapter 4. System models are derived for evaluating more effectively the BER performance of the low complexity TR-UWB systems considered through simulation.

- Chapter 5 addresses the synchronization issues. Coarse and fine synchronization algorithms are developed and analyzed.

- Based on the results from chapter 5, the performance of different location estimation algorithms is evaluated in chapter 6.

- Finally, general conclusions, recommendations and possible directions for future works are summarized in chapter 7.

1.5 Contributions of the Thesis

This thesis presents several contributions towards developing UWB-IR technology for short-range low to medium data rate WSN applications. The contributions can be classified into two classes. The first class of contribution concerns the design through simulation of low complexity TR-UWB systems capable of providing data rates up to 5 Mbit/s. Based on previous work done on modelling TR-UWB systems, delay-dependent systems models for different low complexity TR-UWB systems are proposed. These models are aimed in facilitating the performance analysis of the various systems considered, designing efficient detectors and developing new algorithms. The second class of contribution consists of the development of simple algorithms for synchronization and distance estimation using the proposed delay-dependent systems models.

1.5.1 Systems Modelling

In [15] a discrete-time Volterra equivalent system model was derived for DTR-UWB systems in a multipath channel, where both inter-frame interference (IFI) and inter-symbol interference (ISI) are present. Using this model, delay-dependent discrete time equivalent system and noise models for different low complexity TR-UWB systems are proposed in this thesis.

1.5.2 Performance Analysis

The different TR-UWB receiver statistics are analyzed, first, using the Gaussian approximation on the noise terms in the receiver statistics, then, using the equivalent system and noise models of the different TR-UWB receivers.

1.5.3 BER derivation

Both perspectives for receiver statistics analysis allow for bit error rate (BER) performance analysis to be performed. The derivation of an analytic expression for the average BER is provided in this thesis using the concept of minimum distance receiver.

1.5.4 Coarse Synchronization

In this thesis, a novel data-aided timing acquisition technique for differential TR-UWB systems is presented. It achieves efficient multipath energy collection even in presence of timing offset and noise.

1.5.5 Fine Synchronization

Another contribution of this thesis in the field of synchronization concerns a simple timing offset estimator for low complexity TR-UWB systems. The proposed algorithm uses energy collected at the symbol rate, thus reducing considerably the implementation complexity.

1.5.6 Distance and Location Estimation

Assuming coarse synchronization achieved and hardware clock timing error known, the timing offset estimation algorithm can readily be used for distance and location estimation. To my knowledge, the distance measuring approach proposed in this thesis has never been dealt with before. It is similar to the signal strength measurement technique, but instead of using a path loss model, the modelling of the energy collected at the output of the UWB receivers as a function of delay is used.

Chapter 2

Polynomial Nonlinear Systems: Overview

2.1 Introduction

All *linear systems* obey the *superposition principle*, which implies that the output of a linear combination of input signals to a linear system is the same linear combination of the outputs of the system corresponding to the individual components. That is,

$$\mathcal{L}\{\alpha x_1(n) + \beta x_2(n)\} = \alpha\mathcal{L}\{x_1(n)\} + \beta\mathcal{L}\{x_2(n)\}, \tag{2.1}$$

where $\mathcal{L}\{(\cdot)\}$ denotes the output of the linear system, $x_1(n)$ and $x_2(n)$ are two different input signals, and α and β are two arbitrary constants. The superposition principle is a powerful mechanism that allows the study of all linear systems in a unified manner. *Nonlinear systems* do not satisfy the superposition principle. Furthermore, since every system that does not satisfy the superposition principle is nonlinear, it is impossible to develop a framework that is applicable to all nonlinear systems. Consequently, the traditional approach for modelling and studying nonlinear systems is to consider one or more classes of such systems and to develop a theory for analysis, design and realization as well as applications of such classes individually. In the next subsections several classes of nonlinear systems are briefly described [16].

2.1.1 Homomorphic Systems

A *homomorphic system* satisfies the generalized superposition principle stated as

$$\mathcal{H}\{x_1(n) * x_2(n)\} = \mathcal{H}\{x_1(n)\} + \mathcal{H}\{x_2(n)\}, \tag{2.2}$$

where "$*$" and "$+$" are two operations defined on the input signal and the output signal, respectively.

As an example, the intensity of light reflected from an object can be modelled as the product of the intensity of the light that shines on the object at each location and the reflection coefficient of the object [17], i.e., an image $x(n_1, n_2)$ may be expressed as

$$x(n_1, n_2) = I(n_1, n_2) r(n_1, n_2), \tag{2.3}$$

where $I(n_1, n_2)$ is the light intensity that falls on the object at location (n_1, n_2) and $r(n_1, n_2)$ denotes the reflection coefficient of the object at the same location. *Homomorphic filters* are particularly useful in situations, where the information-bearing function $r(n_1, n_2)$ needs to be separated from the image, or when it is necessary to process the two components in different ways using an appropriate nonlinear transformation and a linear filter following the nonlinearity. Fig. 2.1 shows the block diagram of a homomorphic filter, where the first block transforms the input signal using a logarithmic nonlinearity. The transformed signal is then processed by a linear filter. The output of the logarithmic nonlinearity is given by

$$y(n_1, n_2) \;=\; \ln\left(x(n_1, n_2)\right) \;=\; \ln\left(I(n_1, n_2)\right) + \ln\left(r(n_1, n_2)\right). \tag{2.4}$$

Thus, the linear filter will see the multiplicative components as additive components at its input. Consequently, linear filtering techniques can be used to discriminate the two components.

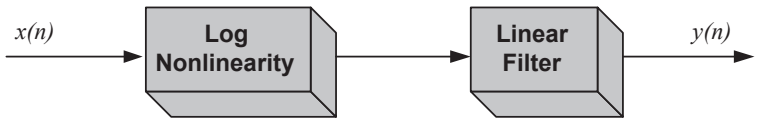

Figure 2.1: A homomorphic filter employing a logarithmic nonlinearity.

2.1.2 Order Statistic Filters

Order statistic filters are employed in applications in which the input signal is corrupted by impulsive noise. The class of order statistic filters includes the median filter and its generalizations. A one-dimensional $(2K+1)$-point median filter is defined by the input-output relationship

$$y(n) = \text{median}\{x(n+K), x(n+K-1), \ldots, x(n-K)\}, \tag{2.5}$$

where the median of the $2K+1$ samples within the curly brackets is the $(K+1)^{\text{th}}$ value among the samples rearranged in the ascending or descending order of magnitude.
A generalization of the median filter computes the output signal as a linear combination of samples arranged in ascending or descending order of magnitude. The output of such a filter may be expressed as

$$y(n) = \sum_{i=0}^{N-1} h_i x_i(n), \tag{2.6}$$

where $x_i(n)$ is the i^{th} sample in a rearrangement of the set $x(n), x(n-1), \ldots, x(n-N+1)$ in the ascending order of magnitude and h_i denotes the coefficients of $x_i(n)$. This type

of generalization provides the filter with a combination of properties associated with the linear filters and the median filters. Other types of order statistic filters include weighted median filters, finite impulse response (FIR)-median hybrid filters, weighted order statistic filters, rank selection filters and stack filters [18] [19].

2.1.3 Morphological Filters

In applications such as pattern recognition and robotics, it is necessary to partition an image into segments on the basis of the geometric properties of the objects depicted in the image. This can be achieved through the use of mathematical transformations of the input images using operators known as *morphological transforms*. Signal processing systems that employ morphological transforms are known as *morphological filters* [20]. In addition to pattern and shape recognition and image decomposition using skeletal representation, morphological filters have also been used in image compression systems [21].

2.1.4 Neural Networks

Neural networks model nonlinear systems using interconnections of simple nonlinear devices known as *artificial neurons*. Artificial neurons are typically multiple-input, single-output systems with input-output relationship in the form

$$y(n) = f\left\{\sum_{i=1}^{N} w_i x_i(n) - \theta\right\}, \tag{2.7}$$

where w_i is the weight associated with the ith input $x_i(n)$ to the device and θ is a constant term that controls the operating point of the nonlinearity f. An artificial neuron with this characteristic is depicted in Fig. 2.2.

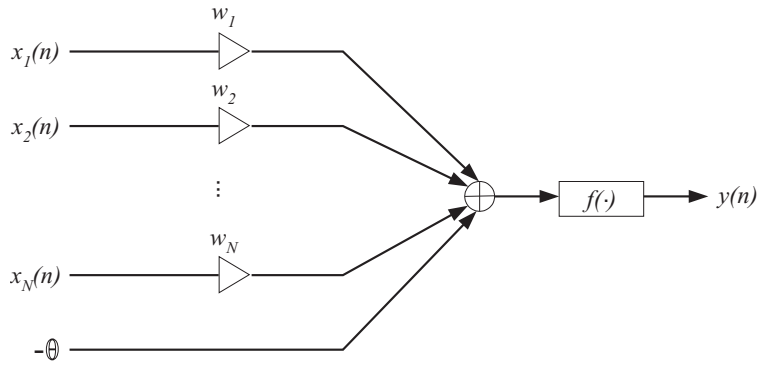

Figure 2.2: An artificial neuron.

Many different types of nonlinear functions have been employed, and some of the common ones are shown in Fig. 2.3.

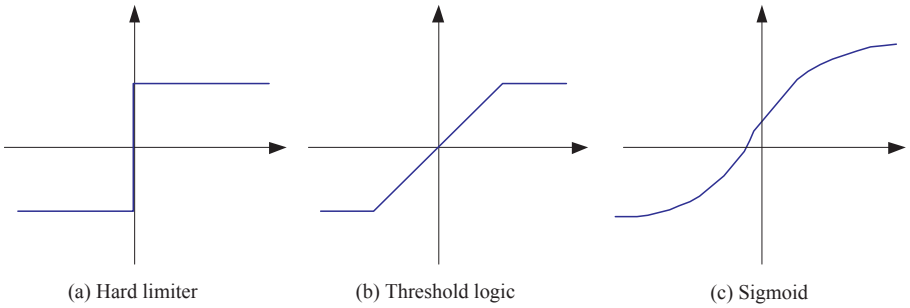

Figure 2.3: Nonlinearities commonly employed in neural networks.

In typical applications, the weights w_i used in the network are selected by training the neural network on data that are representative of what the network will encounter in normal applications. The training is accomplished using an adaptation algorithm such as the *back propagation* algorithm. Algorithms for neural network design and their applications are thoroughly described in [22].
The advantage of artificial neural networks is their ability to model most nonlinear systems. However, in order to perform the modelling accurately, the network might require a very large number of artificial neurons. Another disadvantage of neural networks is that global convergence of training algorithms such as back propagation is not guaranteed.

2.1.5 Polynomial Filters

Causal, discrete-time *polynomial filters* satisfy the input-output relationship of the form

$$y(n) = \sum_{i=0}^{P} f_i \left[x(n), x(n-1), \ldots, x(n-N), y(n-1), \ldots, y(n-M)\right], \tag{2.8}$$

where the function $f_i[\ldots]$ is an ith-order polynomial in the variables within the bracket. This definition contains the linear filters as special case since the system in (2.8) is linear if $f_i[\ldots] = 0$ for all $i \neq 1$. If the system in (2.8) is stable in the bounded-input bounded-output sense, it admits a convergent *Volterra series expansion* of the form

$$\begin{aligned} y(n) = \; & h_0 + \sum_{m_1=0}^{N_1-1} h_1(m_1)x(n-m_1) + \sum_{m_1=0}^{N_1-1}\sum_{m_2=0}^{N_2-1} h_2(m_1,m_2)x(n-m_1)x(n-m_2) + \ldots \\ & + \sum_{m_1=0}^{N_1-1}\sum_{m_2=0}^{N_2-1}\cdots\sum_{m_r=0}^{N_r-1} h_r(m_1,m_2,\ldots,m_r)x(n-m_1)x(n-m_2)\ldots x(n-m_r) \\ & + \ldots, \end{aligned} \tag{2.9}$$

where $h_r(m_1, m_2, \ldots, m_r)$ denotes the r^{th}-order *Volterra kernel* of the nonlinear system. The term involving the r^{th}-order kernel looks like an r-dimensional convolution. Consequently, polynomial systems are considered as generalizations of linear systems.

2.2 Volterra Series Expansion

Volterra series expansions form the basis of the theory of polynomial nonlinear systems. In this section, the Volterra series expansions are introduced and their properties are discussed.

2.2.1 Continuous-time Systems

A *system* is defined mathematically as a rule for transformation of an input signal x into another signal y by means of an operator S so that

$$y = S\{x\}. \tag{2.10}$$

The input and output signals are usually functions of one or more independent variables such as position or time. If they are functions only of time t, and the variable t is defined over a continuous range of values, (2.10) defines a continuous one-dimensional system whose input-output relationship can be represented as

$$y(t) = S\{x(t)\}. \tag{2.11}$$

Linear Shift-invariant Systems

A *shift-invariant* system is characterized by the invariance of its output with respect to a shift in the independent variable. As an example, a time-invariant system satisfies the relationship

$$y(t+\tau) = S\{x(t+\tau)\} \tag{2.12}$$

for all values of τ. A *linear* system is one that satisfies the superposition principle. This implies that

$$S\{\alpha x_1(t) + \beta x_2(t)\} = \alpha S\{x_1(t)\} + \beta S\{x_2(t)\} \tag{2.13}$$

for all arbitrary constants α and β and arbitrary $x_1(t)$ and $x_2(t)$.
The output of a continuous time linear and time-invariant (LTI) system is related to the input signal through the convolution integral

$$y(t) = \int_{-\infty}^{\infty} h(\tau)x(t-\tau)d\tau, \tag{2.14}$$

where $h(t)$ is the impulse response of the system. Equation (2.14) implies that the impulse response completely characterizes an LTI system. A system is said to be *causal* if its output at any given time does not depend on the future values of its input. An LTI system is causal if and only if

$$h(t) = 0 \quad \text{for} \quad \text{t} < 0. \tag{2.15}$$

The unit impulse response signal represents the *memory* of the LTI system since the contribution to the current value of the output signal from the value of the input signal T seconds prior to the present time is determined by $h(T)$. The output of a memoryless LTI system is given by

$$y(t) = c(x(t)), \tag{2.16}$$

which is obtained by convolving the input $x(t)$ with $c\delta(t)$, where $\delta(t)$ represents the Dirac function and c is a constant that determines the extent of amplification or attenuation of the input signal at the output of the system.

Volterra Series Expansion for Nonlinear Systems

A nonlinear system without memory can be often described by means of an appropriate series expansion. A power series expansion such as the Taylor series expansion may be used to describe the output of such systems as

$$y(t) = \sum_{p=0}^{\infty} c_p x^p(t). \tag{2.17}$$

A nonlinear system with memory can be represented by means of an extension of this expression. Such an extension, known as the *Volterra series expansion* [23], relates the input and output signals of the system as

$$\begin{aligned} y(t) = \; & h_0 + \int_{-\infty}^{\infty} h_1(\tau_1)x(t-\tau_1)d\tau_1 + \int_{-\infty}^{\infty}\int_{-\infty}^{\infty} h_2(\tau_1,\tau_2)x(t-\tau_1)x(t-\tau_2)d\tau_1 d\tau_2 + \dots \\ & + \int_{-\infty}^{\infty} \dots \int_{-\infty}^{\infty} h_p(\tau_1,\tau_2,\dots,\tau_p)x(t-\tau_1)x(t-\tau_2)\dots x(t-\tau_p)d\tau_1\dots d\tau_p. \end{aligned} \tag{2.18}$$

The nonlinear system represented by a Volterra series expansion is completely characterized by the multidimensional functions $h_p(t_1, t_2, \dots, t_p)$, called the *Volterra kernels*. The zero$^{\text{th}}$-order kernel h_0 is a constant. The higher-order kernels can be assumed, without loss of generality, as symmetric functions of their arguments so that any of the $p!$ possible permutations of $t_1, t_2, \dots, t_p$ leaves $h_p(t_1, t_2, \dots, t_p)$ unchanged. This symmetry is the direct result of the invariance of the products of the delayed input functions $\{x(t-\tau_i), i = 1, \dots, p\}$ with respect to their permutations. The system is causal if and only if

$$h_p(t_1, \dots, t_p) = 0 \quad \text{for any} \quad t_i < 0 \quad \text{and} \quad i = 1, \dots, p. \tag{2.19}$$

The lower limits in the integrals in (2.18) are therefore set to zero for causal nonlinear systems. The upper limits of the integrals in (2.18) given as ∞ indicate that the system may have infinite memory. If the upper limits are all finite, the system possesses finite memory. Each integral in (2.18) has the form of a multidimensional convolution. By defining the p^{th}-order Volterra operator $\bar{h}_p[x(t)]$ as

$$\bar{h}_p[x(t)] = \int_{-\infty}^{\infty} \dots \int_{-\infty}^{\infty} h_p(\tau_1, \tau_2, \dots, \tau_p) x(t-\tau_1) x(t-\tau_2) \dots x(t-\tau_p) d\tau_1 \dots d\tau_p. \quad (2.20)$$

Equation (2.18) may be written more compactly as

$$y(t) = h_0 + \sum_{p=1}^{\infty} \bar{h}_p[x(t)]. \quad (2.21)$$

A *truncated* Volterra series expansion is obtained by setting the upper limit of the summation in (2.21) to a finite integer value P. The parameter P is called the *order*, or the *degree*, of the Volterra series expansion. (2.21) reveals the similarity of Volterra series expansions with the Taylor series expansions. When the input signal is multiplied by a constant factor c, the output $y(t)$ becomes

$$y(t) = h_0 + \sum_{p=1}^{\infty} \bar{h}_p[cx(t)] = h_0 + \sum_{p=1}^{\infty} c^p \bar{h}_p[x(t)]. \quad (2.22)$$

which is a power series expansion in c.

Limitations of Volterra Series Expansions

As a consequence of its power series characteristic, there are some limitations associated with the application of the Volterra series expansion to nonlinear system modeling. These are:

- *Convergence issues*: Because of its close relationship with Taylor series expansions, Volterra series expansions exhibit convergence problems when the nonlinear systems to be modeled include strong nonlinearities such as saturating elements. Therefore, the Volterra series approach can be applied with good results only to systems with mild nonlinearities.

- *Nonlinear systems not completely charaterized by the impulse response function*: In contrast to the LTI systems, the impulse response function does not fully characterize a nonlinear system. Indeed, the response of the nonlinear system to the impulse $c\delta(t)$ is given by

  $$h(t) = h_0 + ch_1(t) + c^2 h_2(t,t) + \dots + c^p h_p(t, \dots, t) + \dots. \quad (2.23)$$

  This indicates that the impulse response is determined only by diagonal values of he kernel h_p, that is for $t = t_1 = t_2 = \dots = t_p$. Thus, it does not completely specify the p^{th}-order Volterra kernels of higher order than 1.

- *Multiple-valued nonlinearities*: Since the Volterra series expansion is a single-valued representation, it cannot be used to represent multiple-valued nonlinearities.

2.2.2 Discrete-time Systems

Consider a system for which the input and output values are known only at given time instants $t = nT$, where n is an integer variable. By assuming a normalized time interval $T = 1$, (2.11) becomes

$$y(n) = S\{x(n)\}. \tag{2.24}$$

This equation describes a general one-dimensional discrete-time system. Many classifications of discrete-time systems can be made in a manner similar to those of continuous-time systems.

A discrete time shift-invariant system is characterized by the property that it is invariant to shifts in the independent variable:

$$y(n+m) = S\{x(n+m)\}, \tag{2.25}$$

where m is an integer shift. A discrete time shift-invariant system is said to be *discrete time-invariant* (DTI) when the independent variable is time. A discrete-time is said to be linear if it obeys the superposition principle:

$$S[\alpha x_1(n) + \beta x_2(n)] = \alpha S[x_1(n)] + \beta S[x_2(n)], \tag{2.26}$$

for all arbitrary constants α and β and arbitrary input signals $x_1(n)$ and $x_2(n)$. If a discrete-time system is both linear and time-invariant its output can be evaluated by convolving its input signal with its unit impulse response function h_n as

$$y(n) = \sum_{m=-\infty}^{\infty} h(m)x(n-n). \tag{2.27}$$

A discrete-time LTI system is *causal* if and only if

$$h(n) = 0 \quad \text{for} \quad \text{n} < 0. \tag{2.28}$$

DTI Nonlinear Systems

In a manner similar to continuous case, it is possible to describe DTI nonlinear systems with memory by means of the discrete-time Volterra series expansion

$$y(n) = h_0 + \sum_{p=1}^{\infty} \bar{h}_p[x(n)], \tag{2.29}$$

where $y(n)$ and $x(n)$ are the output and input signals, respectively, and

$$\bar{h}_p[x(n)] = \sum_{m_1=-\infty}^{\infty} \dots \sum_{m_p=-\infty}^{\infty} h_p(m_1, \dots, m_p)x(n-m_1)x(n-m_2)\dots x(n-m_p), \tag{2.30}$$

where $h_p(m_1, \ldots, m_p)$ is the p^{th}-order Volterra kernel of the system. If $h_p(m_1, \ldots, m_p) = 0$ for all $m_i < 0$, and $i = 1, \ldots, p$, the DTI nonlinear system is causal, and (2.30) becomes

$$\bar{h}_p[x(n)] = \sum_{m_1=0}^{\infty} \ldots \sum_{m_p=0}^{\infty} h_p(m_1, \ldots, m_p) x(n - m_1) x(n - m_2) \ldots x(n - m_p). \tag{2.31}$$

The discrete-time Volterra kernels can be interpreted in a manner similar than the continuous-time systems. The constant h_0 is an offset term, $h_1(m_1)$ is the impulse response of a discrete-time LTI filter, and the p^{th}-order kernel $h_p(m_1, \ldots, m_p)$ can be considered as a generalized p^{th}-order impulse response characterizing the nonlinear behavior of the system. The upper limit in the summations in (2.31) given as infinity indicates that the discrete system may have infinite memory. The difficulties that arise because of the infinite summations in (2.31) may be avoided by using recursive polynomial system models. This approach is similar to the use of infinite impulse response (IIR) filters in applications involving linear system models.

Usually, the memory required to adequately approximate a nonlinear system is finite. In such situations, a Volterra series expansion involving only the input signal is sufficient to model the system. This simpler class of nonlinear system models is derived by limiting all the summations in (2.31) to finite values. In this case, $h_1(m_1)$ represents the impulse response of a finite impulse response (FIR) filter, and the effect of the nonlinearity on the output depends only on the present and past values of the input signals defined on the extent of the filter support. If the discrete Volterra series expansion is truncated by limiting the summation in (2.29) to a finite value P, finite-order expansion is obtained as

$$y(n) = h_0 + \sum_{p=1}^{P} \bar{h}_p[x(n)], \tag{2.32}$$

where

$$\bar{h}_p[x(n)] = \sum_{m_1=0}^{N-1} \ldots \sum_{m_p=0}^{N-1} h_p(m_1, \ldots, m_p) x(n - m_1) x(n - m_2) \ldots x(n - m_p). \tag{2.33}$$

Equation (2.32) represents a general discrete-time Volterra model of order P and memory length N. The upper limits in all the summations of (2.33) are made identical only for convenience. They may be set to arbitrary values to obtain a more general expression. The simplest polynomial filter of this class is the *quadratic filter* obtained by choosing $P = 2$ in (2.32). This type of filter is discussed in the next two subsections.

2.2.3 Algebraic Representation of Quadratic Filters

A causal, discrete and time-invariant quadratic filter with finite support for its kernels is described by means of the first three terms of the Volterra series expansion as

$$y(n) = h_0 + \sum_{m_1=0}^{N-1} h_1(m_1)x(n-m_1) + \sum_{m_1=0}^{N-1}\sum_{m_2=0}^{N-1} h_2(m_1,m_2)x(n-m_1)x(n-m_2), \quad (2.34)$$

where h_0 represents a constant offset term, $\{h_1(m_1); 0 \leq m_1 \leq N-1\}$ denotes the coefficients of a linear time-invariant FIR filter and $\{h_2(m_1,m_2); 0 \leq m_1, m_2 \leq N-1\}$ represents the coefficient of a homogenous quadratic filter. The quadratic filter can be realized as a parallel combination of these three components as shown in Fig. 2.4.

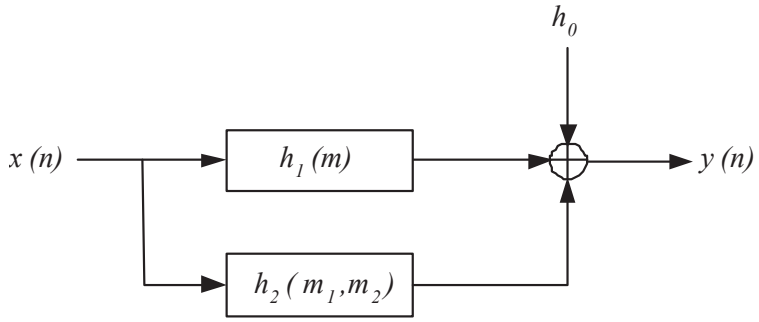

Figure 2.4: A quadratic filter realized as a parallel combination of three components.

Matrix-Vector Representation

It is usual to arrange the input values and the filter coefficients of one-dimensional linear FIR filters into two vectors $\mathbf{x}(n)$ and $\mathbf{h}_1$ defined as

$$\mathbf{x}(n) = \begin{bmatrix} x(n) & x(n-1) & \cdots & x(n-N+1) \end{bmatrix}^T \quad (2.35)$$

and

$$\mathbf{h}_1 = \begin{bmatrix} h_1(0) & h_1(1) & \cdots & h_1(N-1) \end{bmatrix}^T. \quad (2.36)$$

$\bar{h}_1[x(n)]$ is expressed as

$$\bar{h}_1[x(n)] = \mathbf{x}^T(n)\mathbf{h}_1 = \mathbf{h}_1^T\mathbf{x}(n). \quad (2.37)$$

In similar way, the input-output relation of a quadratic filter can be written as

$$\bar{h}_2[x(n)] = \mathbf{x}^T(n)\mathbf{H}_2\mathbf{x}(n), \quad (2.38)$$

where $\mathbf{H}_2$ is an $N \times N$ matrix in which the coefficients of the quadratic kernel $h_2(m_1,m_2)$ are arranged as

$$\mathbf{H}_2 = \begin{bmatrix} h_2(0,0) & h_2(0,1) & \cdots & h_2(0,N-1) \\ h_2(1,0) & h_2(1,1) & \cdots & h_2(1,N-1) \\ \vdots & \vdots & \ddots & \vdots \\ h_2(N-1,0) & h_2(N-1,1) & \cdots & h_2(N-1,N-1) \end{bmatrix}. \tag{2.39}$$

2.2.4 Realization of Quadratic Filters

The homogeneous quadratic term in (2.34) may be equivalently represented using a triangular kernel as

$$\bar{h}_2[x(n)] = \sum_{m_1=0}^{N-1} \sum_{m_2=m_1}^{N-1} h_{2t}(m_1, m_2) x(n-m_1) x(n-m_2), \tag{2.40}$$

where

$$h_{2t}(m_1, m_2) = \begin{cases} h_2(m_1, m_2); & m_1 = m_2 \\ h_2(m_1, m_2) + h_2(m_2, m_1); & m_1 < m_2 \\ 0; & \text{otherwise.} \end{cases} \tag{2.41}$$

$\bar{h}_2[x(n)]$ can be implemented by means of a nonlinear combiner, a number of multipliers, and a summing bus as shown in Fig. 2.5. The nonlinear combiner computes all the necessary products of the input samples.

2.3 Wiener & Hammerstein Models

One of the most frequently studied classes of polynomial nonlinear models are the so called *block-oriented models*, which consist of the interconnection of LTI systems and static (memoryless) nonlinearities. Within this class, four of the more common model structures are the:

- *Hammerstein model*, which consists of the cascade connection of a static nonlinearity followed by a LTI system (see for instance [24] for a review on identification of Hammerstein models)
- *Wiener model*, in which the order of the linear and the nonlinear blocks in the cascade connection is reversed (see for instance [25] and [26] for different methods for the identification of Wiener models)
- *LNL cascade model*, which is represented by a combination of Hammerstein and Wiener systems. Indeed, it is a cascade of a LTI filter followed by a static nonlinearity, followed by another LTI filter. In [27] a three steps adaptive algorithm for identification of the LNL model is outlined.

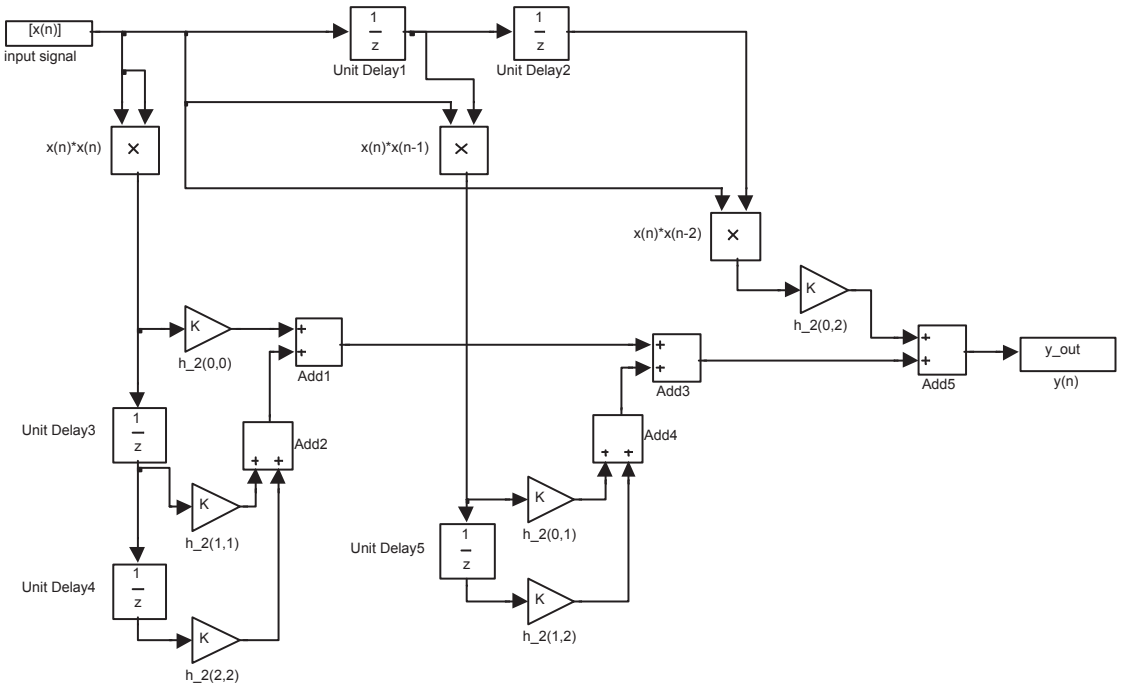

Figure 2.5: Realization of a quadratic operator using Simulink.

- *Feedback block-oriented* (FBO) *model*, which consists of a static nonlinearity in the feedback path around a LTI system (see for instance [28] for an identification algorithm for this type of model).

These models have been successfully used to represent nonlinear systems in a number of practical applications in the areas of signal processing [29], communications and control theory [30]. In the next subsections, the Hammerstein and Wiener models will be discussed.

2.3.1 Hammerstein-Wiener Model

The Hammerstein-Wiener structure models dynamic systems using up to two static nonlinear blocks in series with a linear block. The input signal passes through the first nonlinear block, a linear block, and a second nonlinear block to produce the output signal, as shown in Fig. 2.6.

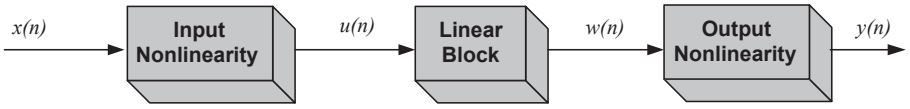

Figure 2.6: The Hammerstein-Wiener model.

This model structure represents a nonlinear system as a linear system that is modified by static input and output nonlinearities. Thus, the linear model provides a reference point for estimating the nonlinear contributions in a system.

The following general equation describes the Hammerstein-Wiener structure:

$$\begin{aligned} u(n) &= f\left(x(n)\right) \\ w(n) &= \tfrac{B(q^{-1})}{A(q^{-1})}u(n) \\ y(n) &= g\left(w(n)\right) \end{aligned} \tag{2.42}$$

where $x(n)$ and $y(n)$ are the input and output for the system, respectively. f and g are nonlinear functions corresponding to the input and output nonlinearities, respectively. For multiple inputs and multiple outputs, f and g are defined independently for each input and output channel. $u(n)$ and $w(n)$ are internal variables. $u(n)$ has the same dimension as $x(n)$, whereas $w(n)$ has the same dimension as $y(n)$. $B(q^{-1})$ and $A(q^{-1})$ in the linear dynamic block are polynomials in the unit delay operator q^{-1}. For multiple inputs and outputs, the linear block is a transfer function matrix.

If only the input nonlinearity is present, the model is called the *Hammerstein model*. If only the output nonlinearity is present, the model is called the *Wiener model*.

2.3.2 Hammerstein Model

The Hammerstein model of a nonlinear system is shown in Fig. 2.7.

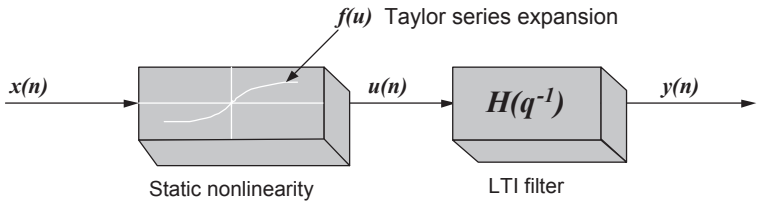

Figure 2.7: The Hammerstein model.

It consists of a static nonlinear mapping or gain followed by a linear dynamic block. The input signal $x(n)$ goes through the nonlinear static mapping block and gives an unobservable intermediate signal $u(n)$. Then $u(n)$ goes through the linear dynamic block to give the output signal $y(n)$, with $f[x(n)]$ denoting the nonlinear static gain function and the dynamics being modelled by a linear discrete transfer function $H(z)$. The Hammerstein model models the nonlinear effects as an input-dependent gain nonlinearity. If the static nonlinear function is assumed to be approximated by a finite polynomial expansion, the Hammerstein model can be described by the following equations

$$y(n) + a_1 y(n-1) + \ldots + a_k y(n-k) = b_1 u(n-1) + \ldots + b_k u(n-k) \tag{2.43}$$

and

$$u(n) = \gamma_1 x(n) + \gamma_2 x^2(n) + \ldots + \gamma_m x^m(n). \tag{2.44}$$

The intermediate variable $u(n)$ cannot be measured, but it can be eliminated from the equations. Substituting (2.44) into (2.43) we get

$$\begin{aligned} y(n) + a_1 y(n-1) + \ldots + a_k y(n-k) = \quad & b_1\gamma_1 x(n-1) + \ldots + b_1\gamma_m x^m(n-1) \\ & + b_2\gamma_1 x(n-2) + \ldots + b_2\gamma_m x^m(n-2) \\ & \qquad \vdots \\ & + b_k\gamma_1 x(n-k) + \ldots + b_k\gamma_m x^m(n-k) \end{aligned} . \tag{2.45}$$

Equation (2.45) can be written in operator form as

$$y(n) = \frac{B(q^{-1})}{A(q^{-1})} \sum_{i=1}^{m} \gamma_i x^i(n) = H(q^{-1}) \left(\sum_{i=1}^{m} \gamma_i x^i(n) \right) \tag{2.46}$$

where the polynomials $A(q^{-1})$ and $B(q^{-1})$ are expressed as

$$\begin{aligned} A(q^{-1}) &= 1 + a_1 q^{-1} + \ldots + a_k q^{-k} \\ B(q^{-1}) &= b_1 q^{-1} + \ldots + b_k q^{-k} \end{aligned} . \tag{2.47}$$

The orders of the polynomials are assumed to be the same, but this needs not be the case

in general.

2.3.3 Wiener Model

The Wiener system has the same two type of blocks as the Hammerstein system, but in the reverse order, as shown in Fig. 2.8.

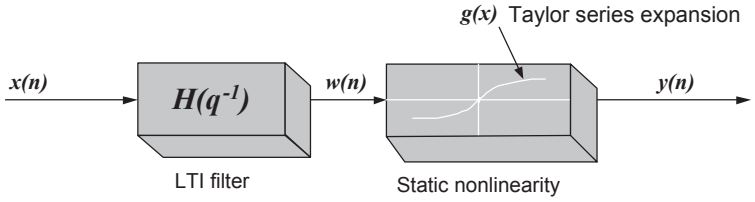

Figure 2.8: The Wiener model.

In the Wiener structure, the input signal $x(n)$ is transformed by the linear dynamic block to get $w(n)$, and then $w(n)$ goes through the static nonlinear block to produce $y(n)$. Mathematically, $x(n)$ and $y(n)$ can be expressed as

$$w(n) = H(q^{-1})x(n) \tag{2.48}$$

and

$$y(n) = g\left(w(n)\right). \tag{2.49}$$

If the static nonlinear function g is assumed to be approximated by a finite polynomial expansion, the Wiener model can be described by the following equation

$$y(n) = \sum_{i=1}^{m} \gamma_i \left[H(q^{-1})x(n)\right]^i. \tag{2.50}$$

2.4 Summary

Polynomial nonlinear systems were described in this chapter. They are used, in this thesis, to model different TR-UWB systems. After a brief introduction on the different classes of nonlinear systems, Volterra series expansions were presented. They constitute the basis of the theory of polynomial nonlinear systems. Further, the Wiener and Hammerstein models were revisited. They are part of the most frequently studied classes of polynomial nonlinear models.

Chapter 3

Channel Characterization

3.1 Introduction

The goal of this chapter is the description and discussion of an appropriate channel model for mobile radio systems, in general, and UWB radio systems, in particular.

Radio propagation in a mobile radio channel is determined mainly by its multipath nature. Multiple reflections, and sometimes a LOS component of the transmitted signal arrive at the receiver via different propagation paths and therefore with different amplitudes and delay times. As an effect of this, the narrowband received power fluctuates dramatically when observed as a function of location (or time) and frequency. In the early days of mobile systems, the communications engineer was mainly interested in the time-variability of narrowband channels, which were thus studied extensively [31]. By that time, transmission bandwidths were small, hence flat-fading was a reasonable assumption. As the systems evolved, demand for higher transmission rates has been increasing, making the channels time dispersion (which is equivalent to its frequency-selectivity) a major issue.

UWB systems transmit signals with very low power levels. Unavoidably, this constraint limits the range of UWB wireless links to values typically in few meters, making such systems suitable to short range indoor applications. This is the reason why most of the research works on the characterization and modelling of UWB channels have focused on indoor environments with both LOS and NLOS settings.

The following sections review the propagation mechanisms that have to be characterized by the channel model. Different UWB channels are introduced with emphasis on the standardized IEEE 802.15.4a realistic channel model.

3.2 Characterization of the Mobile Radio Channel

3.2.1 Components of a Multipath Channel Model

Three mechanisms should be distinguished in order to describe mathematically a multipath radio channel, namely:

- path loss

- shadowing
- multipath interference.

The first two are described by *large-scale* channel models, which essentially provide information about the average received power at a certain location. Path loss strictly describes the dependency of this average power on the distance between transmitter and receiver, while shadowing accounts for the fluctuations observed at a fixed distance, due to geometric features of the propagation environment. These fluctuations occur for instance because of the blocking of relevant propagation paths, e.g., the LOS component, as the mobile moves around. For mobile radio applications, the description of the effects of multipath interference is required, since the air-interface has to cope with them. These effects are often referred to as *small-scale* fading. Small-scale models are valid within (small) local areas, where the signal fluctuations due to shadowing and path loss can be neglected. The dimension of such a local area is therefore limited to approximately $5 \cdots 40\lambda$, where λ is the wavelength of the RF carrier [32].

The channel model considered in this section is limited to the description of small-scale effects. A set of average parameters specifies the channels behavior within a local area. These parameters are the normalized received power, P_0 , the Ricean K-factor, K, and the RMS delay spread, τ_{rms}. P_0 is the ratio of the received power P_{rx} and the transmitted power P_{tx}. It is important noting that each realization obtained from the model has varying instantaneous parameters denoted $\{\hat{P}_0, \hat{K}, \hat{\tau}_{rms}\}$, since the model is a stochastic one. The amount of variation of these parameters from the local-area parameters depends in particular on the observed bandwidth. When the bandwidth is much greater than the coherence bandwidth, then the multipath is completely resolved and the channel parameters vary little, since the individual multipath amplitudes do not change rapidly within a local area. However, if the system is narrowband, then the multipath is not resolved, and the path amplitudes at each resolvable delay time-bin (being spaced by the reciprocal of the bandwidth) vary due to multipath interference. This leads to the fluctuation of the instantaneous channel parameters within the local area [33].

3.2.2 Channel Impulse Response

In complex low-pass equivalent notation, the channel impulse response (CIR) is given as

$$h(t) = \sum_{n=0}^{\infty} \alpha_n e^{-j\theta_n} \delta(t - \tau_n), \tag{3.1}$$

where $\{\alpha_n\}$, $\{\theta_n\}$ and $\{\tau_n\}$ are the the propagation paths' amplitudes, phases, and delays, respectively. Normally, the delay of the first (shortest) ray is defined as $\tau_0 = 0$. Since $\tau_n > 0$ for $i > 0$, the channel impulse response is causal. Note that in a real environment, the parameters $\{\alpha_n\}$, $\{\theta_n\}$ and $\{\tau_n\}$ are time-variant. For the sake of simplicity, this time dependency was omitted in (3.1).

3.2.3 Channel Parameters

The channel parameters P_0 ,K and τ_{rms} are defined from the static power delay profile (PDP), which is a function derived from the CIR. The PDP specifies the ray-power versus time delay, and is given as

$$p_h(t) = \sum_{n=0}^{\infty} \alpha_n^2 \delta(t - \tau_n). \tag{3.2}$$

As the ray phases are dropped in this equation, the channel parameters must be constant within the local area, provided that the propagation paths are fully resolvable. The normalized received power is defined as the sum of the ray powers

$$P_0 = \sum_{n=0}^{\infty} \alpha_n^2. \tag{3.3}$$

The Ricean K-factor is the ratio of the dominant path's power to the power in the scattered paths, and it is defined as

$$K = \frac{\alpha_{n,max}^2}{P_0 - \alpha_{n,max}^2}, \tag{3.4}$$

where $\alpha_{n,max}^2 = \max_n\{\alpha_n^2\}$. The K-factor specifies the depth of the fades within a local area. Larger K-factors relate to shallower fades, and smaller K-factors relate to deeper fades. In the presence of a LOS, the first ray is the dominant one, implying that $\alpha_{n,max} = \alpha_0$ at $\tau_0 = 0$.

The RMS delay spread, defined as the second central moment of the PDP, is written as

$$\tau_{rms} = \sqrt{\bar{\tau^2} - \bar{\tau}^2}, \tag{3.5}$$

where $\bar{\tau^m} = \sum_{n=0}^{\infty} \tau_n^m \alpha_i^2 / P_0$, for $m = \{1, 2\}$. τ_{rms} is an important parameter for specifying the time extent of the dispersive channel. It also characterizes the frequency-selectivity, since τ_{rms} is related to the average number of fades per bandwidth, and to the average bandwidth of the fades [32].

3.2.4 Channel Description

The channel is characterized by its delay power spectrum (or average power delay Profile - APDP), $P_h(t) = \mathsf{E}\{h^2(t)\} = \mathsf{E}\{\sum_{n=0}^{\infty} \alpha_n^2 \delta(t - \tau_n)\}$. The expected power of ray at delay τ_n given by

$$\mathsf{E}\left\{\alpha_n^2 | \tau_n\right\} = \begin{cases} \rho^2 & n = 0 \\ \frac{P_h(\tau_n)}{\lambda(\tau_n)} & n > 0 \end{cases}, \tag{3.6}$$

where $\lambda(\tau_n)$ [rays/s] is the density of arriving rays, being a function of the excess delay time t. ρ^2 is the power of the dominant path, given by

$$\rho^2 = \alpha_{n,max}^2 = P_0 \frac{K}{K+1}. \tag{3.7}$$

In agreement with measurements reported in [34], the shape of the APDP is defined as shown in Fig. 3.1.

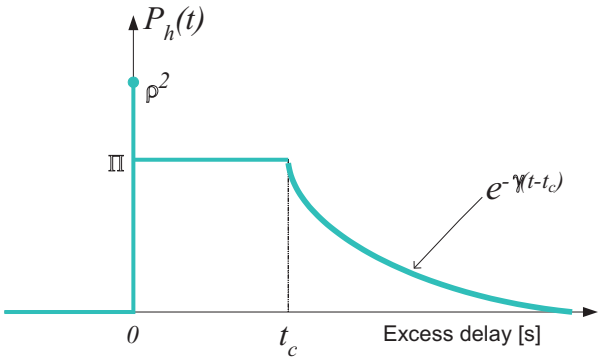

Figure 3.1: Model of the average power delay profile

It is specified by four parameters:

- ρ^2 - the normalized power of the direct ray
- Π [1/s] - the normalized power density of the constant-level part
- t_c [s] - the duration of the constant level part
- γ [1/s] - the decay exponent of the exponentially decaying part.

Mathematically, the APDP [W/s] can be written as

$$P_h(t) = \begin{cases} 0 & t < 0 \\ \rho^2\delta(t) & t = 0 \\ \Pi & 0 < t \leq t_c \\ \Pi e^{-\gamma(t-t_c)} & t > t_c \end{cases}. \tag{3.8}$$

The exponentially decaying APDP is a good approximation for most practical channels, which is implemented by letting $t_c = 0$. The existence of a LOS ray at $t = 0$ implies that the fading envelope distribution is Ricean. Rayleigh fading channels have $\rho = 0$.

The relationship between channel parameters defined in subsection 3.2.3 and the parameters $\{\rho, \Pi, \gamma, t_c\}$ is presented below.
P_0 relates to the APDP as

$$P_0 = \int_0^\infty P_h(t)dt = \rho^2 + \Pi\left[t_c + \frac{1}{\gamma}\right]. \tag{3.9}$$

For the special case of the exponentially decaying APDP ($t_c = 0$), we have

$$P_0 = \int_0^\infty P_h(t)dt = \rho^2 + \frac{\Pi}{\gamma}. \tag{3.10}$$

The K-factor characterizes the amplitude distribution of Ricean channels, relating the power of the direct path to the power of the scattered paths.

$$K = \frac{\rho^2}{P_0 - \rho^2} = \frac{\rho^2}{\Pi\left[t_c + \frac{1}{\gamma}\right]}. \tag{3.11}$$

The RMS delay spread τ_{rms} was defined in (3.5) as a function of $\bar{\tau}$ and $\bar{\tau^2}$. $\bar{\tau}$ is expressed as

$$\bar{\tau} = \int_0^\infty \tau \frac{P_h(t)}{P_0} dt = \Pi\left[\frac{t_c^2}{2} + \frac{t_c}{\gamma} + \frac{1}{\gamma^2}\right], \tag{3.12}$$

and $\bar{\tau^2}$ can be written as

$$\bar{\tau^2} = \int_0^\infty \tau^2 \frac{P_h(t)}{P_0} dt = \Pi\left[\frac{t_c^3}{3} + \frac{t_c^2}{\gamma} + \frac{2t_c}{\gamma^2} + \frac{2}{\gamma^3}\right]. \tag{3.13}$$

From (3.12), (3.13) and (3.11), τ_{rms} is expressed as

$$\tau_{rms} = \frac{1}{\gamma}\sqrt{\frac{1}{K+1}\frac{u_3}{u_1} - \frac{1}{(K+1)^2}\frac{u_2^2}{u_1^2}}, \tag{3.14}$$

where $u_1 = t_c\gamma + 1$, $u_2 = t_c^2\gamma^2/2 + t_c\gamma + 1$ and $u_3 = t_c^3\gamma^3/3 + t_c^2\gamma^2 + 2t_c\gamma + 2$.
If $t_c = 0$, we have

$$\tau_{rms} = \frac{1}{\gamma}\frac{\sqrt{2K+1}}{K+1}. \tag{3.15}$$

Finally, from (3.7) and (3.11), we have

$$\Pi = \frac{P_0}{K+1}\frac{\gamma}{u_1}. \tag{3.16}$$

If $t_c = 0$, we have

$$\Pi = \frac{P_0}{K+1}\gamma. \tag{3.17}$$

Let us define the maximum excess delay as the delay time where the exponentially decaying part has decreased by about 43 dB. Such attenuation is reached if the duration of the exponentially decaying part is exactly $t_{exp} = 10/\gamma$, leading to the maximum delay spread $t_{max} = t_c + t_{exp} = t_c + 10/\gamma$. Expressed in terms of channel parameters, we have

$$t_{max} = t_{rms}(u+10)\frac{u_1(K+1)}{\sqrt{u_1 u_3(K+1) - u_2^2}}, \tag{3.18}$$

which simplifies for $t_c = 0$ to

$$t_{max} = 10 t_{rms}\frac{K+1}{\sqrt{2K+1}}. \tag{3.19}$$

It can be seen that t_{max} and t_{rms} are related by a factor which is function of K, t_c and γ. A typical realization of the CIR ($\Re e\{h(t)\}$) and its associated PDP are illustrated in Fig. 3.2 (a) and (b) respectively, with channel parameters shown in Tab. 3.1.

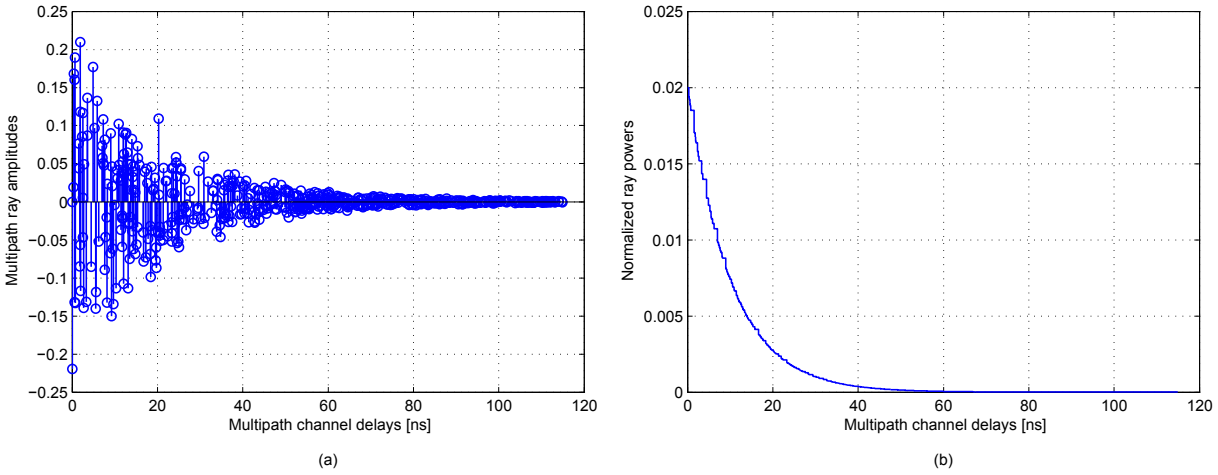

Figure 3.2: A typical channel realization (a) Channel impulse response; (b) Associated power delay profile.

t_c	P_0	K	λ	τ_{rms}	ρ^2	γ	Π
[ns]		NLOS	[rays/ns]	[ns]		[ns^{-1}]	
0	1	0	5	10	0	0.1	0.1

Table 3.1: Simulation values of the channel parameters.

3.3 Standardized Channel Models for UWB Communications

3.3.1 Overview

In UWB systems, the intended radiation can cover a bandwidth of almost 10 GHz. This large bandwidth can give rise to new effects. For example, only few multipath components overlap within each resolvable delay bin, so the central limit theorem is no more applicable, and the amplitude fading statistics are no longer Rayleigh. Also, there can be delay bins into which no multipath components fall, and thus are empty. It is then necessary to characterize the likelihood that this happens, and that an empty bin is followed by a full one. A channel model taking into account those characteristics is the well-known Saleh-Valenzuela (S-V) indoor channel model [35]. It is based on measurements utilizing low power ultra-short pulses (of width 10 ns and center frequency 1.5 GHz) in a medium-size, two-storey office building. In the S-V model, multipath components arrive at the receiver in groups (clusters). Cluster arrivals are Poisson distributed with rate Λ. Within each cluster, subsequent arrivals are also Poisson distributed with rate $\lambda > \Lambda$. With $\alpha_{l,k}$ denoting the gain of the kth multipath component of the lth cluster, having phase $\theta_{l,k}$, the CIR can be expressed as

$$h(t) = \sum_{l=0}^{L-1} \sum_{k=0}^{K-1} \alpha_{l,k} e^{j\theta_{l,k}} \delta(t - T_l - \tau_{l,k}). \tag{3.20}$$

The gains $\alpha_{l,k}$ of the kth component in the lth cluster are independent Rayleigh random variables with power $\mathrm{E}\{\alpha_{l,k}^2\}=\mathrm{E}\{\alpha_{0,0}^2\}e^{-T_l/\Gamma}e^{-\tau_{l,k}/\gamma}$, where Γ is the cluster decay factor, γ is the ray decay factor. T_l is the delay of the lth cluster, $\tau_{l,k}$ is the delay of the kth multipath component relative to the lth cluster arrival time T_l. The phases $\theta_{l,k}$ are uniformly distributed, i.e., for a bandpass system, the phase is taken as a uniformly distributed random variable from the range $[0,2\pi)$. K is the number of multipath components within a cluster, while L is the number of clusters.

To come up with a statistical model, channel realizations are identified either in the frequency domain by frequency sweeping or in the time domain using impulsive signals. In November 2002, the channel modelling subcommittee of the IEEE 802.15.3a Task Group recommended a channel which captures the aforementioned works, as well as recent refinements [36]. Because the clustering phenomenon has been experimentally confirmed, the standardized channel model is basically a modified version of the S-V model. To reach an analytically manageable channel model, the total number of paths is defined as the number of multipath arrivals with expected power within 10 dB from that of the strongest arrival path. The Rayleigh distribution in the S-V channel model is replaced by the log-normal distribution. The phases $\theta_{l,k}$ are also constrained to take values 0 or π with equal probability to account for signal inversion due to reflection, yielding a real-valued channel model. With path gains normalized to have unit energy, a log-normal random variable is introduced to account for shadowing (large-scale fading).

The Task Group 802.15.4a has the mandate to develop an alternative physical layer

for sensor networks and similar devices, working with the IEEE 802.15.4 MAC layer. The main goals for this new standard are energy-efficient data communications with data rates between 1kbit/s and several Mbit/s; additionally, the capability for geolocation plays an important role. The channel modelling subgroup started its activities at the meeting in September 2003 (Singapore), and submitted its final report in September 2004 (Berlin). The proposed IEEE 802.15.4a channel model was aimed at modelling attenuation and delay dispersion [37]. The former includes both shadowing and average path loss, while the latter describes the PDP and the small-scale fading statistics, with parameters such as RMS delay spread, number of multipath components carrying x% of the energy, etc... This channel model can be used for UWB systems spanning frequency range 100-1000 MHz and 2-10 GHz.

3.3.2 The IEEE 802.15.4a Channel Model

The key features of the 802.15.4a Channel Model are

- d^{-n} law for the path loss
- frequency dependence of the path loss
- modified S-V model:
  - arrival of paths in clusters
  - Poisson distribution for ray arrival times
  - possible delay dependence of cluster decay times
  - some NLOS environments have first increase, then decrease of power delay profile
- Nakagami-distribution of small-scale fading, with different m-factors for different components
- block fading: channel stays constant over data burst duration.

Path Loss Model

By definition, the attenuation undergone by an electromagnetic wave in transit between a transmitter and receiver in a communication system is called *path loss* or *path attenuation*. Path loss may be due to many effects, such as: free space loss, refraction, reflection, diffraction, clutter, aperture-medium coupling loss and absorption. The path loss in a narrowband system is conventionally defined as

$$PL(d) = \frac{\mathsf{E}\{P_{rx}(d, f_c)\}}{P_{tx}}, \tag{3.21}$$

where d is the distance between transmitter and receiver, f_c is the center frequency, and the expectation $\mathsf{E}\{\cdot\}$ is taken over an area that is large enough to allow averaging out of

the shadowing as well as the small-scale fading. A frequency-dependent path loss related to wideband path loss, as suggested in [38] is defined as

$$PL(f,d) = \mathsf{E}\{\int_{f-\Delta f/2}^{f+\Delta f/2} \left|H\left(\tilde{f},d\right)\right|^2 d\tilde{f}\}, \tag{3.22}$$

where $H(f,d)$ is the transfer function from transmitter antenna connector to receiver antenna connector, and Δf is chosen small enough so that diffraction coefficients, dielectric constants, etc., can be considered constant within that bandwidth. The total path loss is obtained by integrating over the whole bandwidth of interest. To simplify computations, it is assumed that the path loss as a function of the distance and frequency can be written as a product of the terms

$$PL(f,d) = PL(f)PL(d). \tag{3.23}$$

The frequency dependence of the path loss is given as [39]

$$\sqrt{PL(f)} \propto f^{-\kappa}. \tag{3.24}$$

The distance dependence of the path loss in dB is described by

$$PL(d) = PL_0 + 10n\log_{10}\left(\frac{d}{d_0}\right), \tag{3.25}$$

where the reference distance d_0 is set to 1 m, and PL_0 is the path loss at the reference distance. n is the path loss exponent. The path loss exponent also depends on the environment, and on whether a LOS connection exists between the transmitter and receiver or not. LOS path loss exponents in indoor environments range from 1.0 in a corridor to about 2 in an office environment. NLOS exponents typically range from 3 to 7. The above model includes the effects of the transmit and the receive antenna, as it defines the path loss as the ratio of the received power at the receiver antenna connector, divided by the transmit power (as seen at the transmitter antenna connector).

Fading Statistics

1. Shadowing

Shadowing, or *large-scale fading*, is defined as the variation of the local mean around the path loss. Also this process is fairly similar to the narrowband fading. The path loss in dB can be written as

$$PL(d) = PL_0 + 10n\log_{10}\left(\frac{d}{d_0}\right) + S, \tag{3.26}$$

where S is a Gaussian-distributed random variable with zero mean and standard deviation σ_S.

2. Power Delay Profile

The discrete-time impulse response, in complex baseband, of the S-V model was expressed in (3.20). The number of clusters L is an important parameter of the model, and it is assumed to be Poisson-distributed

$$p_L(L) = \frac{(\bar{L})^L e^{-\bar{L}}}{L!}. \tag{3.27}$$

The distributions of the cluster arrival times are given by a Poisson process

$$p(T_l/T_{l-1}) = \Lambda e^{[-\Lambda(T_l - T_{l-1})]}, \quad l > 0 \tag{3.28}$$

where Λ is the cluster arrival rate, assumed to be independent of l. The classical S-V model also uses a Poisson process for the ray arrival times. Due to the divergence in the fitting for the indoor residential, and indoor and outdoor office environments, ray arrival times are modelled with mixtures of two Poisson processes as follows

$$p\left(\tau_{l,k}|\tau_{l,k-1}\right) = \beta\lambda_1 e^{\left[-\lambda_1\left(\tau_{l,k}-\tau_{l,k-1}\right)\right]} + (\beta-1)\lambda_2 e^{\left[-\lambda_2\left(\tau_{l,k}-\tau_{l,k-1}\right)\right]}, \quad k > 0 \tag{3.29}$$

where $p\left(\tau_{l,k}|\tau_{l,k-1}\right)$ is the conditional probability density function conditioning consecutive ray arrival times within a cluster. By definition $\tau_{l,0} = 0$. β is the mixture probability, while λ_1 and λ_2 are the ray arrival rates. For some environments, like industrial areas, a "dense" arrival of multipath components is observed, i.e., each resolvable delay bin contains significant energy. In that case, the concept of ray arrival rates loses its meaning, and a realization of the CIR based on a tapped delay line model with regular tap spacings is to be used.

Next, the cluster powers and cluster shapes are determined. The average power delay profile (APDP), which is the mean power of the different paths, is exponential within each cluster

$$\mathsf{E}\{|\alpha_{l,k}^2|\} = E_l \frac{1}{\gamma_l[(1-\beta)\lambda_1 + \beta\lambda_2 + 1]} e^{-\tau_{l,k}/\gamma_l}, \tag{3.30}$$

where E_l is the integrated energy of the lth cluster, and γ_l is the intra-cluster decay time constant. The cluster decay rates are found to depend linearly on the arrival time of the cluster

$$\gamma_l \propto k_\gamma T_l + \gamma_0, \tag{3.31}$$

where k_γ describes the increase of the decay constant with delay and γ_0 is a constant. The mean energy (normalized to γ_l), of the lth cluster follows in general an exponential decay

$$10\log(E_l) = 10\log\left(e^{-T_l/\Gamma}\right) + X_{cl}, \tag{3.32}$$

where X_{cl} is a normally distributed variable with standard deviation σ_{cl}. Γ is the cluster decay factor, and is typically around 10-30 ns, while widely differing values (between 1 and 60 ns) have been reported for the intra-cluster constant γ_l.

For the NLOS case of some environments (office and industrial), the shape of the PDP can be different, namely

$$\mathsf{E}\{|\alpha_{1,k}^2|\} = (1 - \chi e^{-\tau_{l,k}/\gamma_r}) e^{(-\tau_{l,k}/\gamma_1)} \frac{\gamma_1 + \gamma_r}{\gamma_1} \frac{E_1}{\gamma_1 + \gamma_r(1-\chi)}. \tag{3.33}$$

Here, the parameter χ describes the attenuation of the first component, the parameter γ_r determines how fast the APDP increases to its local maximum, and γ_1 determines the decay at late times.

3. Small-scale fading

The distribution density of the small-scale amplitudes is Nakagami

$$p_x(x) = \frac{2}{\Gamma(m)} \left(\frac{m}{\Omega}\right)^m x^{2m-1} e^{-\frac{mx^2}{\Omega}}, \tag{3.34}$$

where $m \geq 1/2$ is the is the Nakagami m-factor, $\Gamma(m)$ is the gamma function, and Ω is the mean-square value of the amplitude. A conversion to a Rice distribution is approximately possible with the conversion equations [40]

$$m = \frac{(K+1)^2}{2K+1} \tag{3.35}$$

and

$$K = \frac{\sqrt{(m^2 - m)}}{m - \sqrt{(m^2 - m)}}, \tag{3.36}$$

where K and m are the Ricean factor and Nakagami-m factor, respectively. The parameter Ω corresponds to the mean power, and its delay dependence is thus given by the APDP above. The m-parameter is modelled as a lognormally distributed random variable, whose logarithm has a mean $\mu_m(\tau)$ and standard deviation σ_m. Both of these can have a delay dependence

$$\begin{aligned} \mu_m(\tau) &= m_0 - k_m\tau \\ \sigma_m(\tau) &= \hat{m}_0 - \hat{k}_m\tau. \end{aligned} \tag{3.37}$$

For the first component of each cluster, the Nakagami factor is modelled differently. It is assumed to be deterministic and independent of delay

$$m = \tilde{m}_0. \tag{3.38}$$

A realization of the CIR of the IEEE 802.15.4a Channel Model for indoor office environment with NLOS scenario is illustrated in Fig. 3.3 (a). It can be observed a certain delay before receiving the first path with significant energy. Fig. 3.3 (b) depicts 100 CIR realizations with random first path arrival delays. The channel parameters are shown in Tab. 3.2.

The APDP, averaged over 100 channel realizations, is shown in Fig. 3.4.

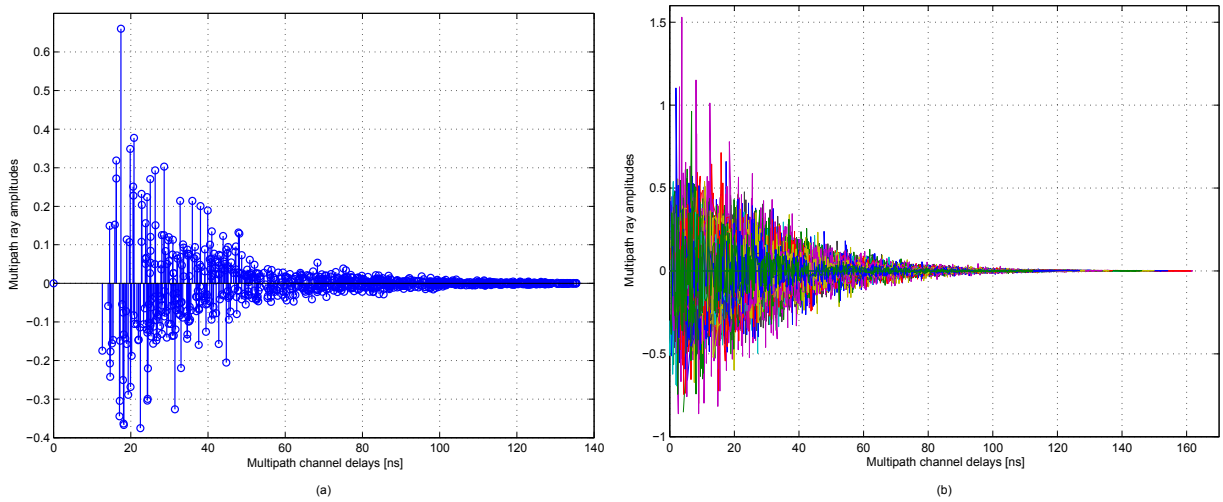

Figure 3.3: Channel impulse response from the IEEE 802.15.4a Channel Model (a) a single realization; (b) multiple realizations.

	Office	
	LOS	NLOS
Path loss		
n	1.63	3.07
σ_S	1.9	3.9
PL_0	36.6	51.4
Power delay profile		
$\bar{L}$	5.4	3.1
Λ [ns^{-1}]	0.016	0.19
λ_1, λ_2 [rays/ns], β	0.19, 2.97, 0.0184	0.11, 2.09, 0.0096
Γ[ns]	14.6	19.8
k_γ, γ_0 [ns]	0, 6.4	0, 11.2
σ_{cl} [dB]	3	3
Small-scale fading		
m_0 [dB], k_m	0.42, 0	0.5, 0
$\hat{m}_0$, $\hat{k}_m$	0.31, 0	0.25, 0
χ		0.78
γ_r, γ_1		15.21, 11.84

Table 3.2: Channel parameters for indoor office environment.

The different channel realizations are studied independently in terms of their RMS delay spreads and the number of significant paths they contain with more than 85% of total energy, as shown in Fig. 3.5 and Fig. 3.6, respectively. The average RMS delay

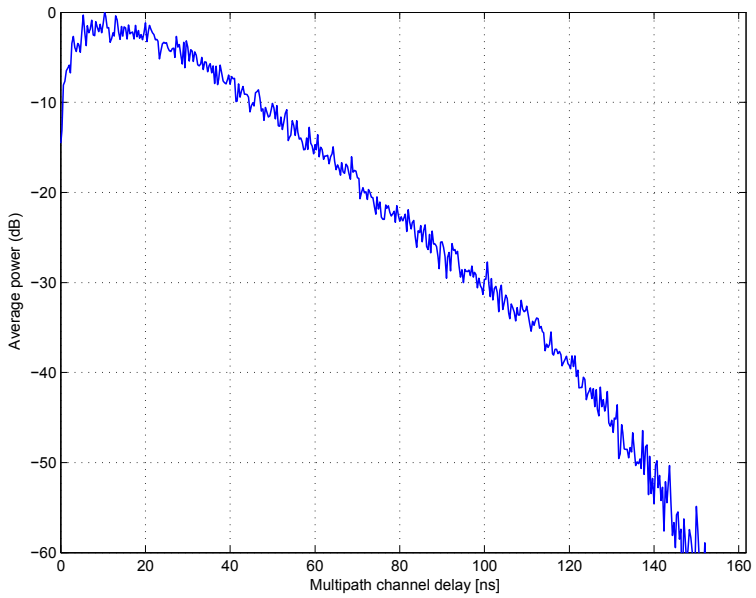

Figure 3.4: Average power delay profile.

spread is $\bar{\tau}_{rms} = 12$ ns. The average number of significant paths capturing more than 85% of total energy is 40.5.

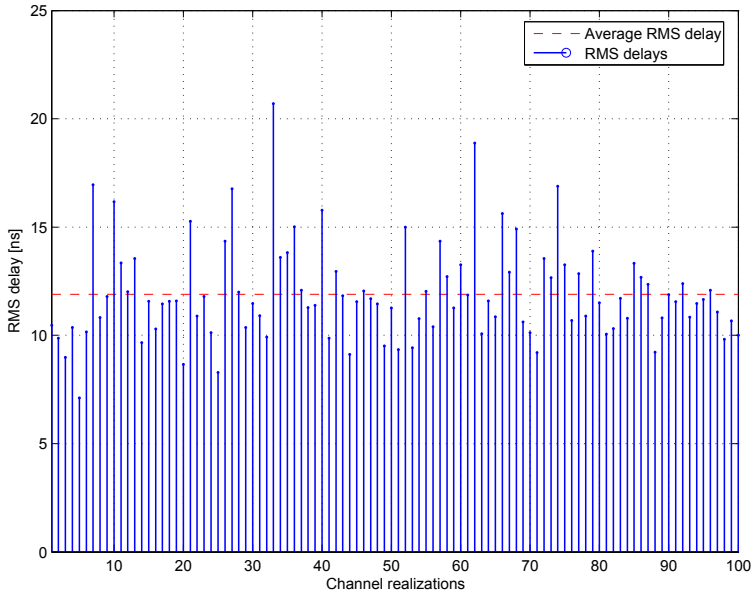

Figure 3.5: RMS delay spreads for different CIR realizations.

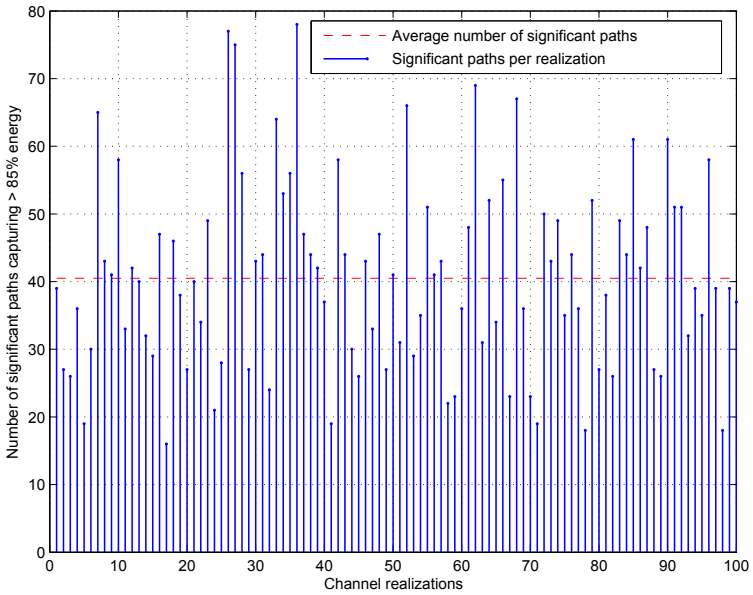

Figure 3.6: Number of significant paths.

3.4 Summary

This chapter presented first a generic mobile radio channel, identifying the components influencing its description. The CIR and the APDP were expressed analytically. The channel parameters characterizing this channel model are:

- P_0 - the normalized received power
- K - the Ricean K-factor
- τ_{rms} - the RMS delay spread
- ρ^2 - the normalized power of the direct ray
- Π - the normalized power density of the constant-level part
- t_c - the duration of the constant level part
- γ - the decay exponent of the exponentially decaying part.

Further, standardized channels models are introduced, especially the IEEE 802.15.4a channel model. The statistical modelling of path loss, path inter-arrival times, large-scale and small-scale fadings was presented, as well as the determination of the cluster powers and cluster shapes. The considered parameters characterizing the IEEE 802.15.4a channel model are:

- PL_0 - the path loss at 1m distance

- n - the path loss exponent
- σ_S - the shadowing standard deviation
- A_{ant} - the normalized power of the direct ray
- $\bar{L}$ - the mean number of clusters
- Λ - the inter-cluster arrival rate
- $\lambda_1, \lambda_2, \beta$ - the ray arrival rates (mixed Poisson model parameters)
- Γ - the inter-cluster decay constant
- k_γ, γ_0 - the intra-cluster decay time constant parameters
- σ_{cl} - the cluster shadowing variance
- m_0, k_m - the Nakagami-m factor mean
- $\hat{m}_0, \hat{k}_m$ - the Nakagami-m factor variance
- $\tilde{m}_0$ - the Nakagami-m factor for strong components
- γ - the decay exponent of the exponentially
- γ_r, γ_1, χ - parameters for alternative PDP shape

The standardized IEEE 802.15.4a UWB channel model, as it is claimed, match better the measurements, making it a more realistic channel model. However, the log-normal distribution and the shadowing factor render this model less tractable for theoretical performance analysis and quantification of the channel-induced diversity. For this reason the channel model presented in section 3.2 will be used whenever performance analysis is concerned. For most other simulations in this thesis the standardized model will be used.

Chapter 4

Transmitted Reference Systems

4.1 Introduction

The key motivations for using UWB communications systems are the ability of UWB signals to finely resolve multipath components, as well as the availability of technology to implement and generate UWB signals with relatively low complexity. Non-coherent receivers with no channel estimation have been proposed in [41, 42] to make the UWB technology attractive for applications where low cost and low power consumption are playing an important role, as in the case of WSNs. Compared with coherent receivers that are facing great design challenges, non-coherent autocorrelation receivers (AcR) represent an interesting solution for realizing low complexity UWB systems. They can also detect data with synchronization inaccuracy as large as one frame duration [43].

In AcR front-ends for UWB communications systems, the received signal consisting of a train of pulses is delayed and correlated with itself. Hence, each information-conveying pulse is coupled with an unmodulated pulse. Generally, the first pulse is known as the "*reference pulse*" and the second pulse is the "*data pulse*". The reference pulse acts as a template for the AcR. Data can be applied, for instance, by differentially modulating the polarity of the data pulse with respect to the reference pulse. The delay line in an AcR front-end, also known as "*pulse-pair*" correlator, is matched to the lag between the reference and the data pulses. The overall system is called a *Transmitted-Reference* (TR) AcR [41], [43] - [49].

Generally, in AcRs the reference pulse is corrupted by noise and interference, which is an inherent disadvantage. If the data rate of such systems is increased, interference among multiple pulses becomes one of the most fundamental deteriorating effects, due to multipath propagation. This is known as *Inter-Frame Interference* (IFI) if interference between multiple pulses of one data symbol is referred to. It is termed *Inter-Symbol Interference* (ISI) if interference among consecutive data symbols is considered.

The TR-UWB systems considered, in this thesis, are the *Differential Transmitted-Reference*(DTR) UWB system [50], the *Low-Duty-Cycle* (LDC) DTR-UWB system [51] and the *Dual-Pulse* (DP) TR-UWB system [52]. Discrete-time equivalent system models for these TR-UWB systems are derived in [15], [51] and [52]. In this chapter, their delay-dependence is studied. The delay-dependent system models accurately relate the

transmitted data bits d_i and the timing offset τ to the test statistics at the decision device $\hat{z}[i]$. The data model can be written as

$$\hat{z}[i] = z_\tau[i] + z_{\tau\nu}[i]. \tag{4.1}$$

The decision variable $\hat{z}[i]$ comprises a data and delay dependent term $z_\tau[i]$ and a noise term $z_{\tau\nu}[i]$.

Using the data model and the concept of minimum distance receiver, the BER of low-complexity TR-UWB systems was derived, where ISI is minimal or absent.

4.2 TR-UWB Signal and Systems Models

4.2.1 TR-UWB Transmission Schemes

Narrowband signals (i.e. sinusoidal and quasi-sinusoidal signals) have the unique property of keeping their sinusoidal shape during forms of signal conversions such as addition, subtraction, differentiation and integration. *Shape* is defined here as the law of change of a signal in time. The waveforms of sinusoidal and quasi-sinusoidal signals keep a shape identical to that of the original function and may differ only in their amplitude and time shift, or phase. On the contrary, the UWB signal has a nonsinusoidal waveform that can change shape while processing the above specified transformations.

When a UWB signal is generated and transmitted to the antenna in a form of a current pulse, the first change of the UWB signal shape occurs during pulse radiation, since the intensity of the radiated electromagnetic field varies proportionally with the derivative of the antenna current. The second change occurs during signal propagation through the multipath channel. The third change of the shape occurs during signal reception, for the same reason as for signal radiation. Thus, when a Gaussian pulse is transmitted, the second derivative of the Gaussian pulse is expected at the UWB receiver front-end. Hence, the standard pulse-shape assumed in theoretical work is the second derivative of a Gaussian pulse (Gaussian doublet), given by

$$\omega(t) = \left[1 - 4\pi(t/t_m)^2\right] e^{-2\pi(t/t_m)^2}. \tag{4.2}$$

This pulse is confined in time to an interval $[0,T_\omega)$.

A DTR-UWB system sends data as a stream of very narrow pulses. Let us assume each data symbol is transmitted via N_f consecutive pulses/frames, where i is the symbol index. A known random sequence $b_j \in \{-1,+1\}$ is differentially modulated on the time-hopped pulses, where $j \in \{0,1,...,N_f-1\}$ is the pulse index within a symbol. The differentially modulated pulse-polarities are obtained as $a_{i,j+1} = a_{i,j}b_j d_i$ and $a_{i+1,0} = a_{i,N_f-1}b_{N_f-1}d_i$, where d_i is the i^{th} data symbol, $d_i \in \{-1,+1\}$. The transmitted signal is written as

$$s(t) = \sum_{i=0}^{\infty} \sum_{j=0}^{N_f-1} a_{i,j}\tilde{\omega}(t - t_{i,j}), \tag{4.3}$$

where $\tilde{\omega}(t)$ is the transmitted pulse shape and $t_{i,j} = (j + iN_f)T_f + c_j = C_j + iT_s$. T_f is the average spacing between two pulses, i.e., the average frame duration, c_j is the known TH sequence and $C_j = c_j + jT_f$. $\{C_j\}$ are the relative pulse timings within a symbol. T_s is the symbol duration. The time shifts between consecutive pulses are given as $D_j = t_{i,j+1} - t_{i,j}$. Since $d_i^2 = 1$, every second pulse of a symbol is not modulated by data. Each pulse is re-used as a reference and data pulse to increase the power efficiency. Indeed, the differential TR scheme transmits half the number of pulses that would transmit a conventional TR scheme. Let $s_i(t)$ be the i^{th} transmitted symbol waveform containing the N_f pulses, i.e.,

$$s_i(t) = \sum_{j=0}^{N_f-1} a_{i,j}\tilde{\omega}(t - iT_s - jT_f - c_j). \tag{4.4}$$

The transmitted signal is visualized in Fig. 4.1(a).

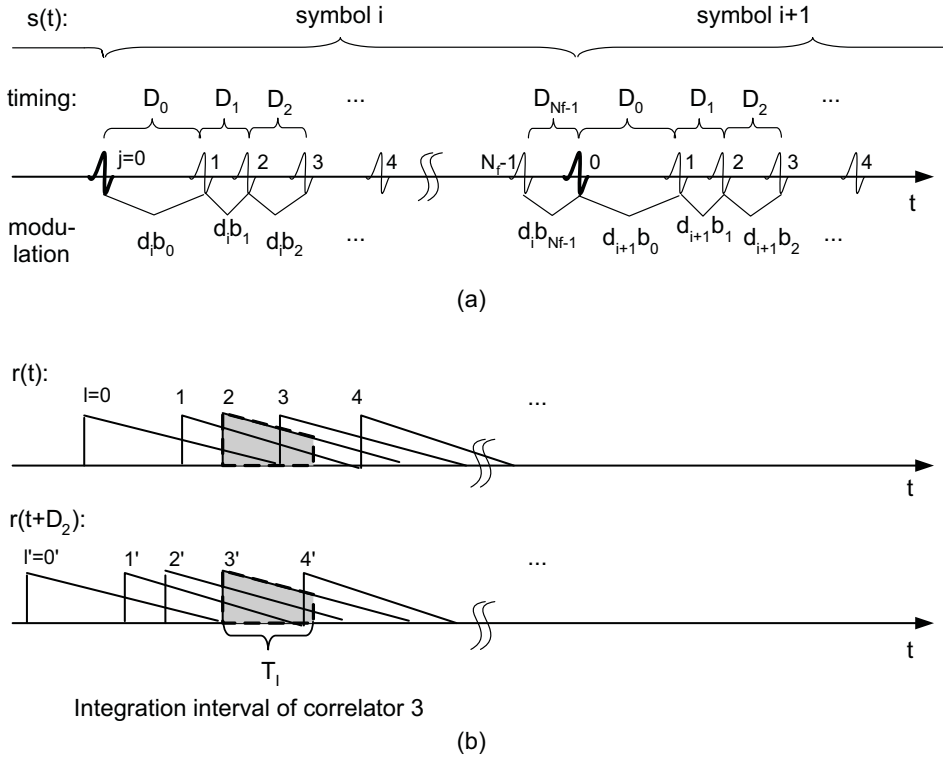

Figure 4.1: Diagram of the transmitted and received signals in DTR-UWB.

The burst-oriented LDC DTR-UWB system is fundamentally similar to a conventional DTR-UWB system. The difference is that the random sequence b_j is of length $N_f - 1$. This is because the polarity of the first pulse within a symbol is no more dictated by the polarity of the last pulse of the previous symbol. Hence, the differentially modulated pulse-polarities are obtained as $a_{i,j+1} = a_{i,j}b_j d_i$, $j \in \{0, 1, ..., N_f - 2\}$ and $a_{i+1,0} \in \{-1, +1\}$. The LDC DTR-UWB system, as conceived in [51], was designed for efficient narrowband

interference (NBI) mitigation and robustness in multiuser scenarios. Pulses are transmitted in short bursts, separated by comparably longer idle periods, making up a "low-duty-cycle" as shown in Fig. 4.2.

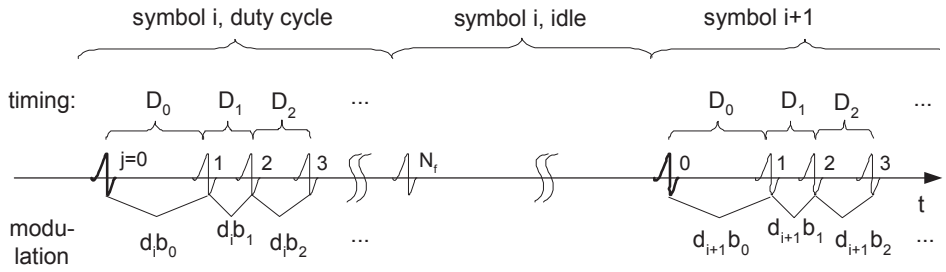

Figure 4.2: Diagram of transmitted signals for the burst oriented LDC DTR-UWB systems.

For a DP TR-UWB system, the unmodulated data pulse is followed at a delay D by the data-modulated pulse, as illustrated in Fig. 4.3. The timing of pulse $j = 0$ is $c_0 = 0$ and for $j = 1$ it is $c_1 = D$.

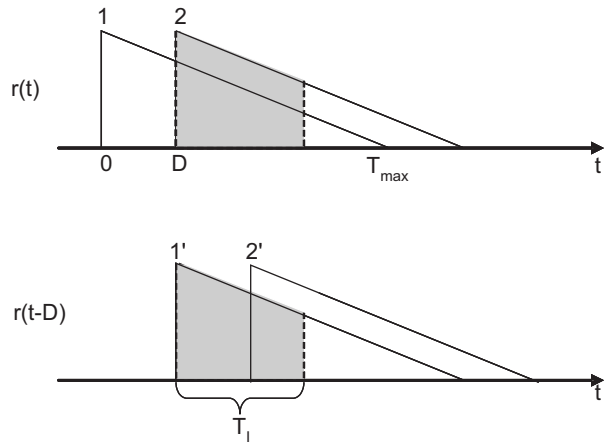

Figure 4.3: Received signal for a DP TR-UWB system.

4.2.2 TR-UWB Receiver Front-End

Let $\tilde{g}(t) = h(t) * \tilde{\omega}(t) = \sum_{n=0}^{\infty} \alpha_n \tilde{\omega}(t - \tau_n)$ be the overall channel capturing both pulse shaping by linear system components and multipath effects. $h(t)$ is a realization of a simulated CIR, generated according to the channel models presented in sections 3.2 and 3.3. It can also be a measured channel impulse response. The received noisy signal is expressed as

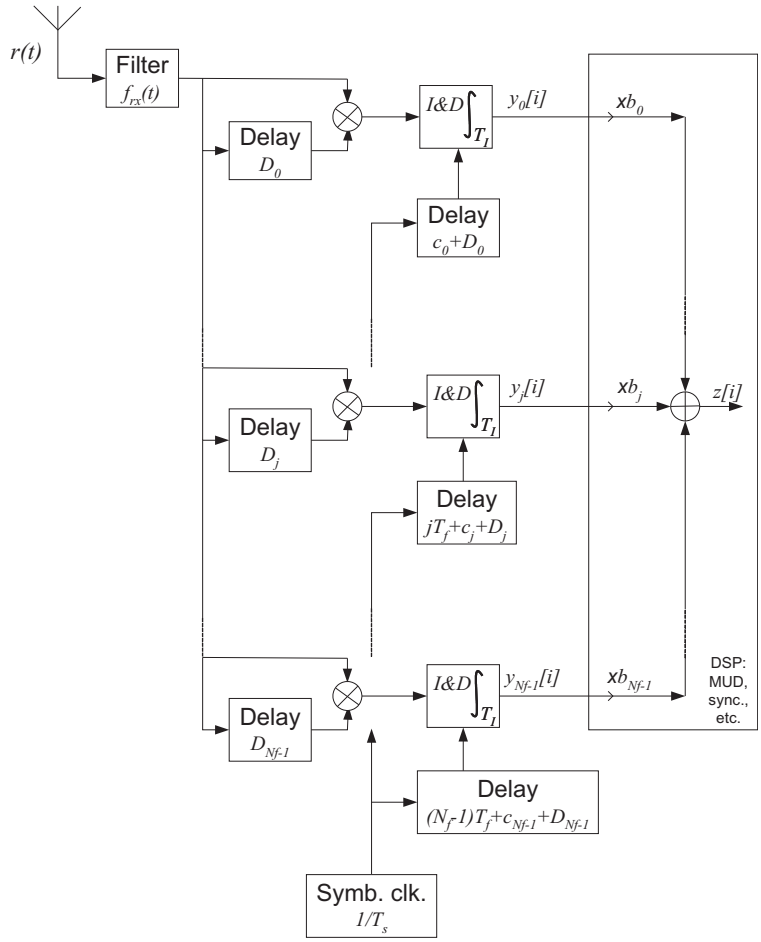

Figure 4.4: Receiver front-end for a DTR-UWB system.

$$r(t) = \sum_{i=0}^{\infty} \sum_{j=0}^{N_f-1} a_{i,j} \tilde{g}(t - iT_s - jT_f - c_j - \tau) + n(t), \tag{4.5}$$

where T_s is the symbol period, $\tau \in [0, T_s)$ is the timing delay and $n(t)$ represents noise.

A conventional DTR-UWB receiver front-end is shown in Fig. 4.4. It has at its input a bank of pulse-pair correlators, whose lags are matched to the time shifts D_j. While a conventional DTR-UWB receiver has $N_{cr} = N_f$ pulse-pair correlators, a LDC DTR-UWB receiver has $N_{cr} = N_f - 1$ pulse-pair correlators. In a DP TR-UWB receiver, a single correlator ($N_{cr} = 1$) is used for the detection of the pulse-pairs. Integration is performed over a time interval T_I, which can be selected to optimize the signal-to-noise ratio (SNR) of the AcR outputs [49, 53, 54].

The outputs of the *Integrate-and-Dump* (I&D) blocks, after being sampled at the symbol rate, are coherently combined by removing the chip-level modulation b_j. We obtain

$$z[i] = \sum_{j=0}^{N_f-1} y_j\,[i]\,b_j, \tag{4.6}$$

where

$$y_j[i] = \int_{t_{i,j}}^{t_{i,j}+T_I} \hat{r}(t)\hat{r}(t+D_j)dt, \tag{4.7}$$

and

$$\hat{r}(t) = r(t) * f_{rx}(t) = r_\tau(t) + \nu(t), \tag{4.8}$$

where $r_\tau(t)$ is the delay-dependent noise-free received signal. $f_{rx}(t)$ denotes a front-end analog filter in the receiver. The filtered noise process $\nu(t) = n(t) * f_{rx}(t)$ is characterized by its autocorrelation function

$$R_\nu(\kappa) = E\{\nu(t)\nu(t+\kappa)\} = \frac{N_0}{2} f_{rx}(\kappa) * f_{rx}(-\kappa), \tag{4.9}$$

where $N_0/2$ is the double-sided power spectral density of the receiver front-end noise.

Using (4.7) and (4.8), we obtain

$$\begin{aligned} y_j[i] &= \textstyle\int_{t_{i,j}}^{t_{i,j}+T_I} r_\tau(t)r_\tau(t+D_j)dt + \int_{t_{i,j}}^{t_{i,j}+T_I} \nu(t)r_\tau(t+D_j)dt \\ &\quad + \textstyle\int_{t_{i,j}}^{t_{i,j}+T_I} r_\tau(t)\nu(t+D_j)dt + \int_{t_{i,j}}^{t_{i,j}+T_I} \nu(t)\nu(t+D_j)dt \\ &= y_{\tau j}[i] + \nu_{\tau 1 j}[i] + \nu_{\tau 2 j}[i] + \nu_{3j}[i]. \end{aligned} \tag{4.10}$$

4.3 Equivalent TR-UWB Systems Models

Among all the TR-UWB systems presented in section 4.2, only the DTR-UWB system is prone to ISI in the case the average frame duration T_f is less than the maximum delay spread of the multipath channel T_m. In this thesis, the LDC DTR-UWB and DP TR-UWB are chosen in such a way that they mitigate ISI effects.

4.3.1 System with ISI: Volterra Equivalent Model

In [15] a discrete-time Volterra equivalent system model is derived for DTR-UWB systems in a multipath channel, where both IFI and ISI are present. In this subsection, a review of the system modelling is presented, introducing the delay parameter.

Equivalent System Model without Noise

The noise-free delay-dependent received signal can be written as

$$r_\tau(t) = \sum_{i=-\infty}^{\infty} \sum_{l=0}^{N_p-1} a_{i,l} g(t - t_{i,l} - \tau), \tag{4.11}$$

where $g(t) = \tilde{g}(t) * f_{rx}(t)$ is the filtered overall channel. $y_{\tau j}[i]$ is expressed as

$$\begin{aligned} y_{\tau j}[i] &= \sum_{n=-\infty}^{\infty} \sum_{l=0}^{N_f-1} a_{i+n,l} g(t - t_{i+n,l} - \tau) \\ &\quad \cdot \sum_{n'=-\infty}^{\infty} \sum_{l'=0}^{N_f-1} a_{i+n',l'} g(t - t_{i+n',l'} - \tau) dt \\ &= \sum_{n=-\eta}^{1} \sum_{l=0}^{N_f-1} \sum_{n'=-\eta}^{1} \sum_{l'=0}^{N_f-1} a_{i+n,l} a_{i+n',l'} \\ &\quad \cdot I_g(t_{i,j} - t_{i+n,l} - \tau, t_{i,j} - t_{i+n,l} - \tau + T_I; D_j + t_{i+n,l} + c_l - c_{l'}), \end{aligned} \tag{4.12}$$

where $I_g(t_1, t_2; \zeta) = \int_{t_1}^{t_2} g(t) g(t + \zeta) dt$. Equation (4.12) accounts for the interference from all pulses of η previous and one consecutive symbol. $\eta = \lceil T_m / T_s \rceil$ is the memory length, where $\lceil \cdot \rceil$ represents the ceiling function defined by $\lceil x \rceil = \min \{n \in \mathbb{Z} | x \leq n\}$. This IFI was depicted in Fig. 4.1(b). Equation (4.12) can be written as

$$y_{\tau j}[i] = \mathbf{a}^T[i] \mathbf{Y}_{\tau j} \mathbf{a}[i], \tag{4.13}$$

where $\mathbf{a}[i] = [a_{i,0}, a_{i,1}, \ldots, a_{i,N_f-1}, a_{i,N_f}]^T$ represents the polarities of all pulses. The elements of the $N_p(\eta + 2) \times N_p(\eta + 2)$ matrix $\mathbf{Y}_{\tau \mathrm{j}}$ are given by

$$\begin{aligned} &[\mathbf{Y}_{\tau j}]_{(n+\eta)N_p+l+1,(n'+\eta)N_p+l'+1} \\ &= I_g(c_j - nT_s - c_l - \tau, c_j - nT_s - c_l - \tau + T_I; D_j + (n - n')T_s + c_l - c_{l'}) \end{aligned} \tag{4.14}$$

$\forall$ n,$n' \in \{-\eta, -\eta + 1, \ldots, 1\}$ and l,$l' \in \{0, 1, \ldots, N_p - 1\}$.

The noise-free signal term $z_\tau[i] = \sum_{j=0}^{N_f-1} y_{\tau j}[i] b_j$ can be modelled as

$$z_\tau[i] = \sum_{j=0}^{N_f-1} b_j \mathbf{a}^T[i] \mathbf{Y}_{\tau j} \mathbf{a}[i] = \mathbf{a}^T[i] \mathbf{Z}_\tau \mathbf{a}[i], \tag{4.15}$$

where $\mathbf{Z}_\tau = \sum_{j=0}^{N_f-1} b_j \mathbf{Y}_{\tau j}$. It is demonstrated in [15] that (4.15) constitutes a discrete-time Volterra model of order two, having the transmitted symbols $\{d_i\}$ at its input. The data and code dependent vector $\mathbf{a}[i]$ is expressed as

$$\mathbf{a}[i] = a_{i-\eta,0} \mathbf{B}(\mathbf{p} + \mathbf{P}\mathbf{d}[i]), \tag{4.16}$$

where $\mathbf{d}[i] = [d_{i-\eta}, d_{i-\eta+1}, \ldots, d_i, d_{i+1}]^T$, $\mathbf{B} = \mathrm{diag}[1, b_0, b_0 b_1, \ldots]$, $[\mathbf{B}]_{k,k} = \prod_{\mu=0}^{k-2} b_{\mu \bmod N_f}$, $k = 1, 2, \ldots, N_f$. $\mathbf{P} = \mathbf{I}_{\eta+2} \otimes \mathbf{s}$ is a block-diagonal matrix of dimension $N_f(\eta+2) \times (\eta+2)$, with the length N_f selection vectors $\mathbf{s} = [0, 1, 0, 1, \ldots, 1]^{\mathrm{T}}$ at its main diagonal. $\otimes$ denotes the Kronecker product. The length $N_f(\eta+2) \times (\eta+2)$ vector $\mathbf{p} = \mathbf{i}_{\eta+2} \otimes (\mathbf{i}_{\mathrm{N_f}} - \mathbf{s})$ contain ones at the elements of $\mathbf{a}[i]$ that are not data dependent. $\mathbf{I}_N$ and $\mathbf{i}_N$ denote an identity matrix of size $N \times N$ and an all-ones vector of length N, respectively. Using (4.15) and (4.16), a second-order Volterra model is obtained

$$\begin{aligned} z_\tau[i] &= (\mathbf{p} + \mathbf{P}\mathbf{d}[i])^T \mathbf{B}\mathbf{Z}_\tau \mathbf{B}(\mathbf{p} + \mathbf{P}\mathbf{d}[i]) \\ &= h_{\tau 0} + \mathbf{h}_{\tau 1}^T \mathbf{d}[i] + \mathbf{d}^T[i]\mathbf{H}_{\tau 2}\mathbf{d}[i], \end{aligned} \tag{4.17}$$

where $h_{\tau 0} = \mathbf{p}^T \mathbf{B}\mathbf{Z}_\tau \mathbf{B}\mathbf{p}$, $\mathbf{h}_{\tau 1} = \mathbf{P}^T \mathbf{B}(\mathbf{Z}_\tau + \mathbf{Z}_\tau^T)\mathbf{B}\mathbf{p}$ and $\mathbf{H}_{\tau 2} = \mathbf{P}^T \mathbf{B}\mathbf{Z}_\tau \mathbf{B}\mathbf{P}$. The bias term $h_{\tau 0}$ is due to the interference among the (channel's response to) fixed reference pulses plus interference between equally modulated data pulses. The linear model coefficient $\mathbf{h}_{\tau 1}$ relates to the interference between unmodulated reference and modulated data pulses. The nonlinear product terms $\mathbf{H}_{\tau 2}$ are attributed to interference between differently modulated pulses of any two different data symbols. Thus, nonlinear product terms appear only if significant ISI is present.

Multiuser Equivalent System Model

In a multiuser (MU) equivalent system model, nonlinear terms also exist if data symbols of various users overlap [15]. An equivalent system model can be derived for the MU case by including the interfering users' pulse polarities in the $\mathbf{a}[i]i$-vectors and extending $\mathbf{Y}_j$-matrices with all channels' auto- and cross-correlation values for any pulse-pairs. The MU Volterra model comprises $\mathbf{d}[i]$-vectors extended by the other users' data and correspondingly extended coefficient vectors and matrices.

Equivalent Noise Model

The three noise terms in (4.10) are considered for the noise analysis. We encounter two "*linear*" terms $\nu_{\tau 1 j}[i]$ and $\nu_{\tau 2 j}[i]$ which depend on the received signal, and a "*product*" noise term $\nu_{3j}[i]$. Following [15] and [55], all three noise components at the output of the correlators are assumed to be zero-mean Gaussian noise variables. This requires that the noise process $\nu(t)$ is zero mean, that $R_\nu(D_j) \approx 0$, $\forall j$, and that the integration-time by noise-bandwidth product $T_I W \gg 1$.

The noise component of the decision variable $z[i]$ is defined by $z_{\tau\nu}[i] = \hat{z}[i] - z_\tau[i]$. Using (4.6) and (4.10), we obtain

$$\begin{aligned}\mathsf{E}\{z_{\tau\nu}[i]z_{\tau\nu}[i+\iota]\} &= \sum_{j=0}^{N_f-1}\sum_{j=0}^{N_f-1} b_j b_{j'}[\mathsf{E}\{\nu_{\tau 1j}[i]\nu_{\tau 1j'}[i+\iota]\} \\ &+\mathsf{E}\{\nu_{\tau 1j}[i]\nu_{\tau 2j'}[i+\iota]\}+\mathsf{E}\{\nu_{\tau 2j}[i]\nu_{\tau 1j'}[i+\iota]\} \\ &+\mathsf{E}\{\nu_{\tau 2j}[i]\nu_{\tau 2j'}[i+\iota]\}+\mathsf{E}\{\nu_{3j}[i]\nu_{3j'}[i+\iota]\}],\end{aligned} \tag{4.18}$$

since $\nu_{3j}[i]$ is uncorrelated from $\nu_{\tau 1j'}[i]$ and $\nu_{\tau 2j'}[i]$, $\forall\ j, j'$.

The delay and data-dependent covariance of the linear noise terms is expressed by quadratic forms

$$\mathsf{E}\{\nu_{\tau mj}[i]\nu_{\tau m'j'}[i+\iota]\} = \frac{N_0}{2}\mathbf{a}^T[i]\mathbf{V}_{\tau\iota,j,j'}^{(\nu_m\nu_{m'})}\mathbf{a}[i], \tag{4.19}$$

for $m, m' \in \{1,2\}$. It is zero for $|\iota| > 1$ [15]. We derived the expression of the matrix $\mathbf{V}_{\tau\iota,j,j'}^{(\nu_m\nu_{m'})}$ as

$$\begin{aligned}&[\mathbf{V}_{\tau\iota,j,j'}^{(\nu_m\nu_{m'})}]_{(n+\eta)N_f+l+1,(n'+\eta)N_f+l'+1} \\ &= \tfrac{2}{N_0}\int_{t_{i,j}}^{t_{i,j}+T_I} g(t+(-1)^{m+1}D_j - t_{i+n,l} - \tau) \\ &\cdot \int_{t_{i+\iota,j'}-t}^{t_{i+\iota,j'}-t} g(t+\kappa+(-1)^{m'+1}D_{j'} - t_{i+n',l'} - \tau)R_n(\kappa)d\kappa dt.\end{aligned} \tag{4.20}$$

These expressions can be evaluated numerically if the channel response $g(t)$ is known. For the noise product we obtain

$$\begin{aligned}\mathsf{E}\{\nu_{3j}[i]\nu_{3j'}[i+\iota]\} &\approx \delta[\iota]\delta[j-j']T_I\int_{-\infty}^{\infty} R_n^2(\kappa)d\kappa \\ &\approx \delta[\iota]\delta[j-j']T_I\tfrac{N_0^2}{4}\int_{-\infty}^{\infty}|F_{rx}(f)|^4 df,\end{aligned} \tag{4.21}$$

where $F_{rx}(f)$ is the Fourier transform of the receiver front-end.

Finally, the noise model for the decision variable can be expressed by

$$\mathsf{E}\{z_{\tau\nu}[i]z_{\tau\nu}[i+\iota]\} = \frac{N_0}{2}\mathbf{a}^T[i]\mathbf{W}_{\tau\iota}\mathbf{a}[i] + \delta[\iota]\frac{N_0^2}{4}N_2, \tag{4.22}$$

where $\mathbf{W}_{\tau\iota} = \sum_{m,m'}\sum_{j,j'} b_j b_{j'}\mathbf{V}_{\tau\iota,j,j'}^{(z_m z_{m'})}$, $\iota = 0$ (noise variance) or $\iota = 1$ (noise covariance), and $N_2 = N_f T_I\int_{-\infty}^{\infty}|F_{rx}(f)|^4 df$.

Model Illustration

The equivalent system model is depicted in Fig. 4.5, where the upper branch with the "Volterra System I" represents the data model, while the lower branch introduces the data dependency of the noise variance, described by the "Volterra System II".

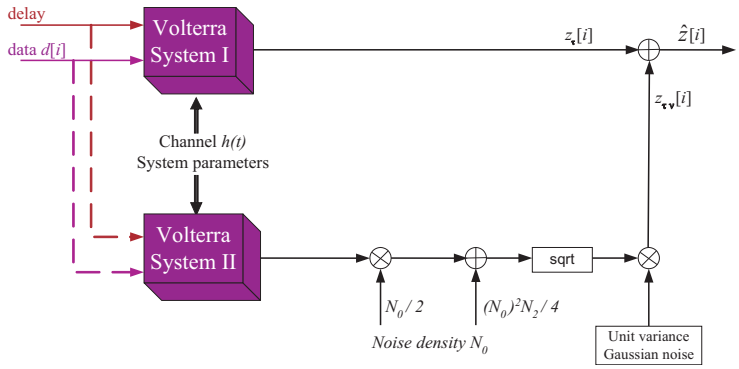

Figure 4.5: 2^{nd} order Volterra equivalent system model of the DTR-UWB system.

Model Validation

We select the pulse $\omega(t)$ as the second derivative of the Gaussian pulse with unit energy and duration $T_\omega = 0.7$ ns. The pulse parameter $\tau_m = 0.2877$. The pulse is sampled using the sampling period $T_{samp} = 0.05$ ns. The precise position of the pulses in each channel impulse response has been oversampled in order to represent better the unquantized ray arrival times. The pulse position resolution is $T_{res} = 0.005$ ns. The DTR-UWB system's key parameters are $N_f = 10$, $T_f = 10$ ns, $T_s = 100$ ns, $\eta = 1$ and $T_I = 20$ ns. Random time hopping (TH) codes were used. All the system parameters are summarized in Tab. 4.1

DTR-UWB system parameters	T_ω [ns]	τ_m [ns]	T_{samp} [ns]	T_f [ns]	T_I [ns]	T_s [ns]	N_f	N_{cr}
	0.7	0.2877	0.05	10	20	100	10	10

Table 4.1: DTR-UWB system and simulation parameters

A NLOS channel has been simulated with an exponentially decaying delay profile at RMS delay spread of $\tau_{rms} = 10$ ns using the channel model presented in section 3.2. The channel simulator generates an unquantized vector of ray arrival times according to a Poisson process with a mean ray arrival rate of $\lambda = 5$ ns^{-1} and a vector of Rayleigh distributed ray magnitudes with random polarity. The SNR is defined as the ratio between the symbol energy and the noise variance, i.e., SNR$= E_s/\sigma^2 = N_f E_b/\sigma^2$, where $E_b = \int_{-\infty}^{+\infty} g^2(t)dt$ and σ^2 is the noise variance. E_s is the symbol energy.

The validation of the delay-dependent equivalent system and noise models is shown in Fig. 4.6 and Fig. 4.7. The data dependence of the models is first studied, followed by the delay dependence.

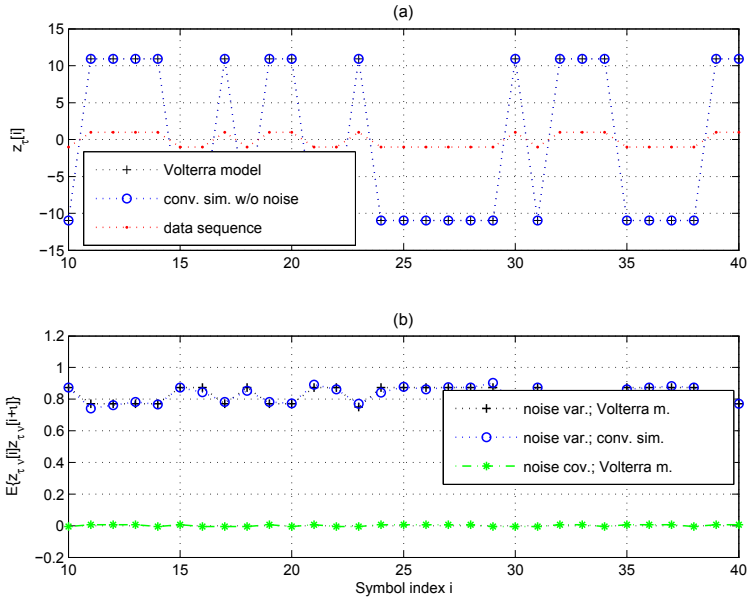

Figure 4.6: Simulated receiver output compared with the output of the second-order Volterra equivalent system. (a) Noise-free case ($\tau = 0$). (b) Data dependence of the noise (co)-variance at SNR= 30 dB ($\tau = 0$).

We compare the noise-free receiver output, simulated by processing the received signal according to the elements of the receiver front-end shown in Fig. 4.4 (conventional simulations) with the output of the second-order Volterra equivalent system. In Fig. 4.6(a) the sampled output of the conventional simulation is marked by "$\circ$". Plus characters "$+$" show the output of the equivalent system model at these sampling instants. Perfect agreement between these two demonstrates the suitability of the proposed equivalent system model. Fig. 4.6(b) compares the variance of the additive noise $\mathrm{var}\{z_{\tau\nu}[i]\}$ at the same set of observed decision variables, for a conventional simulation "$\circ$" and for the noise model in (4.22) "$+$". In the conventional simulation runs, one of 1000 independent noise processes has been added to the receiver front-end at a time, while using a constant data sequence and channel realization. The simulation results show a significant data-dependence of the noise variance, whereas the noise covariance, illustrated by asteriks "$*$" is insignificant.

After the data dependence, the delay-dependence is illustrated. Fig. 4.7 shows the simulated receiver output compared with the output of the second-order Volterra equivalent system model $z_\tau[i]$, with and without delay. It can be seen that $z_\tau[i]$ decreases with increase in time delay, as expected. In fact, $z_\tau[i]$ decays exponentially with respect to τ as is shown in Fig. 4.8, where $\mathsf{E}\{z_\tau[i]/E_s\}$ is obtained by averaging $z_\tau[i]/E_s$ over 1000 channel realizations, for $d_i = 1$ and a constant data sequence. On the other hand, under the same simulation

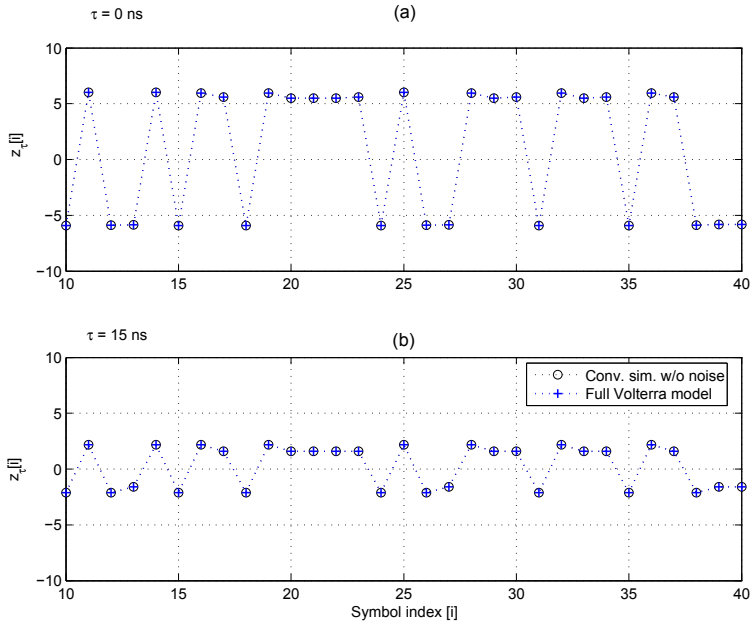

Figure 4.7: Simulated receiver output compared with the output of the second-order Volterra equivalent system. (a) Noise-free case without delay. (b) Noise-free case with delay $\tau = 15$ ns.

conditions, it can be observed that $\mathsf{E}\{z_{\tau\nu}[i]\}$ and $\mathsf{E}\{z^2_{\tau\nu}[i]\}$ do not exhibit such significant delay-dependence, as shown in Fig. 4.9.

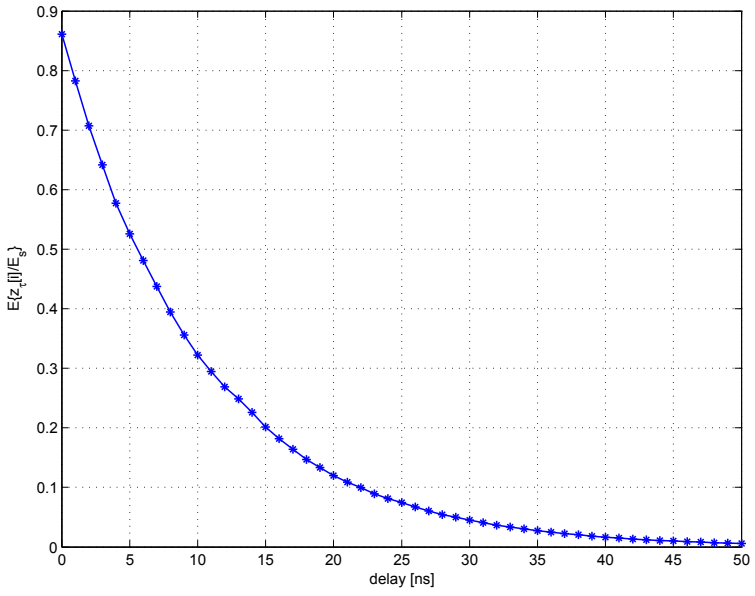

Figure 4.8: Normalized average delay-dependent noise-free decision variable

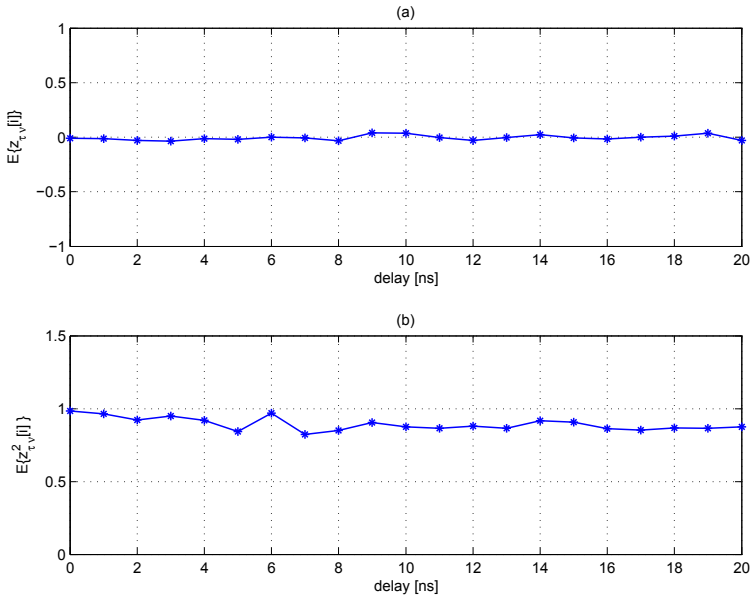

Figure 4.9: (a) Average output noise versus delay (SNR= 30 dB). (b) Variance of output noise versus delay (SNR= 30 dB).

4.3.2 Systems without ISI

In this subsection, low complexity TR-UWB systems without ISI are addressed.

DTR-UWB Systems

For DTR-UWB systems with no ISI the memory length $\eta = 0$. The noise-free delay dependent equivalent system model $z_\tau[i]$ and the variance of the noise variable $z_{\tau\nu}[i]$ for ISI-free DTR-UWB systems are expressed as

$$z_\tau[i] = h_{\tau 0} + h_{\tau 1} d_i, \tag{4.23}$$

and

$$\text{var}\{z_{\tau\nu}[i]\} = \frac{N_0}{2}(h_{\tau\nu,0} + h_{\tau\nu,1} d_i) + \frac{N_0^2}{4} N_f T_I W, \tag{4.24}$$

where

$$\begin{aligned} h_{\tau 0} &= \mathbf{p}^{\mathrm{T}}\mathbf{B}\mathbf{Z}_\tau\mathbf{B}\mathbf{p} + \text{trace}(\mathbf{q}^{\mathrm{T}}\mathbf{B}\mathbf{Z}_\tau\mathbf{B}\mathbf{q}) \\ h_{\tau 1} &= \mathbf{p}^{\mathrm{T}}\mathbf{B}(\mathbf{Z}_\tau + \mathbf{Z}_\tau^{\mathrm{T}})\mathbf{B}\mathbf{q}. \end{aligned} \tag{4.25}$$

Let $\mathbf{b}$ be a vector containing the code sequence $\{b_j\}$. In the diagonal matrix $\mathbf{B}$, the spreading code $\mathbf{b}$ is represented in the form of an accumulated product, $\mathbf{B}$=diag[1 b_0 $b_0 b_1$ $b_0 b_1 b_2$ ...]. $\mathbf{q}$ is a vector of length N_f, which in this case is identical to the selection vector $\mathbf{s} = [0, 1, 0, 1, \ldots, 1]^{\mathrm{T}}$. The length N_f vector $\mathbf{p}$ is defined as $\mathbf{p} = \mathbf{i}_{N_f} - \mathbf{s}$. $\mathbf{Z}_\tau = \sum_{j=0}^{N_{cr}-1} b_j \mathbf{Y}_{\tau j}$,

where $\mathbf{Y}_{\tau \mathrm{j}}$ is a $N_{cr} \times N_{cr}$ matrix containing the autocorrelation integrals $I_g(t_1, t_2; \zeta)$. $\mathbf{Y}_{\tau j}$ is expressed as

$$[\mathbf{Y}_{\tau j}]_{l+1,l'+1} = I_g(t_{i,j} - t_{i,l} - \tau, t_{i,j} - t_{i,l} + T_I - \tau; D_j + t_{i,l} - t_{i,l'}), \tag{4.26}$$

$\forall\, l, l' \in \{0, 1, \ldots, N_{cr} - 1\}$. $W = \int_{-\infty}^{\infty} |F_{rx}(f)|^4 df$ is the equivalent input bandwidth of the receiver, where $F_{rx}(f)$ is the Fourier transform of the front-end filter $f_{rx}(t)$.

The coefficients of the noise model, $h_{\tau\nu,0}$ and $h_{\tau\nu,1}$ (4.24), are obtained in a similar way like $h_{\tau 0}$ and $h_{\tau 1}$ in (4.25), replacing the matrix $\mathbf{Z}_\tau$ by a matrix

$$\mathbf{W}_\tau = \sum_{m,m'} \sum_{j,j'} b_j b_{j'} \mathbf{V}_{\tau,j,j'}^{(m,m')}, \tag{4.27}$$

where

$$\begin{aligned} [\mathbf{V}_{\tau,j,j'}^{(m,m)}]_{l+1,l'+1} \;=\; & \tfrac{2}{N_0} \int_{t_{i,j}}^{t_{i,j}+T_I} g(t + (-1)^{(m+1)} D_j - t_{i,l} - \tau) \\ & \cdot \int_{t_{i,j'}-t}^{t_{i+,j'}-t} g(t + \kappa + (-1)^{(m+1)} D_{j'} - t_{i,l'} - \tau) R_\nu(\kappa) d\kappa dt, \end{aligned} \tag{4.28}$$

for $m, m' \in \{1, 2\}$.

DP TR-UWB Sytems

The equivalent system and noise models for DP TR-UWB systems have been derived in [52]. The expressions of the noise-free delay dependent equivalent system model $z_\tau[i]$ and variance of the noise variable $z_{\tau\nu}[i]$ for DP TR-UWB systems are the same as in (4.23) and (4.24), respectively. For these systems the coefficients $h_{\tau 0}$, $h_{\tau 1}$, are given as

$$\begin{aligned} h_{\tau 0} &= I_g(-\tau, T_I - \tau; D) + I_g(-D - \tau, T_I - D - \tau; D) \\ h_{\tau 1} &= I_g(-\tau, T_I - \tau; 0) + I_g(-D - \tau, T_I - D - \tau; 2D). \end{aligned} \tag{4.29}$$

For $D \geq T_I$, $h_{\tau\nu,0}$ and $h_{\tau\nu,1}$ are expressed as

$$\begin{aligned} h_{\tau\nu,0} &\approx 2 I_g(-\tau, T_I - \tau; 0) = 2 h_{\tau 1} \\ h_{\tau\nu,1} &\approx 2 I_g(-\tau, T_I - \tau; D) = 2 h_{\tau 0}. \end{aligned} \tag{4.30}$$

4.4 Bit Error Rate Performance Analysis

In this section, the receiver statistics are analyzed from two perspectives; both perspectives allow for BER performance analysis to be performed. The first (widely accepted) perspective is to use a Gaussian approximation on the noise terms in the receiver statistics and determine their respective variances. The second approach is to use the equivalent system models of the receiver. The average BER is verified through simulation for different SNR

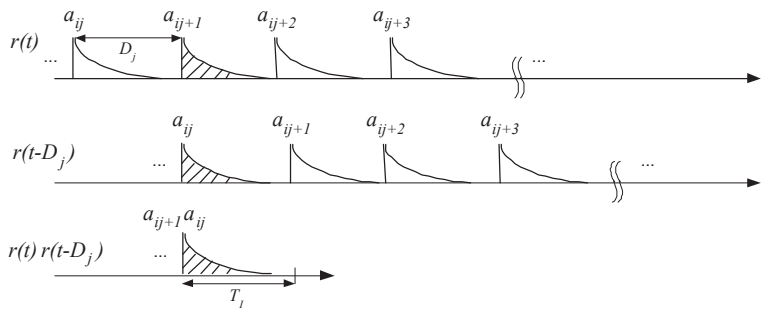

Figure 4.10: Diagram of the received signals in DTR-UWB (without IFI).

values. It is also compared to the average BER derived using the equivalent system model. Since the derivation of an analytic expression for the average BER would need to solve a complicated integral, we adopt another approach for computing the average BER, namely using the concept of *minimum distance receiver* [56].

4.4.1 Gaussian Approximations approach

As we presented in [57], the goal is to derive the receiver decision statistic in the absence of any kind of interference. Fig. 4.1(b) shows the correlator output for a duration of T_I in the presence of IFI and Fig. 4.10 shows the correlator output in the absence of noise and IFI. Equation (4.7) can be rewritten as

$$y_j[i] = \int_{t_{i,j}}^{t_{i,j}+T_I} [a_{i,j}g(t-t_{i,j}) + \nu(t)][a_{i,j+1}g(t-t_{i,j+1}) + \nu(t+D_j)]dt. \tag{4.31}$$

Since $t_{i,j+1} = D_j + t_{i,j}$, (4.31) can be expressed as

$$y_j[i] = \int_{t_{i,j}}^{t_{i,j}+T_I} [a_{i,j}g(t-t_{i,j}) + \nu(t)][a_{i,j+1}g(t-t_{i,j}-D_j) + \nu(t+D_j)]dt. \tag{4.32}$$

Making the appropriate change of variable in (4.32) we finally obtain

$$\begin{aligned} y_j[i] &= \int_0^{T_I} [a_{i,j}g(t) + \nu(t+t_{i,j})][a_{i,j+1}g(t-D_j) + \nu(t+t_{i,j}+D_j)]dt \\ &= \int_0^{T_I} a_{i,j+1}a_{i,j}g(t)g(t-D_j)dt + \int_0^{T_I} a_{i,j}g(t)\nu(t+t_{i,j}+D_j)dt + \\ &\quad \int_0^{T_I} a_{i,j+1}g(t-D_j)\nu(t+t_{i,j})dt + \int_0^{T_I} \nu(t+t_{i,j})\nu(t+t_{i,j}+D_j)dt. \\ &= y_{1j}[i] + y_{2j}[i] + y_{3j}[i] + y_{4j}[i]. \end{aligned} \tag{4.33}$$

Equation (4.6) can be rewritten as

$$\begin{aligned} z[i] &= \sum_{j=0}^{N_f-1} b_j y_{1j} + \sum_{j=0}^{N_f-1} b_j y_{2j} + \sum_{j=0}^{N_f-1} b_j y_{3j} \\ &\quad + \sum_{j=0}^{N_f-1} b_j y_{4j} \\ &= z_1[i] + z_2[i] + z_3[i] + z_4[i]. \end{aligned} \tag{4.34}$$

In (4.34) $z_1[i]$ is the signal term, while $z_2[i]$, $z_3[i]$ and $z_4[i]$ are all noise terms. Let T_m be the channel maximum excess delay. Since there is no IFI, $D_j > T_m \gg T_\omega$, then $\{\nu(t+t_{i,j}\}$ and $\{\nu(t+t_{i,j}+D_j\}$ can be regarded as uncorrelated and thus independent zero mean Gaussian random variables. The validity of this assumption is illustrated by Fig. 4.11, where the noise autocorrelation function is simulated for time delays in the interval $[-T_m, T_m]$. Hence $z_4[i]$ can be approximated as a zero mean random variable. $g(t)$ is zero mean for $t > T_\omega$ [50], thus $z_2[i]$ and $z_3[i]$ are independent zero mean Gaussian random variables. Finally, all the three noise terms in (4.34) can be approximated as independent zero-mean random variables whose variances, given by V_2, V_3 and V_4, are equal to the second moments of $z_2[i]$, $z_3[i]$ and $z_4[i]$, respectively.

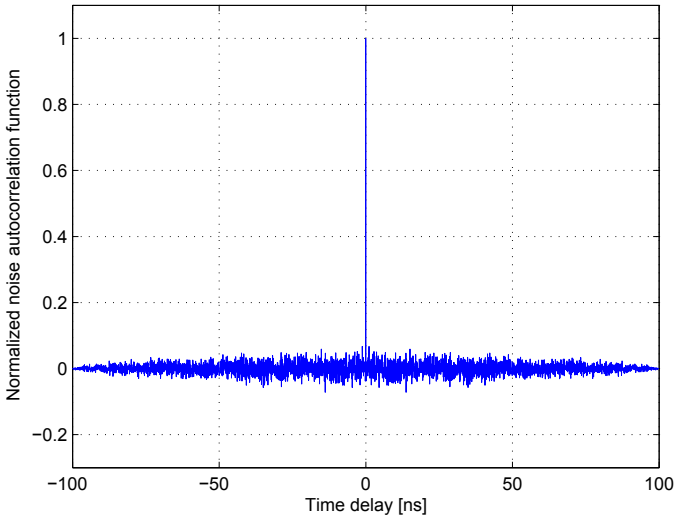

Figure 4.11: Simulated noise autocorrelation function.

Analysis of $z_1[i]$

In subsection 4.2.1 the differentially modulated pulse-polarities were expressed as $a_{i,j+1} = a_{i,j} b_j d_i$, which implies that $a_{i,j+1} a_{i,j} = b_j d_i$ and

$$z_1[i] = d_i \sum_{j=0}^{N_f-1} \int_0^{T_I} g(t - D_j)g(t)dt = d_i z_1. \tag{4.35}$$

z_1 is actually a random variable, considering several realizations of $g(t)$. Since the channel is quasi-static, $g(t-D_j)$ is the exact replica of $g(t)$ delayed by D_j. Thus, z_1 can be expressed as

$$z_1 = N_f \int_0^{T_I} g^2(t)dt. \tag{4.36}$$

Analysis of $z_2[i]$

$$z_2[i] = \sum_{j=0}^{N_f-1} \int_0^{T_I} a_{i,j}b_j g(t)\nu(t + t_{i,j} + D_j)dt. \tag{4.37}$$

Let $z_2[i] = \sum_{j=0}^{N_f-1} I_{2j}$, then $V_2 = \sum_{j=0}^{N_f-1} \mathsf{E}(I_{2j}^2)$, where

$$\mathsf{E}(I_{2j}^2) = \int_0^{T_I}\int_0^{T_I} \mathsf{E}\{a_{i,j}b_j g(t)\nu(t + t_{i,j} + D_j)a_{i,j}b_j g(\varrho)\nu(\varrho + t_{i,j} + D_j)\}dtd\varrho. \tag{4.38}$$

Considering that $g(t)$ and $\nu(t + t_{i,j} + D_j)$ are uncorrelated, we can split up the expectation term in two separate terms.

$$\mathsf{E}(I_{2j}^2) = \int_0^{T_I}\int_0^{T_I} \mathsf{E}\{g(t)g(\varrho)\}\mathsf{E}\{\nu(t + t_{i,j} + D_j)\nu(\varrho + t_{i,j} + D_j)\}dtd\varrho. \tag{4.39}$$

Equation (4.39) can be rewritten as

$$\mathsf{E}(I_{2j}^2) = \int_0^{T_I}\int_{-t}^{T_I-t} \mathsf{E}\{g(t)g(t + \kappa)\}\mathsf{E}\{\nu(t + t_{i,j} + D_j)\nu(t + \kappa + t_{i,j} + D_j)\}dtd\kappa, \tag{4.40}$$

where $\varrho = t + \kappa$. $\mathsf{E}\{g(t)g(t + \kappa)\} \approx \rho^2\omega(t)\omega(t + \kappa) + \tilde{P}_h(t)\phi_\omega(\kappa)$ [50], with $\tilde{P}_h(t) = \Pi e^{-\gamma t}$ and $\phi_\omega(\kappa) = \int_0^{T\omega} \omega(\mu)\omega(\mu + \kappa)d\mu$ is the autocorrelation of the received prototype pulse $\omega(t)$. We define $\phi_\omega(0) = 1$, i.e., the prototype pulse is assumed to have unit energy. $\mathsf{E}\{\nu(t + t_{i,j} + D_j)\nu(t + \kappa + t_{i,j} + D_j)\} = R_\nu(\kappa)$ is the noise autocorrelation function. If we assume that the received signal is passed through an ideal bandpass filter (BPF) with one-side bandwidth W and center frequency f_0, where W equals the bandwidth of the received signal, then

$$R_\nu(\kappa) = WN_0 \frac{\sin(\pi W\kappa)}{\pi W\kappa} \cos(2\pi f_0\kappa), \tag{4.41}$$

where N_0 is the noise power. The normalized prototype pulse and noise autocorrelation functions are shown in Fig. 4.12 and Fig. 4.13, respectively.

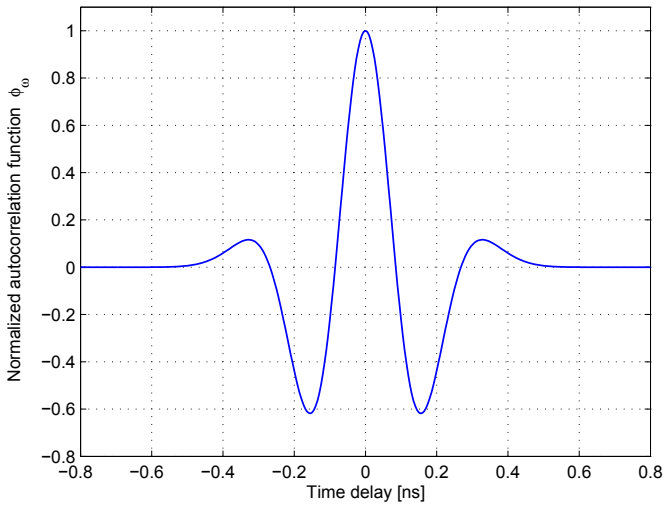

Figure 4.12: Autocorrelation function of the received prototype pulse.

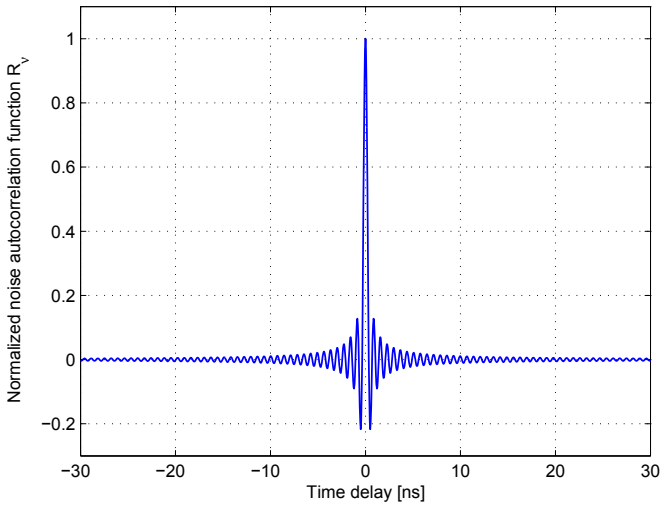

Figure 4.13: Noise autocorrelation function $R_\nu(\kappa)$.

Since $\rho^2 = 0$ (NLOS channel),

$$\mathsf{E}(I_{2j}^2) = \int_0^{T_I} \Pi e^{-\gamma t} dt \int_{-T_\omega}^{T_\omega} \phi_\omega(\kappa) R_\nu(\kappa) d\kappa. \tag{4.42}$$

Finally,

$$\begin{aligned} V_2 &= \tfrac{\Pi}{\gamma} \sum_{j=0}^{N_f-1} \left(1 - e^{-\gamma T_I}\right) \int_{-T_\omega}^{T_\omega} \phi_\omega(\kappa) R_\nu(\kappa) d\kappa \\ &= \tfrac{\Pi N_f \left(1-e^{-\gamma T_I}\right)}{\gamma} \int_{-T_\omega}^{T_\omega} \phi_\omega(\kappa) R_\nu(\kappa) d\kappa. \end{aligned} \tag{4.43}$$

Analysis of $z_3[i]$

Since $b_j a_{i,j+1} = a_{i,j} d_i$,

$$z_3[i] = d_i \sum_{j=0}^{N_f-1} \int_0^{T_I} a_{i,j} g(t - D_j) \nu(t + t_{i,j}) dt. \tag{4.44}$$

Let $z_3[i] = d_i \sum_{j=0}^{N_f-1} I_{3j}$ then $V_3 = \sum_{j=0}^{N_f-1} \mathsf{E}(I_{3j}^2)$, where $\mathsf{E}(I_{3j}^2)$ is determined the same way as $\mathsf{E}(I_{2j}^2)$.

$$\mathsf{E}\left(I_{3j}^2\right) = \int_0^{T_I} \int_0^{T_I} E\{g(t - D_j) g(\nu - D_j)\} E\{n(t + t_{i,j}) n(\nu + t_{i,j})\} dt d\nu. \tag{4.45}$$

Using the same arguments as the ones used to derive $\mathsf{E}(I_{2j}^2)$, we have $\mathsf{E}\{g(t-D_j)g(\varrho-D_j)\} = \mathsf{E}\{g(t)g(\varrho)\}$, and finally

$$\begin{aligned} V_3 &= \tfrac{\Pi}{\gamma} \sum_{j=0}^{N_f-1} \left(1 - e^{-\gamma T_I}\right) \int_{-T_\omega}^{T_\omega} \phi_\omega(\kappa) R_\nu(\kappa) d\kappa \\ &= \tfrac{\Pi N_f \left(1-e^{-\gamma T_I}\right)}{\gamma} \int_{-T_\omega}^{T_\omega} \phi_\omega(\kappa) R_\nu(\kappa) d\kappa. \end{aligned} \tag{4.46}$$

Analysis of $z_4[i]$

V_4 is derived as follows:

$$\begin{aligned} V_4 = & \sum_{j=0}^{N_f-1} \int_0^{T_I} \int_0^{T_I} \mathsf{E}\{\nu(t + t_{i,j}) n(\varrho + t_{i,j})\} \mathsf{E}\{\nu(t + t_{i,j} + D_j) \nu(\varrho + t_{i,j} + D_j)\} dt d\varrho \\ = & N_f \int_0^{T_I} \int_{-t}^{T_I - t} R_\nu^2(\kappa) dt d\kappa \\ = & N_f T_I \int_{-T_I}^{T_I} R_\nu^2(\kappa) d\kappa. \end{aligned} \tag{4.47}$$

Bit Error Probability

The conditional bit error probability is expressed as

$$P\{e|z_1\}_{DTR} = Q\left(\sqrt{\frac{z_1^2}{V_2 + V_3 + V_4}}\right) \tag{4.48}$$

where $Q(x) = 1/\sqrt{2\pi}\int_x^\infty e^{-t^2/2}dt$. $P\{e|z_1\}_{DTR}$ is conditioned by the channel realization.

4.4.2 System Modelling Approach

Using the equivalent system and noise models derived in subsections 4.3.2, the conditional BER can also be determined as

$$\begin{aligned} P_z\{e|z_\tau[i]\} &= Q\left(\frac{(z_\tau[i]-h_{\tau 0})d_i}{\sqrt{\mathsf{E}\{z_n^2[i]\}}}\right) \\ &= Q\left(\frac{h_{\tau 1}}{\sqrt{\mathsf{E}\{z_n^2[i]\}}}\right), \end{aligned} \tag{4.49}$$

where $h_{\tau 0}$ is the bias term and $h_{\tau 1}$ is the linear model coefficient.

4.4.3 Derivation of Average BER

The BER of our TR-UWB systems can be obtained by averaging over several conditional BER values. This average BER can be expressed as

$$\bar{P}_{e,TR} = \int_0^\infty P\{e|x\} f_{z_1}(x)dx, \tag{4.50}$$

where $f_{z_1}(\cdot)$ is the probability density function (pdf) of z_1. The derivation of an analytic expression for $\bar{P}_{e,TR}$ by solving the integral in (4.50) is complex. Instead, we propose to determine the average BER $\bar{P}_e$ for low complexity TR-UWB systems, with minimal ISI ($\eta = 1$) or no ISI ($\eta = 0$), using the concept of minimum distance receiver.

Probability Density Function of the Equivalent System Model $z_\tau[i]$

The equivalent system model $z_\tau[i]$ is a random process as it depends on the channel realization and data. It is assumed, in this thesis, that $z_\tau[i]$ is a Gaussian random process. This assumption is justified through simulation as shown in Fig. 4.14, which is obtained after 1000 channel simulation runs, for positive data. The histogram depicts the probability of occurrence of the different values of $z_\tau[i]$, whereas the solid line is obtained by plotting a Gaussian probability density function with mean $\mathsf{E}\{z_\tau[i]\}$ and variance $\mathsf{E}\{z_\tau^2[i]\} - (\mathsf{E}\{z_\tau[i]\})^2$.

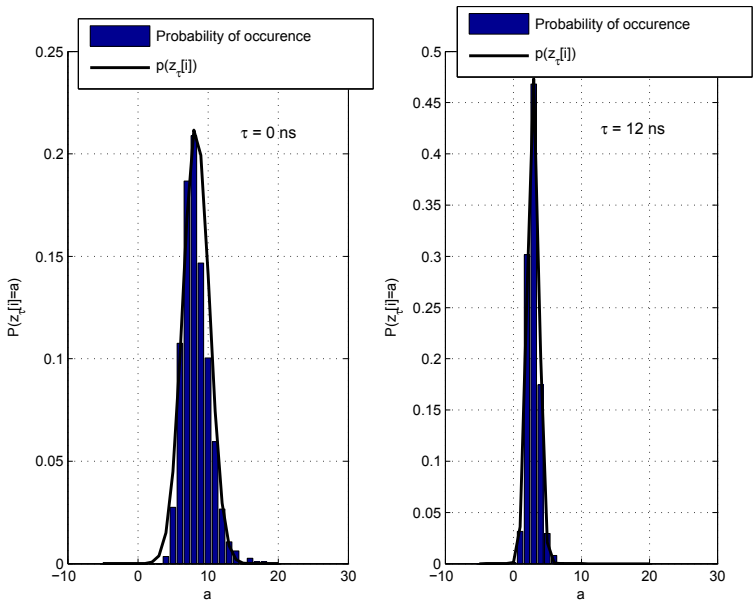

Figure 4.14: Probability density function of $z_\tau[i]$.

Formulation as a Hypothesis Testing Problem

Let us assume a binary detector with the following hypothesis testing problem for detecting $z_\tau[i]$

$$\begin{aligned} H_{-1}: &\quad \hat{z}[i] = s_{-1\tau}[i] + z_{\tau\nu}[i] \\ H_1: &\quad \hat{z}[i] = s_{1\tau}[i] + z_{\tau\nu}[i], \end{aligned} \tag{4.51}$$

where $s_{-1\tau}[i]$ and $s_{1\tau}$ are respectively the equivalent system model for negative and positive data transmitted at time instant i. $s_{-1\tau}[i]$ and $s_{1\tau}$ are expressed as

$$\begin{aligned} s_{1\tau}[i] &= h_{\tau 0} + \mathbf{h}_{\tau 1}^T \mathbf{d}_1[i] + \mathbf{d}_1[i]\mathbf{H}_{\tau 2}\mathbf{d}_1[i] \\ s_{-1\tau}[i] &= h_{\tau 0} + \mathbf{h}_{\tau 1}^T \mathbf{d}_{-1}[i] + \mathbf{d}_{-1}[i]\mathbf{H}_{\tau 2}\mathbf{d}_{-1}[i] \\ \mathbf{d}_1[i] &= [d_{i-\eta}, d_{i-\eta+1}, \ldots, d_{i-1}, 1, d_{i+1}]^T \\ \mathbf{d}_{-1}[i] &= [d_{i-\eta}, d_{i-\eta+1}, \ldots, d_{i-1}, -1, d_{i+1}]^T. \end{aligned} \tag{4.52}$$

Low complexity TR-UWB systems with minimal ISI ($\eta = 1$) are first considered. Since $\forall i$, $d_i \in \{-1, 1\}$, $s_{1\tau}$ and $s_{-1\tau}$ can each have $2^{\eta+1}$ possible values $s_{kj\tau}[i]$, where $k \in \{-1, 1\}$ and $j = 1, 2, \ldots, 2^{\eta+1}$. Thus, at the symbol rate, one of the $2^{\eta+2}$ variables $s_{kj\tau}[i]$ is transmitted. This is a classical signal classification problem, which motivates the use of a minimum distance receiver.

Since $z_\tau[i]$ is a Gaussian random process, the $s_{kj\tau}[i]$ are also Gaussian. Moreover they are independent of each other. At time i let we decide H_{kj} for which $D_{kj}^2 = (\hat{z}[i] - s_{kj\tau}[i])^2$ is minimum.

Because $\hat{z}^2[i]$ is the same $\forall(i, j)$, we decide H_{jk} for which $T_{kj}(\hat{z}[i]) = -2\hat{z}[i]s_{kj\tau}[i] + s_{kj}^2[i]$ is minimum, i.e., $T_{kj}(\hat{z}[i]) = \hat{z}[i]s_{kj\tau}[i] - \frac{1}{2}s_{kj\tau}^2[i]$ is maximum. Since H_k is decided when

one of the H_{kj} is decided, and H_{kj} are independent elements of H_k,

$$p(\hat{z}[i]|H_k) = \sum_{j=1}^{2^{\eta+1}} p(\hat{z}[i]|H_{kj}). \tag{4.53}$$

This motivates us to decide H_k for which

$$T_k(\hat{z}[i]) = \sum_{j=1}^{2^{\eta+1}} (\hat{z}[i]s_{kj\tau}[i] - \frac{1}{2}s^2_{kj\tau}[i]) \tag{4.54}$$

is maximum. Thus, H_1 is decided if $T_1(\hat{z}[i]) > T_{-1}(\hat{z}[i])$.
Let $T(\hat{z}[i]) = T_1(\hat{z}[i]) - T_{-1}(\hat{z}[i])$,

$$T(\hat{z}[i]) = \sum_{j=1}^{2^{\eta+1}} \big(\hat{z}[i](s_{1j\tau}[i] - s_{-1j\tau}[i]) - \frac{1}{2}(s^2_{1j\tau}[i] - s^2_{-1j\tau}[i])\big). \tag{4.55}$$

Following the condition that $T(\hat{z}[i]) > 0$, we have

$$\begin{aligned} T'(\hat{z}[i]) &= \sum_{j=1}^{2^{\eta+1}} \hat{z}[i](s_{1j\tau}[i] - s_{-1j\tau}[i]) \\ &> -\tfrac{1}{2}\sum_{j=1}^{2^{\eta+1}} (s^2_{1j\tau}[i] - s^2_{-1j\tau}[i]) = \gamma_\tau. \end{aligned} \tag{4.56}$$

Equation (4.56) shows that the assumed detector consists of a test statistics $T'(\hat{z}[i])$ and a threshold γ_τ.

For the case of ISI-free TR-UWB systems, we have

$$\begin{aligned} s_{1\tau}[i] &= h_{\tau 0} + h^T_{\tau 1} \\ s_{-1\tau}[i] &= h_{\tau 0} - h^T_{\tau 1}. \end{aligned} \tag{4.57}$$

H_1 is decided if

$$\begin{aligned} T_h(\hat{z}[i]) &= \hat{z}[i](s_{1\tau}[i] - s_{-1\tau}[i]) \\ &> -\tfrac{1}{2}(s^2_{1\tau}[i] - s^2_{-1\tau}[i]) = \zeta_\tau. \end{aligned} \tag{4.58}$$

After simplification we obtain

$$\begin{aligned} T_h(\hat{z}[i]) &= \hat{z}[i] \\ \zeta_\tau &= h_{\tau 0}. \end{aligned} \tag{4.59}$$

Analysis of the Test Statistics

$T'(\hat{z}[i])$ and $T_h(\hat{z}[i])$ are Gaussian random variables conditioned on either hypothesis. We already considered $z_{\tau\nu}$ in subsection 4.3.1 to be zero-mean Gaussian. Using this approxi-

mation we express analytically the moments of $T'(\hat{z}[i])$ and $T_h(\hat{z}[i])$.

$$\begin{aligned} \mathsf{E}\{T'|H_{-1}\} &= \mathsf{E}\{\sum_{j=1}^{2^{\eta+1}} (s_{-1j\tau}[i] + z_{\tau\nu}[i])(s_{1j\tau}[i] - s_{-1j\tau}[i])\} \\ &= \mathsf{E}\{\sum_{j=1}^{2^{\eta+1}} s_{-1j\tau}[i](s_{1j\tau}[i] - s_{-1j\tau}[i])\} \\ &\quad + \mathsf{E}\{\sum_{j=1}^{2^{\eta+1}} z_{\tau\nu}[i](s_{1j\tau}[i] - s_{-1j\tau}[i])\} \\ &= \mathsf{E}\{\mathbf{s}_{-1\tau}(\mathbf{s}_{1\tau} - \mathbf{s}_{-1\tau})^T\} = \varepsilon_{-1\tau}, \end{aligned} \tag{4.60}$$

where $\mathbf{s}_{k\tau} = [s_{k1\tau}[i], s_{k2\tau}[i], \ldots, s_{kN\tau}[i]]$ and $N = 2^{\eta+1}$.

$$\mathsf{E}\{T_h|H_{-1}\} = \mathsf{E}\{s_{-1\tau}\}. \tag{4.61}$$

$$\begin{aligned} \mathrm{var}(T'|H_{-1}) &= \mathrm{var}(\mathbf{s}_{-1\tau}(\mathbf{s}_{1\tau} - \mathbf{s}_{-1\tau})^T) + \mathrm{var}(z_{\tau\nu}[i] \sum_{j=1}^{2^{\eta+1}} (\mathrm{s}_{1j\tau}[i] - \mathrm{s}_{-1j\tau}[i])) \\ &= \sigma^2_{-1\tau} + \sigma^2_{\tau s\nu}, \end{aligned} \tag{4.62}$$

where

$$\sigma^2_{\tau s\nu} = \mathsf{E}\{(\sum_{j=1}^{2^{\eta+1}} (\mathrm{s}_{1j\tau}[i] - \mathrm{s}_{-1j\tau}[i]))^2\} \times \mathsf{E}\{z^2_{\tau\nu}\}. \tag{4.63}$$

$$\mathrm{var}(T_h|H_{-1}) = \mathrm{var}(z_\tau) + \mathsf{E}\{z^2_{\tau\nu}\} = \sigma^2_\tau + \sigma^2_{\tau\nu}. \tag{4.64}$$

Following the same steps as above, we derive

$$\mathsf{E}\{T'|H_1\} = \mathsf{E}\left\{\mathbf{s}_{1\tau}(\mathbf{s}_{1\tau} - \mathbf{s}_{-1\tau})^T\right\} = \varepsilon_{1\tau}. \tag{4.65}$$

$$\mathsf{E}\{T_h|H_1\} = \mathsf{E}\{s_{1\tau}\}. \tag{4.66}$$

$$\mathrm{var}(T'|H_1) = \sigma^2_{1\tau} + \sigma^2_{\tau s\nu}, \tag{4.67}$$

where $\sigma^2_{1\tau} = \mathrm{var}(\mathbf{s}_{1\tau}(\mathbf{s}_{1\tau} - \mathbf{s}_{-1\tau})^T)$.

$$\mathrm{var}(T_h|H_1) = \sigma^2_\tau + \sigma^2_{\tau\nu}. \tag{4.68}$$

Bit Error Probability

The probability of error $\bar{P}_e$ is defined as

$$\bar{P}_e = P(H_{-1}|H_1)P(H_1) + P(H_1|H_{-1})P(H_{-1}), \tag{4.69}$$

where $P(H_1|H_{-1})$ is the conditional probability of deciding H_1 given that H_{-1} is true. Assuming that the prior probabilities are equal, i.e., $P(H_1) = P(H_{-1}) = \frac{1}{2}$ we have

$$\begin{aligned} \bar{P}_e &= \tfrac{1}{2}[P(H_{-1}|H_1) + P(H_1|H_{-1})] \\ &= \tfrac{1}{2}[P_r(T'(\hat{z}[i]) < \gamma_\tau|H_1) + P_r(T'(\hat{z}[i]) > \gamma_\tau|H_{-1})] \end{aligned} \tag{4.70}$$

$$\begin{aligned} \bar{P}_e &= \tfrac{1}{2}[1 - Q(\tfrac{\gamma_\tau - \varepsilon_{1\tau}}{\sqrt{\sigma^2_{1\tau}+\sigma^2_{\tau s\nu}}}) + Q(\tfrac{\gamma_\tau - \varepsilon_{-1\tau}}{\sqrt{\sigma^2_{-1\tau}+\sigma^2_{\tau s\nu}}})] \\ &= \tfrac{1}{2}[Q(\tfrac{\varepsilon_{1\tau} - \gamma_\tau}{\sqrt{\sigma^2_{1\tau}+\sigma^2_{\tau s\nu}}}) + Q(\tfrac{\gamma_\tau - \varepsilon_{-1\tau}}{\sqrt{\sigma^2_{-1\tau}+\sigma^2_{\tau s\nu}}})], \end{aligned} \tag{4.71}$$

where $Q(x) = 1/\sqrt{2\pi}\int_x^\infty e^{-t^2/2}dt$ and $Q(-x) = 1 - Q(x)$. Since $\sigma^2_{1\tau} \approx \sigma^2_{-1\tau}$, P_e can be expressed as

$$\bar{P}_e = \frac{1}{2}\left[Q\left(\frac{\varepsilon_{1\tau} - \varepsilon_{-1\tau}}{\sqrt{\sigma^2_{k\tau} + \sigma^2_{\tau s\nu}}}\right)\right]. \tag{4.72}$$

For the non-ISI case, we obtain

$$\bar{P}_e = \frac{1}{2}[P_r(T_h(\hat{z}[i]) < \zeta_\tau|H_1) + P_r(T_h(\hat{z}[i]) > \zeta_\tau|H_{-1})], \tag{4.73}$$

and finally

$$\begin{aligned} \bar{P}_e &= \tfrac{1}{2}\left[Q\left(\tfrac{E\{s_{1\tau} - s_{-1\tau}\}}{\sqrt{\sigma^2_\tau+\sigma^2_{\tau\nu}}}\right)\right] \\ &= \tfrac{1}{2}\left[Q\left(\tfrac{2E\{h_{\tau 1}\}}{\sqrt{\sigma^2_\tau+\sigma^2_{\tau\nu}}}\right)\right]. \end{aligned} \tag{4.74}$$

4.4.4 Simulation Results

The channel model is the same as in subsection 4.3.1. The different TR-UWB systems considered are shown in Table 4.2 with their simulation parameters.

The bit error performance of the different considered TR-UWB systems, in the presence and absence of timing delay, is demonstrated in Fig. 4.15-Fig. 4.18. The BER curves are presented as functions of SNR and delay ($\tau = \{0$ ns,20 ns$\}$). The solid lines denote the simulated average BER obtained using Monte Carlo simulation, the dash-dot lines denote the average BER obtained from (4.72) or (4.74), and the dotted line in Fig. 4.15 denotes the average BER computed numerically by averaging $P\{e|z_1\}$ in (4.48). There is a perfect matching between both BER curves at $\tau = 0$ ns, and good agreement at higher delay values for the ISI-free DTR-UWB system ($\eta = 0$)).

Next, the bit error performance of DTR-UWB system with minimal ISI is illustrated in Fig. 4.16, in the presence and absence of timing delay ($\tau = 20$ ns and $\tau = 0$ ns, respectively). It can be observed, for both values of τ, that the solid lines (denoting the simulated average

TR-UWB systems ⇒ Parameters ⇓	**DTR UWB** $\eta = 1/\eta = 0$	**LDC DTR-UWB**	**DP TR-UWB**
T_ω [ns]	0.7	0.7	0.7
τ_m [ns]	0.2877	0.2877	0.2877
T_{samp} [ns]	0.05	0.05	0.05
T_f [ns]	10/100	2	20
T_I [ns]	20	20	20
T_s [ns]	100/1000	100	200
N_f	10	9	2
N_{cr}	10	8	1
Data rates [Mb/s]	10/1	10	5

Table 4.2: TR-UWB systems and simulation parameters.

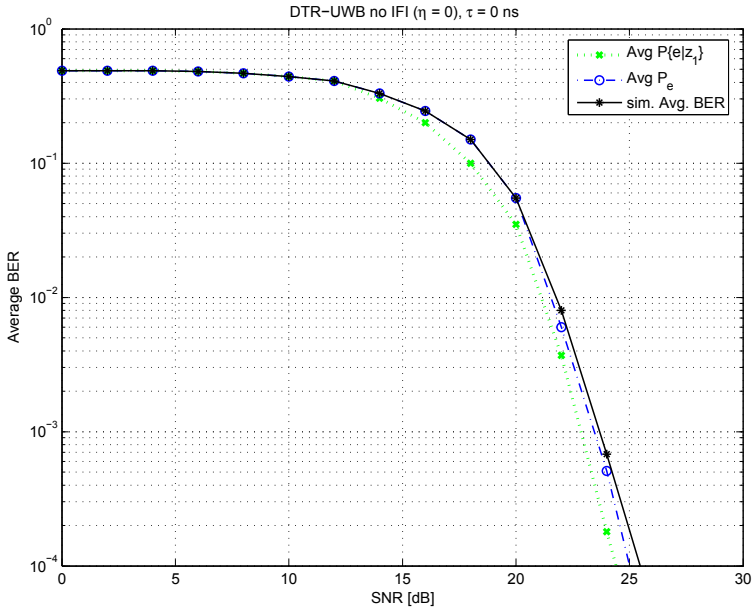

Figure 4.15: BER performance of the DTR-UWB system (η =0) versus SNR.

BER obtained using Monte Carlo simulation) and the dash-dot lines (denoting the average BER obtained from (4.72)) are in good agreement.

Finally, the ISI-free systems LDC DTR-UWB and DP TR-UWB are considered. Fig. 4.17 and Fig. 4.18 show the bit error performance of both systems, in the presence and absence of timing delay. It can again be observed, for both values of τ, that the solid lines (denoting the simulated average BER obtained using Monte Carlo simulation) and the dash-dot lines (denoting the average BER obtained from (4.74)) are in good agreement.

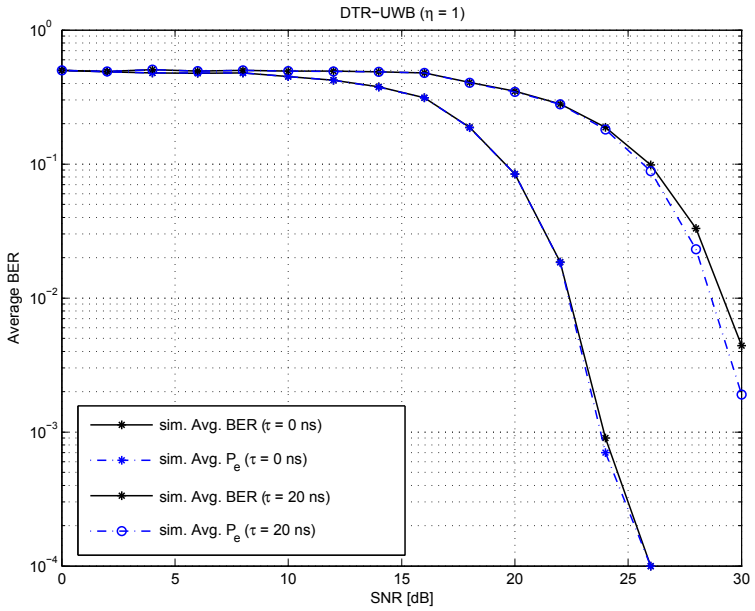

Figure 4.16: BER performance of the DTR-UWB system (η =1) versus SNR.

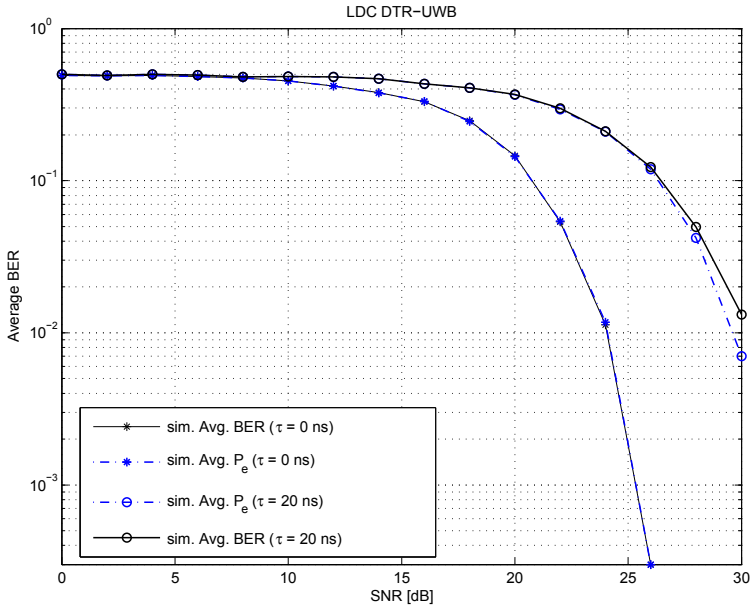

Figure 4.17: BER performance of the LDC DTR-UWB system versus SNR.

4.5 Optimization of the Integration Time Interval T_I

From (4.36) it is clear that by increasing T_I more energy is collected. Simultaneously, more noise is also collected as the sum of the noise variances $V_2 + V_3 + V_4$ is increased.

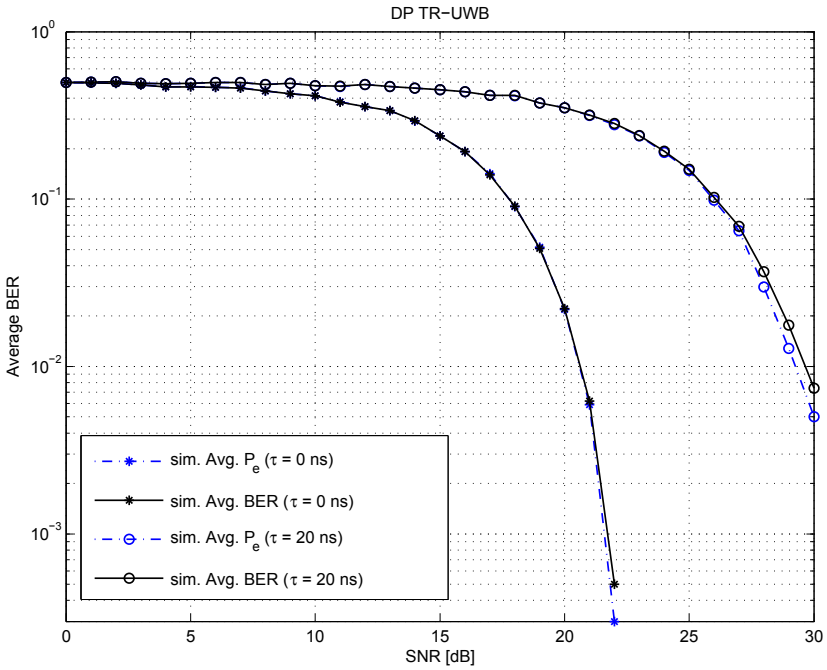

Figure 4.18: BER performance of the DP TR-UWB system versus SNR.

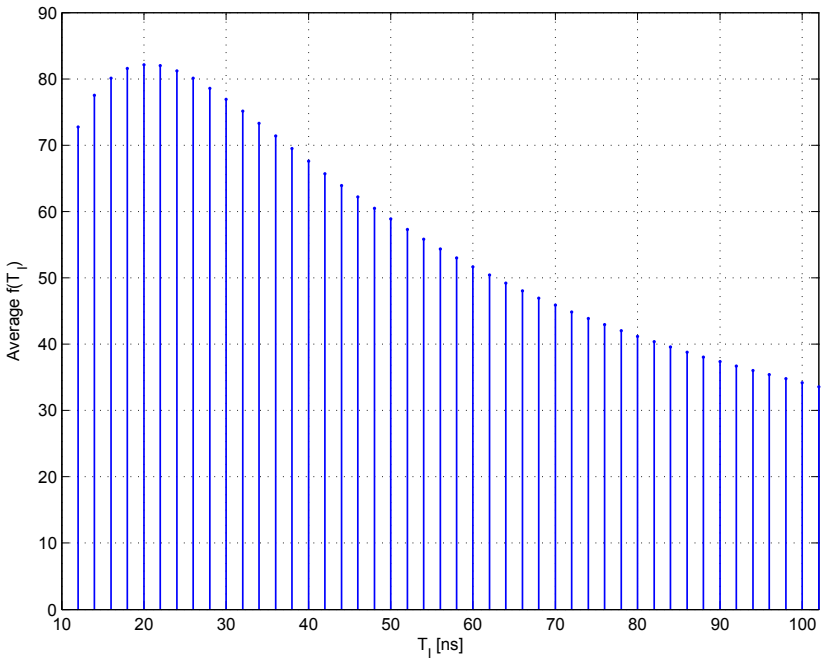

Figure 4.19: Optimal choice for T_I.

Equation (4.48) can be rewritten as

$$\begin{aligned} P\{e|z_1\}_{DTR} &= Q\left(\sqrt{\frac{\left(N_f \int_0^{T_I} g^2(t)dt\right)^2}{\frac{2\Pi N_f\left(1-e^{-\gamma T_I}\right)}{\gamma}\int_{-T_\omega}^{T_\omega}\phi_\omega(\kappa)R_n(\kappa)d\kappa + N_f T_I \int_{-T_I}^{T_I} R_n^2(\kappa)d\kappa}}\right) \\ &= Q\left(\sqrt{f(T_I)}\right). \end{aligned} \tag{4.75}$$

The optimal choice of T_I for optimal BER can be found by optimizing the function $T_I \mapsto f(T_I)$, which is out of scope of this thesis. Instead, the optimal choice for T_I is made graphically by plotting $f(T_I)$ versus T_I, as shown in Fig. 4.19, where the function $T_I \mapsto f(T_I)$ is averaged over 1000 channel realizations. This motivates the choice for $T_I = 20$ ns in all the simulations.

4.6 Summary

Signal and systems models for different TR-UWB systems were presented in this chapter. The different TR-UWB transmission schemes were introduced, followed by the presentation of the receiver front-end. Delay-dependent discrete time equivalent system and noise models for different TR-UWB systems were also reviewed in this chapter for TR-UWB systems with and without ISI. Further, the different receiver statistics are analyzed from two perspectives:

- Use of Gaussian approximation on the noise terms in the receiver statistics.
- Use of the equivalent system models of the receiver.

Both perspectives allow for BER performance analysis to be performed. The average BER is verified through simulation for different SNR values. It is also compared to the average BER derived using the equivalent system models. The derivation of an analytic expression for the average BER was provided using the concept of minimum distance receiver. Finally, the optimization of the integration time interval T_I was dealt with.

Chapter 5

Synchronization of Transmitted Reference Systems

5.1 Introduction

The large bandwidth of UWB technology besides providing the possibility to transmit at a very high data rate also provides very accurate temporal and spatial information that can be used for precise timing offset estimation. This high accuracy also allows new perspectives in terms of synchronization, positioning and tracking [9, 58].

Synchronization is a particulary acute problem faced by UWB systems due to the fact that they employ low-power ultra-short (sub-nanoseconds) pulses. Thus, timing requirements are stringent because minor misalignments may result in a lack of energy capture which renders symbol detection impossible [59]. Synchronization is typically performed in two stages: the first stage achieves *coarse synchronization* to within a reasonable amount of accuracy, and the second stage is responsible for achieving *fine synchronization* (timing offset estimation). Synchronization schemes for UWB systems in the literature can be roughly classified into *detection-based* schemes [60] - [65] and *estimation-based* schemes [66] - [70].

The synchronization methods which employ a detection-based approach evaluate a candidate delay by first obtaining a measure of correlation between the received signal and a locally generated template signal offset by the candidate delay. This measure of correlation is then compared to a threshold in order to make a decision. The candidates could be evaluated in a serial, parallel or hybrid manner. For threshold based synchronization schemes in multipath fading channels, it was shown in [64] that, no matter how large the SNR is or how the threshold is chosen, it may not be possible to make the probabilities of detection and false alarm arbitrarily large and small. Moreover, the large search space in UWB signal acquisition poses significant challenges in the design and implementation of practical systems for high data rate applications.

In the estimation-based methods, an estimate of the delay is obtained through maximizing a statistic over a set of candidate delays. This statistic is usually obtained from the correlation of the received signal with a template. These schemes do not involve a threshold comparison. They rather exploit the cyclostationarity inherent in UWB signaling due to pulse repetition. Most of these schemes are based on the Nyquist or higher sampling

rate of the signal and may not be feasible for low cost UWB devices. To avoid the high sampling rate and computational complexity associated with channel estimation and time synchronization, there has been a renewed interest in the TR systems for impulse radio due to their simple receiver structure.

In this thesis, a novel data-aided timing acquisition technique for frame-level synchronization of DTR-UWB systems is suggested [71]. It is based on incorporating parallel I&D circuits within pulse-pair correlator branches to improve considerably the energy capture in the presence of timing offset. Since this technique performs perfectly well when the noise variance is much less than the signal energy, symbol-long segments of the received signal are averaged before timing acquisition. A training sequence is chosen to ensure that pulse polarities within consecutive symbol-long segments of the received signal do not get cancelled through the averaging operation. The good performance of the proposed timing acquisition technique is confirmed through simulation results.

Furthermore, a simple timing offset estimator for low complexity TR-UWB systems, assuming no ISI, is considered. Both the classical and bayesian approaches are used for estimating the timing offset. It is shown, in this chapter, that both approaches yield the same timing offset estimate. The proposed algorithm uses energy collected at the symbol rate, thus reducing considerably the implementation complexity. If coarse synchronization is achieved (e.g. [71]) and hardware clock timing error is known, timing offset estimation problems are analogical to ranging problems, and the proposed algorithm can readily be used for distance measurement. The theoretical performance limit of such a timing offset estimation is illustrated through the derived Cramér-Rao Lower Bound (CRLB) for the variance of the timing offset estimates.

5.2 Data-Aided Timing Acquisition

The DTR-UWB receiver illustrated in Fig. 4.4 has at its input a bank of pulse-pair correlators, whose lags are matched to the time shifts D_j. The I&D blocks are triggered at the arrival-times of the respective pulses, which requires time-synchronization and knowledge of the TH-sequence.

5.2.1 Timing Acquisition Technique

In this section, we perform a parallel search of the timing offset by incorporating parallel I&D circuits within pulse-pair correlator branches and using the outputs of these I&D blocks to determine the frame index that matches the timing offset. It is worth noting that, in practice, the data obtained at the output of the I&D circuits are actually acquired serially since the parallel I&D circuits within each pulse-pair correlator branch are actually fractional parts of a single I&D circuit (*fractional sampling*). The parallel structure shown in Fig. 5.1 is used to help understand our timing acquisition technique. This novel timing acquisition technique relies on judiciously choosing the different triggering times of the I&D circuits and the time interval T_I over which the integration operations are performed, as shown in Fig. 5.1. Each pulse-pair correlator branch with correlator lag D_j is associated with N_f parallel I&D blocks which are triggered at different times than the respective

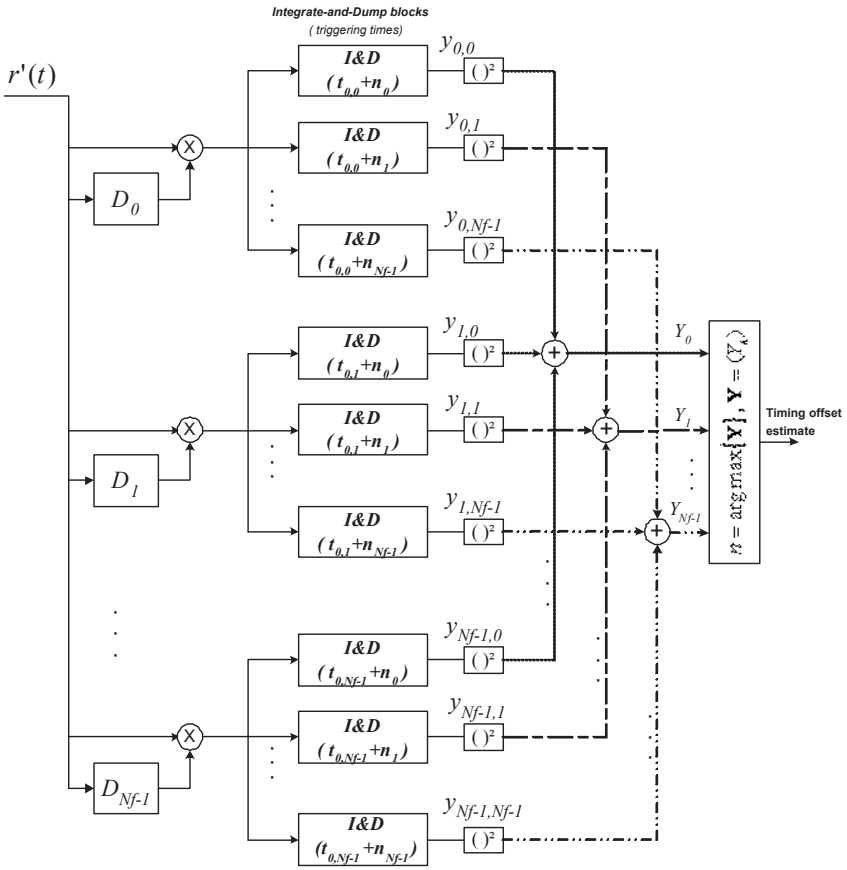

Figure 5.1: Illustration of the timing acquisition technique

pulses arrival times. Without loss of generality, the synchronization to symbol $i = 0$ is considered. Thus, the different pulse arrival times are given by

$$t'_{j,k} = t_{0,j} + n_k, \tag{5.1}$$

where $n_k = kT_f$ for $k \in \{0, 1, ..., N_{f-1}\}$.

Our timing acquisition technique, through the parallel I&D operations, aims to achieve efficient multipath energy collection even in presence of timing offset and noise. The accuracy of timing acquisition is enhanced by reducing the noise level, i.e., by averaging over different symbol-long segments of the received signal $r(t)$. The shortcomings of such averaging stem from the fact that the differentially modulated pulse polarities (± 1) are different from one symbol to another. Thus, averaging could result on the cancellation of some pulses within a symbol waveform and therefore altering the energy collection within some frames. This is the reason why we use a training sequence, given by $d'_p = (-1)^p$, where $p \in \{0, 1, ..., P-1\}$ and P is the length of the training sequence. This sequence ensures that pulse polarities within the $P/2$ first odd numbered symbol-long segments of $r(t)$ are identical, as well as pulse polarities within the $P/2$ first even numbered symbol-

long segments of $r(t)$. Thus, consecutive segments of $r(t)$ of duration $2T_s$ are summed together before we apply our timing acquisition technique.

Indeed, let us assume the m^{th} segment of the received signal $r(t)$ of duration $2T_s$ is $r_m(t) = r\big(t + 2(m-1)T_s\big)$ for $t \in [0, 2T_s)$, and $r_m(t) = 0$ elsewhere. Then the waveform used for timing acquisition is

$$r'(t) = \frac{2}{P} \sum_{m=1}^{P/2} r_m(t). \tag{5.2}$$

The outputs of the $N_f \times N_f$ I&D blocks are given by

$$y_{j,k} = \int_{t_{0,j}+n_k}^{t_{0,j}+n_k+T_I} r'(t + D_j) r'(t) dt. \tag{5.3}$$

Let $Y_k = \sum_{j=0}^{N_f-1} y_{j,k}^2$. Fig. 5.2 shows the magnitude of the Y_k for different timing offsets.

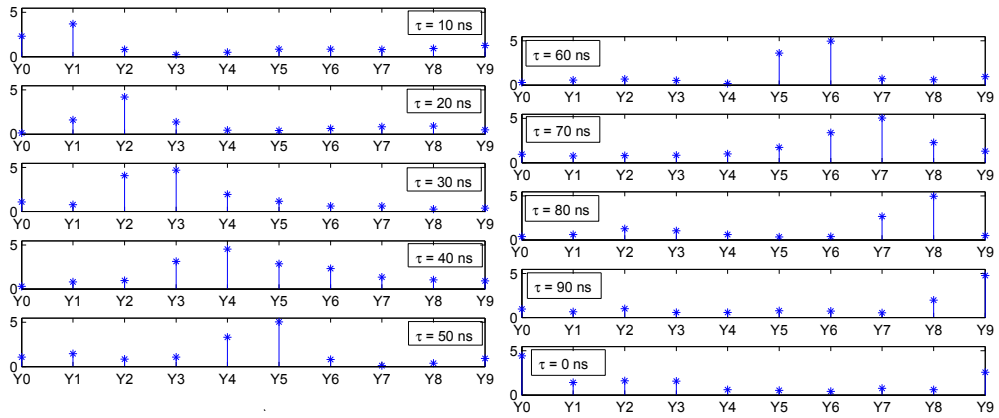

Figure 5.2: Illustration of the outputs Y_k for different timing offsets

The first step towards estimating the timing offset is achieved by finding the index n given by:

$$n = \arg\max_k \{Y_k\}. \tag{5.4}$$

Finally, the coarse estimate of τ is given as

$$\tilde{\tau} = nT_f, \tag{5.5}$$

where $n \in \{0, 1, \ldots, N_{f-1}\}$.

5.2.2 Simulation Results

In this subsection, the simulation results are presented. The timing acquisition performance is discussed by using the following performance metrics: the normalized acquisition esti-

mation mean square error (MSE) given by $E\left\{(\tilde{\tau}-\tau)^2\right\}/T_s^2$, the probability of detecting correctly the timing offset P_{CD} and the average bit-error-rate (BER).

Fig. 5.3 depicts the MSE of our timing acquisition technique plotted versus SNR for values of $M = P/2 = 16, 32, 64, 128$. As M increases, the normalized MSE decreases monotonically. The same trend can be observed for increasing SNR. For all the M values, the MSE curves flatten at high SNR towards a certain error floor. This is due to the frame resolution limit imposed by the coarse estimation. This frame resolution limit can be removed through tracking.

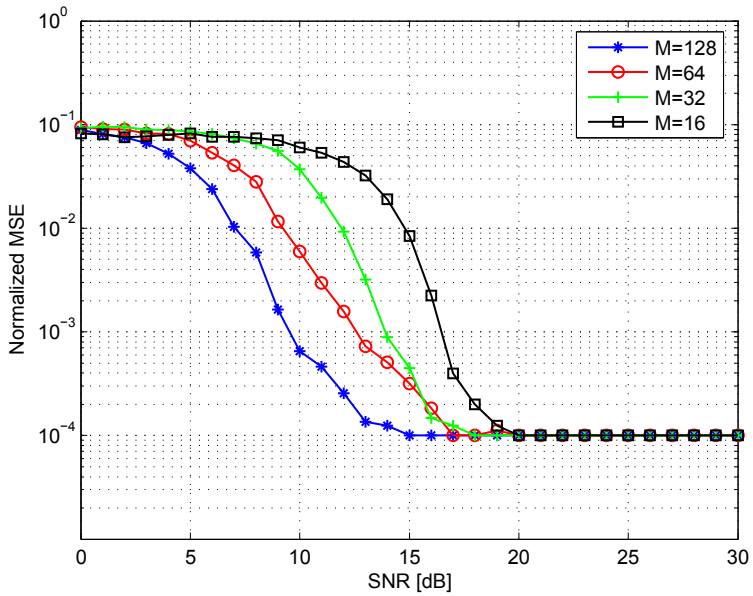

Figure 5.3: Normalized timing acquisition MSE vs. SNR for $M = \{16, 32, 64, 128\}$.

This error floor is illustrated in Fig. 5.4 for different timing offsets $\tau = \{41$ ns, 42 ns, 45 ns, 48 ns, 49 ns$\}$ where the expected estimated timing offsets are given respectively as $\tilde{\tau} = \{40$ ns, 40 ns, 40 ns, 50 ns, 50 ns$\}$.

From the frame resolution limit it is clear that the best performance of our timing acquisition technique is achieved when the timing offset to be estimated is an integer multiple of the frame duration. Thus, we have tested the performance of our timing acquisition technique in terms of its probability of detecting correctly the timing offset P_{CD}, when the timing offset is an integer multiple of the frame duration. This is shown in Fig. 5.5 for values of $M = 16, 32, 64, 128$. It can be observed that the P_{CD} increases monotonically as M increases. The same trend is observed for increasing SNR. With $M = 128$, we achieve $P_{CD} = 1$ from SNR = 10 dB.

Finally, the BER performance of our timing acquisition technique is tested for values of $M = 16, 128$. This BER performance is compared to the cases without timing acquisition, and with perfect timing. It can be observed from Fig. 5.6 that, as M increases, the BER performance improves monotonically. It is also observed that there is no significant performance loss when we compare the BER performance of our timing acquisition technique to

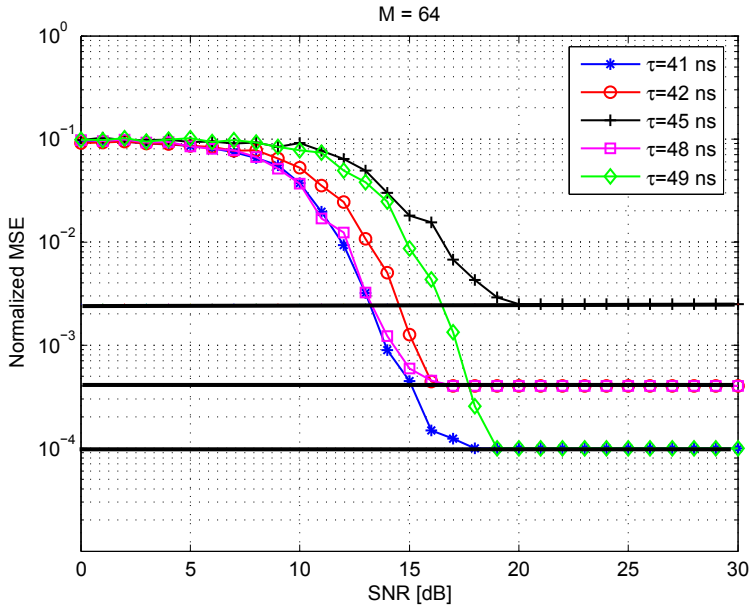

Figure 5.4: Normalized timing acquisition MSE vs. SNR for $\tau = \{41$ ns, 42 ns, 45 ns, 48 ns, 49 ns$\}$.

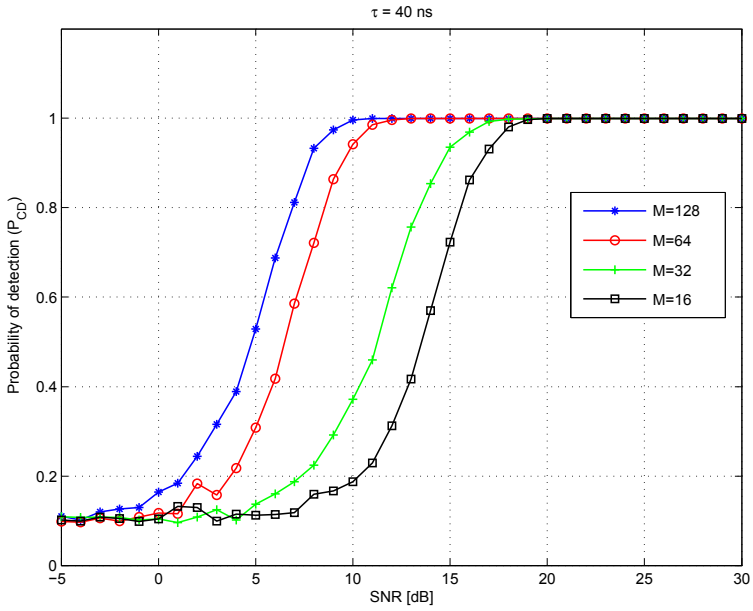

Figure 5.5: Probability of detection vs. SNR for $M = \{16, 32, 64, 128\}$.

the case where there is perfect timing. Indeed, the performance loss is less than 1 dB for $M = 128$ and around 1.2 dB when $M = 16$. This is due to a combination of the robustness

of the DTR-UWB systems against timing offset and the good performance of our timing acquisition technique.

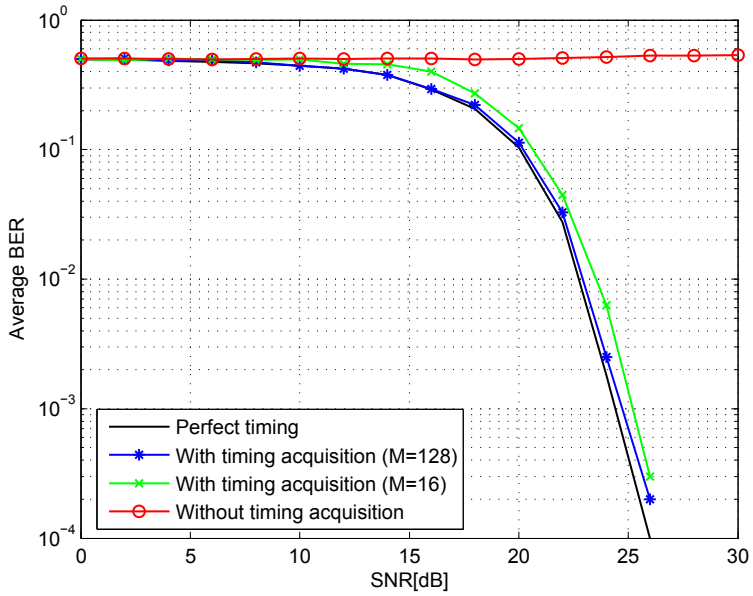

Figure 5.6: Average BER vs. SNR for $M = \{16, 168\}$.

5.3 Timing Offset Estimation

The received signal with time delay τ, expressed in (4.5), will start within a window of duration T_d that represent the uncertainty on the arrival time of the received signal. This time window is allocated in the time line by a previous coarse acquisition process, presented in the previous section. In this section, two approaches to timing offset estimation are presented, using the statistical analysis of the delay-dependent equivalent system and noise models presented in section 4.3 for low complexity TR-UWB systems, and the analysis in subsection 4.4.3.

5.3.1 Normalization of the decision variable

Let $z_s[i] = \hat{z}[i]/E_s$ be the normalized decision variable. This normalization is necessary to minimize the channel dependence of the decision variable. We obtain

$$z_s[i] = z_{e\tau}[i] + z_{e\tau\nu}[i]. \tag{5.6}$$

where $z_{e\tau}[i] = z_\tau[i]/E_s$ and $z_{e\tau\nu}[i] = z_{\tau\nu}[i]/E_s$. At a time instant i, $z_{e\tau}[i]$ is a Gaussian random variable with mean $\mathsf{E}\{z_{e\tau}[i]\}$ and variance σ^2_{ze}. The data-dependence of $z_{e\tau}[i]$ impose a prior knowledge of the data sequence for efficient characterization of $z_{e\tau}$. This implies the

need of a training sequence in order to obtain an efficient timing offset estimation. When fitted with an exponential function, $\mathsf{E}\{z_{e\tau}\}$ can be expressed as

$$\begin{array}{rcll} \mathsf{E}\{z_{e\tau}\} & = & A_1 \exp(B\tau), & d_i = 1 \\ \mathsf{E}\{z_{e\tau}\} & = & A_2 \exp(B\tau), & d_i = -1. \end{array} \tag{5.7}$$

Generally, A_2 is slightly different from $-A_1$, due to the bias term $h_{\tau 0}$. Hence a time instant i the realizations of $z_{e\tau}[i]|d_i$ are asymmetric. Nevertheless, for most of the systems considered in this work, $h_{\tau 0} \approx 0$, since the interference among fixed reference pulses plus interference between equally modulated data pulses is reduced by allowing larger average pulse separations. Hence, we can write

$$\mathsf{E}\{z_{e\tau}[i]\} = Ad_i \exp(B\tau). \tag{5.8}$$

B takes approximately the same value for all TR-UWB systems considered in this work. The value of A is proportional to the ratio N_{cr}/N_f.

5.3.2 Classical Approach to Timing Offset Estimation

Let us consider $z_{e\tau}$ to be a deterministic but unknown function of τ. We assume that the normalized output energy of the TR-UWB systems, collected at the symbol rate, is composed of the equivalent system model $z_{e\tau}$ with zero mean gaussian modelling uncertainty plus system noise $z_{e\tau\nu}$. The variance of the modelling error is given by σ_{ze}^2 and $\mathrm{var}(z_{e\tau\nu}) = \sigma_{\nu e}^2$. In [15] it is indicated that the noise $z_{\tau\nu}$ can be considered as a zero-mean Gaussian process. Thus, we have

$$p(z_s;\tau) = \frac{1}{[2\pi(\sigma_{ze}^2 + \sigma_{\nu e}^2)]^{P/2}} \exp\left[-\frac{1}{2(\sigma_{ze}^2 + \sigma_{\nu e}^2)} \sum_{i=0}^{P-1} (z_s[i] - Ad_i \exp(B\tau))^2 \right], \tag{5.9}$$

where P indicate the number of data symbols in the training sequence with the same polarity. Taking the logarithm of (5.9) and finding its derivative w.r.t τ, we obtain

$$\frac{\partial \ln p(z;\tau)}{\partial \tau} = \frac{ABd_i \exp(B\tau) \left(\sum_{i=0}^{P-1} z_s[i] - PAd_i \exp(B\tau) \right)}{(\sigma_{ze}^2 + \sigma_{\nu e}^2)}. \tag{5.10}$$

Solving $\frac{\partial \ln p(z;\tau)}{\partial \tau} = 0$ for τ, we obtain the maximum likelihood (ML) estimate of the timing offset as

$$\begin{array}{rcl} \hat{\tau} & = & \frac{1}{B} \ln \left(\sum_{i=0}^{P-1} z_s[i] \Big/ (PAd_i) \right) \\ & = & \frac{1}{B} \ln \left(\frac{|\bar{z}_s|}{A} \right), \end{array} \tag{5.11}$$

where $\bar{z}_s = (1/P)\sum_{i=0}^{P-1} z_s[i]$, and $|\bar{z}_s| = \bar{z}_s/d_i = z_s d_i$.
The Cramér-Rao Lower Bound (CRLB) for the variance of the timing offset estimates is derived by finding the derivative of (5.10) w.r.t τ [72].

$$\frac{\partial^2 \ln p(z;\tau)}{\partial \tau^2} = \frac{PAB^2 \exp(B\tau)\left[|\bar{z}_s| - 2A\exp(B\tau)\right]}{(\sigma_{ze}^2 + \sigma_{\nu e}^2)}. \tag{5.12}$$

Finally, $CRLB(\hat{\tau}) = -\mathsf{E}\left\{\frac{\partial^2 \ln p(z;\tau)}{\partial \tau^2}\right\}$ is expressed as

$$CRLB(\hat{\tau}) = \frac{(\sigma_{ze}^2 + \sigma_{\nu e}^2)}{PAB^2 \exp(B\tau)\left[2A\exp(B\tau) - |\bar{z}_s|\right]}. \tag{5.13}$$

5.3.3 Bayesian Approach to Timing Offset Estimation

$z_{e\tau}[i]$ is now considered to be a stochastic process with pdf

$$p(z_{e\tau}[i]) = \frac{1}{\sqrt{2\pi\sigma_{ze}^2}} \exp\left[-\frac{1}{2\sigma_{ze}^2}(z_{e\tau} - Ad_i \exp(B\tau))^2\right]. \tag{5.14}$$

The pdf of $\mathbf{z}_s$ conditioned on $z_{e\tau}$ is given by

$$p(\mathbf{z}_s|z_{e\tau}) = \frac{1}{(2\pi\sigma_{\nu e}^2)^{P/2}} \exp\left[-\frac{1}{2\sigma_{\nu e}^2}\sum_{i=0}^{P-1}(z_s[i] - z_{e\tau})^2\right]. \tag{5.15}$$

In the Appendix III, we have proven that $z_{e\tau}|\mathbf{z}_s$ is a Gaussian random variable with variance

$$\sigma_{z_{e\tau}|z_s}^2 = \frac{1}{P/\sigma_{\nu e}^2 + 1/\sigma_{ze}^2}, \tag{5.16}$$

and mean

$$m_{z_{e\tau}|z_s} = \left(\frac{P\bar{z}_s}{\sigma_{\nu e}^2} + \frac{Ad_i \exp(B\tau)}{\sigma_{ze}^2}\right)\left(\frac{P}{\sigma_{\nu e}^2} + \frac{1}{\sigma_{ze}^2}\right)^{-1}. \tag{5.17}$$

Equation (5.17) can be written as

$$m_{z_{e\tau}|z_s} = \alpha + \beta \exp(B\tau), \tag{5.18}$$

where

$$\begin{aligned} \alpha &= \left(\tfrac{P\bar{z}_s}{\sigma_{\nu e}^2}\right)\left(\tfrac{P}{\sigma_{\nu e}^2} + \tfrac{1}{\sigma_{ze}^2}\right)^{-1} \\ \beta &= \left(\tfrac{Ad_i}{\sigma_{ze}^2}\right)\left(\tfrac{P}{\sigma_{\nu e}^2} + \tfrac{1}{\sigma_{ze}^2}\right)^{-1}. \end{aligned} \tag{5.19}$$

The timing offset estimate $\hat{\tau}$ is derived from (5.18) through functional mapping, by minimizing the least square (LS) error criterion $J(\tau) = \sum_{i=0}^{P-1}[z_s[i] - (\alpha + \beta\exp(B\tau))]^2$. Differen-

tiating $J(\tau)$ w.r.t. τ, we obtain

$$\frac{\partial J(\tau)}{\partial \tau} = 2PB\beta \exp(B\tau)[\alpha + \beta \exp(B\tau) - \bar{z}_s]. \tag{5.20}$$

Setting $\frac{\partial J(\tau)}{\partial \tau} = 0$ we obtain

$$\hat{\tau} = \frac{1}{B} \ln\left(\frac{\bar{z}_s - \alpha}{\beta}\right). \tag{5.21}$$

Since $\bar{z}_s - \alpha = \frac{\bar{z}_s \sigma_{\nu e}^2}{(P\sigma_{ze}^2 + \sigma_{\nu e}^2)}$ and $\beta = \frac{Ad_i \sigma_{\nu e}^2}{(P\sigma_{ze}^2 + \sigma_{\nu e}^2)}$, (5.21) can be expressed as

$$\begin{aligned} \hat{\tau} &= \frac{1}{B} \ln\left(\sum_{i=0}^{P-1} z_s[i] \Big/ (PAd_i)\right) \\ &= \frac{1}{B} \ln\left(\frac{|\bar{z}_s|}{A}\right), \end{aligned} \tag{5.22}$$

which is equal to the ML estimate of τ in (5.11).

5.3.4 Determination of E_s, A and B

Estimating the symbol energy

An estimation of the symbol energy at the receiver front-end can be obtained by integrating the received signal over a reasonably long time interval as follows

$$\hat{E}_s = \frac{\sum_{k=0}^{KN_s-1} r_k^2 - \sigma^2 KN_s}{K}, \tag{5.23}$$

where K is the number of symbols within the time interval used for symbol energy estimation and $N_s = T_s/T_{samp}$ is the number of samples per symbol. $r_k = r(kT_{samp})$ is the k^{th} sample of $r(t)$.

Determining A and B

The mathematical procedure for finding the best-fitting curve to a given set of points by minimizing the sum of the squares of the offsets ("the residuals") of the points from the curve is known as *least squares fitting* [73] [74]. A and B can be determined offline through least squares exponential fitting of the average of the normalized equivalent system model $z_{e\tau}$ over several channel realizations, as is shown in Appendix IV.
For distance measurement applications, A and B are tuning parameters that can be determined during the calibration phase for making accurate measurements.

5.3.5 Simulation Results

In this subsection, the simulation results are presented. The performance of our data-aided timing offset estimator is demonstrated for different TR-UWB systems by using the

following performance metrics: the normalized estimation mean square error (MSE) given by mse= $\mathsf{E}\{(\hat{\tau}-\tau)^2\}/T_s^2$, the root mean square error rmse= $\sqrt{\mathsf{E}\{(\hat{\tau}-\tau)^2\}}$ and the bias (estimation error). We define the bias of our estimator to be $\text{Bias}(\hat{\tau}) = \mathsf{E}\{\hat{\tau}-\tau\} = \mathsf{E}\{\hat{\tau}\}-\tau$. The channel model used, is the IEEE 802.15.4a CM3 model for indoor office environment [37], with RMS delay spread $\tau_{rms} = 12$ ns. The different systems used and their simulation parameters are shown in Table 5.1.

TR-UWB systems ⇒ Parameters ⇓	**DTR UWB**	**LDC DTR-UWB**	**BLDC DTR-UWB**	**DP TR-UWB**
T_ω [ns]	0.7	0.7	0.7	0.7
τ_m [ns]	0.2877	0.2877	0.2877	0.2877
T_{samp} [ns]	0.05	0.05	0.05	0.05
T_f [ns]	100	16	2	20
T_I [ns]	20	20	20	20
T_s [ns]	1000	200	100	200
N_f	10	5	9	2
N_{cr}	10	4	8	1

Table 5.1: TR-UWB systems and simulation parameters

Fig. 5.7 - Fig. 5.9 depict the MSE of our timing offset estimator plotted versus SNR for values of $P = 64$, 256 and for different TR-UWB systems. Solid lines show the performance with known E_s and dash-dot lines show the performance with estimated E_s. For all the TR-UWB systems considered, it can be observed that, as P increases, the normalized MSE decreases monotonically. The same trend can be observed for increasing SNR. At SNRs above 20 dB the MSE of our timing offset estimator with estimated E_s get closer to the MSE of our timing offset estimator with known E_s. This confirms the good accuracy of our energy estimator at SNR>20 dB. For all the TR-UWB systems, the MSE curves flatten at high SNR towards a certain error floor. This error floor is related to P (amount of averaging) and T_f (average pulse separation).

IFI plays an important role in the observed error floor as shown in Fig. 5.10, where the rmse of our timing offset estimation technique is plotted versus SNR for different TR-UWB systems. BLDC DTR-UWB system is the burst-oriented type of the low duty cycle (LDC) DTR-UWB, with pulse-burst of 16 ns compared to the pulse presence of 64 ns for LDC DTR-UWB system. It can be observed that the BLDC DTR-UWB system, which has severe IFI, has the highest level of error floor. For other TR-UWB systems, as T_f is increased, the error floor decreases monotonically.

Fig. 5.11 confirms (5.13) since the performance of our timing offset estimator is related to the delay. This is due to the exponential fitting, where $z_{e\tau}$ values get closer to each other as delay increases, making it difficult to resolve them.

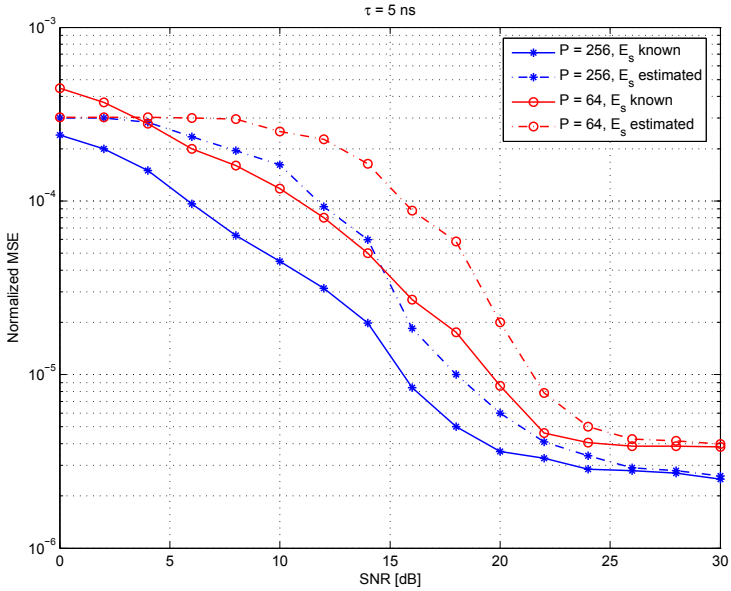

Figure 5.7: Normalized timing offset estimation MSE vs. SNR for DTR-UWB systems, $P = \{64, 256\}$.

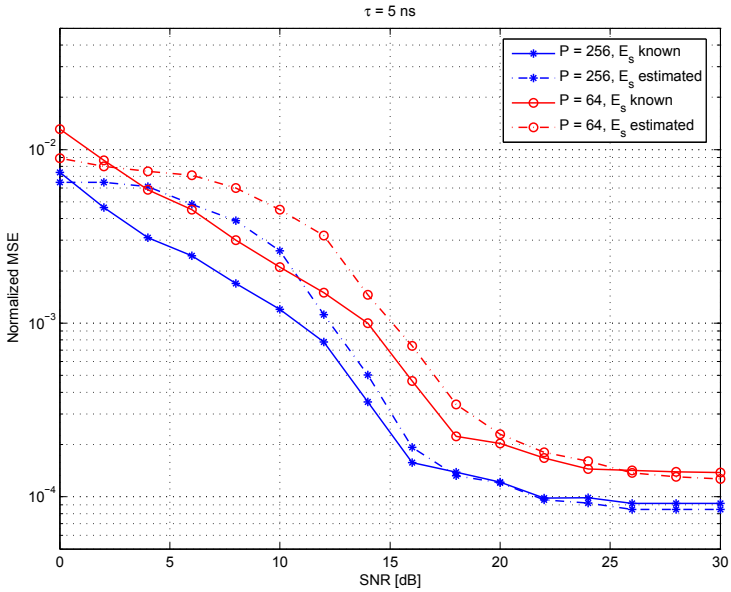

Figure 5.8: Normalized timing offset estimation MSE vs. SNR for LDC DTR-UWB systems, $P = \{64, 256\}$.

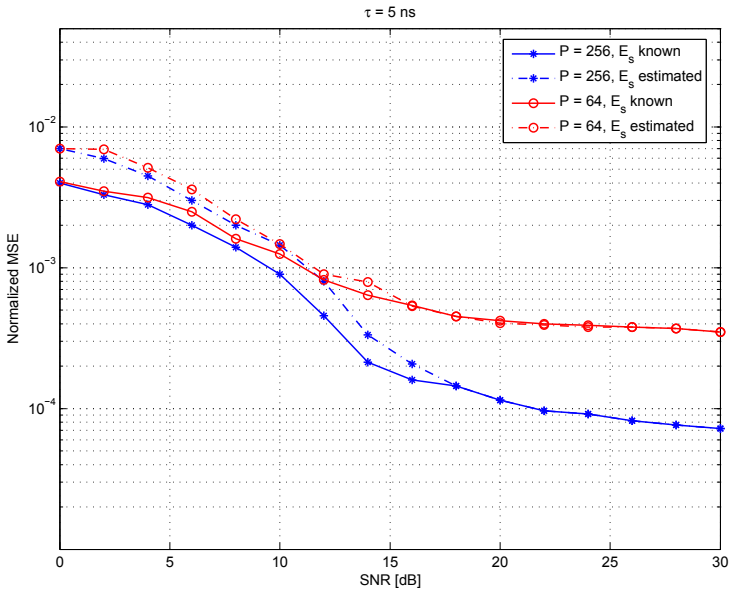

Figure 5.9: Normalized timing offset estimation MSE vs. SNR for DP TR-UWB systems, $P = \{64, 256\}$.

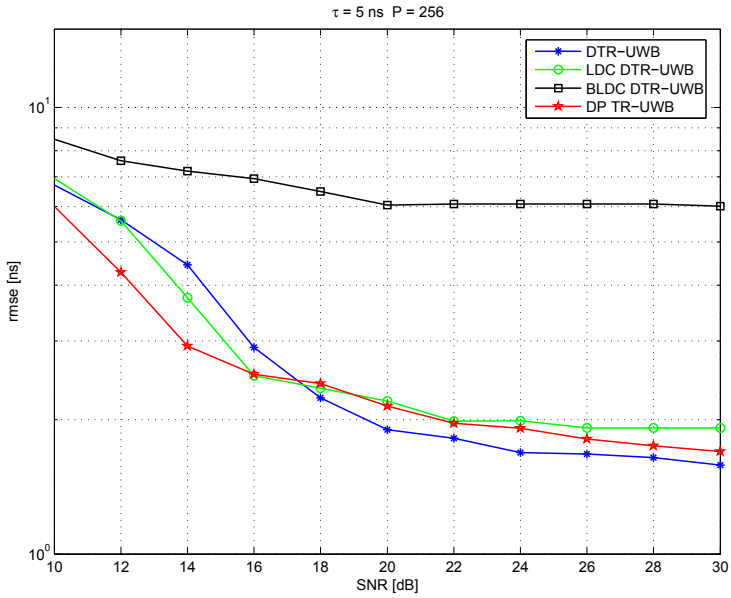

Figure 5.10: Timing offset estimation rmse vs. SNR for different TR-UWB systems.

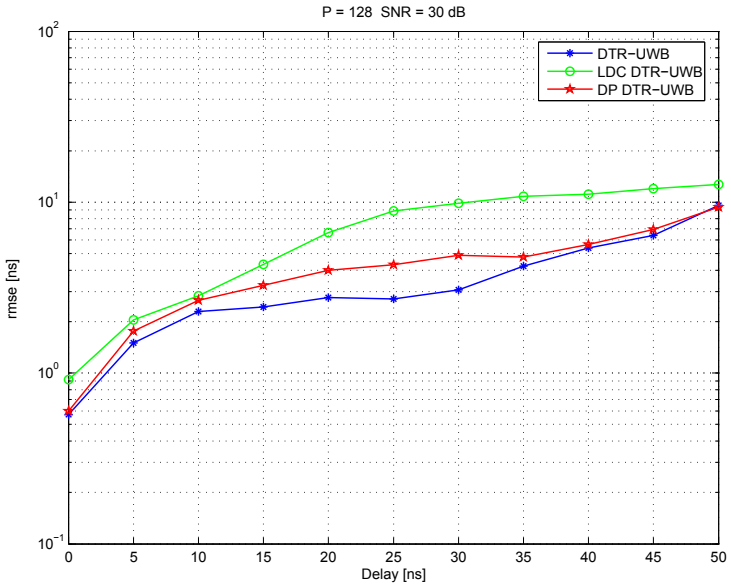

Figure 5.11: Timing offset estimation rmse vs. delay for different TR-UWB systems.

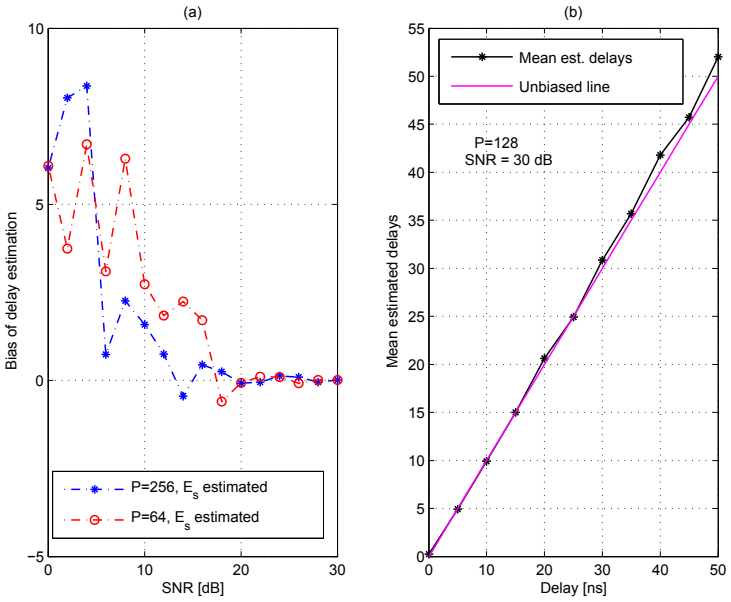

Figure 5.12: Biasedness of timing offset estimator for DTR-UWB systems, (a) vs. SNR (b) vs. delay.

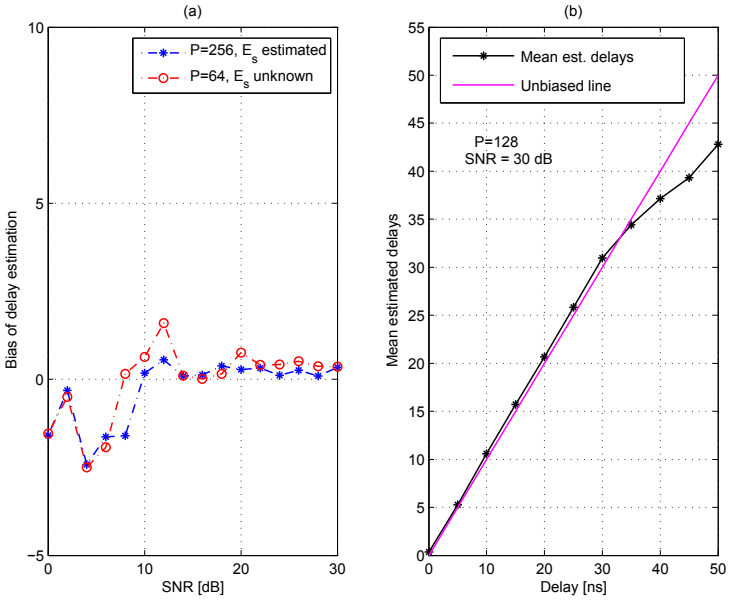

Figure 5.13: Biasedness of timing offset estimator for LDC DTR-UWB systems, (a) vs. SNR (b) vs. delay.

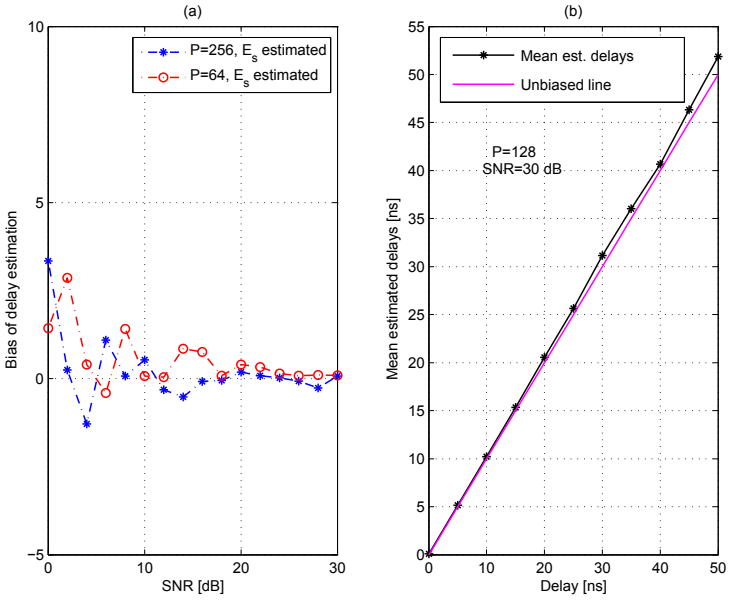

Figure 5.14: Biasedness of timing offset estimator for DP TR-UWB systems, (a) vs. SNR (b) vs. delay.

Fig. 5.12 - Fig. 5.14 depict the biasedness of our timing offset estimator plotted versus SNR and delay for values of $P = 64$, 256 and for different TR-UWB systems. This knowledge contributes in deciding the operating SNR and range (looking also at Fig. 5.11) of our timing offset estimator. For conventional DTR-UWB and dual pulse (DP) TR-UWB systems the biasedness of our estimator is negligible from 20 dB onwards, which is not the case for LDC DTR-UWB system which exhibits some small biasedness.

5.4 Summary

In this chapter, a novel data-aided timing acquisition technique for DTR-UWB systems was presented. The main signal processing techniques used were:

- Averaging of the received signal
- Fractional sampling
- Maximum selection criterion

The technique proposed is limited by the frame resolution which can be overcome through timing offset estimation, which was also presented, in this chapter, for low complexity TR-UWB systems. The proposed data-aided timing offset estimator uses energy collected at the symbol rate, thus reducing considerably the implementation complexity.
Simulation results provided a thorough performance analysis of the timing acquisition technique in terms of timing acquisition MSE, probability of correct detection and average BER. For the timing offset estimator, the performance metrics used were the normalized estimation MSE and estimation error (biasedness). The CRLB for such timing offset estimation approach was also derived.

Chapter 6

Localization with Transmitted Reference Systems

6.1 Introduction

Emergence of location based services requires a technical solution for accurate indoor localization of persons and objects. As satellite based positioning systems are not readily applicable to indoor localization, alternative solutions are needed.

Indoor wireless systems have to cope with severe multipath scenarios. Due to their extremely large bandwidth, UWB signals offer a good multipath resolution and enable accurate localization. UWB localization approaches can be divided into *Time of Arrival* (TOA), *Time-difference of Arrival* (TDOA), *Angle of Arrival* (AOA) and *Received Signal Strength* (RSS) based systems.

There are various existing and potential applications of high precision localization using UWB technology. An UWB precision location system [75] can be used to identify and locate valuable assets, for example, in hospitals, industrial fields and government offices. In [12] a low cost and small size UWB ASIC (application specific integrated circuit) is proposed for outdoor sport and recreational activities. The architecture and implementation status of a low-cost experimental UWB localization system is reported in [76]. It is designed to enable practical evaluations of UWB based positioning concepts. Another potential application is in WSN. Awareness of sensor positions may effectively improve network performance. For instance, location-aware routing protocols can reduce routing overhead and save energy by avoiding route search [77]. In [78] a novel packet routing scheme for UWB ad-hoc network is proposed and evaluated. This routing scheme employs UWB's features and controls spreading factor according to the distance between the nodes. When controlling the maximum transmission distance and adopting multi-hop transmission, the throughput performance can be improved as compared to single-hop transmission. Another position based routing strategy which exploits the high precision ranging capabilities offered by UWB is presented in [79]. It is shown that if a position-aware routing protocol and a power-aware routing metric based on ranging measurements are adopted, emitted power levels as well as multi-user interference are significantly reduced.

The system proposed in this chapter deals with UWB localization based on the timing

offset estimation algorithm presented in section 5.3. This algorithm can readily be used for distance measurement since $c = d/\tau$, where c is the speed of light and d is the distance travelled by light or other electromagnetic waves during a time span τ. Our algorithm provides a new aspect in distance measurement and is similar to the RSS technique. The difference is that the RSS technique relies on the knowledge of the path loss model for accurate and reliable distance estimation, whereas our algorithm uses the statistical analysis of the energy collected at the output of the receiver. Generally, the RSS metric is relatively simple to detect and no high synchronization effort and protocols are needed like in the TOA based solutions. Moreover, TOA based systems are sensitive to the available bandwidth, and also to the occurrence of UDP channel conditions, whereas RSS based systems are less sensitive to the available bandwidth and more resilient to UDP conditions. Nevertheless, it is not expected that RSS methods can match the precision of time-based methods. The achievable accuracy in RSS localization decreases with the distance, which has to been taken into consideration in the system design.

6.2 Localization Systems

Locating a node in a wireless system involves the collection of location information from radio signals traveling between the target node and a number of beacon nodes. Different measurement techniques for localization are discussed in this section from the viewpoint of UWB systems. The general system architecture of localization systems will be briefly discussed.

6.2.1 Ranging-based Systems

The most popular measurement technique for localization is *ranging*. There are two methods to obtain range measurements: *timing* and *signal strength*.

Timing

Time-based techniques rely on measurements of travel times of signals between nodes. If two nodes have a common clock, the node receiving the signal can determine the TOA of the incoming signal that is *time-stamped* by the reference node. The measured time can provide a circle of radius representing the distance between the node to be localized and the receiving node, centered at the latter. In two-dimensional localization, at least three circles are required as shown in Fig. 6.1.

This technique, also known as *trilateration*, is easy to implement; however, it requires knowledge of the transmission time of the emitted signal as well as synchronization of the transmitter and receivers clocks. Otherwise, considerable localization errors can occur. For instance, a clock inaccuracy of just 1 μs will lead to a position error of 300 m. Furthermore, this technique can suffer from multipath propagation effects.

In the TDOA technique the difference in time at which the signal from the node to be localized arrives at two different receivers is measured. Each time difference is then converted into a hyperbola with a constant distance between the two receivers. In two-dimensional

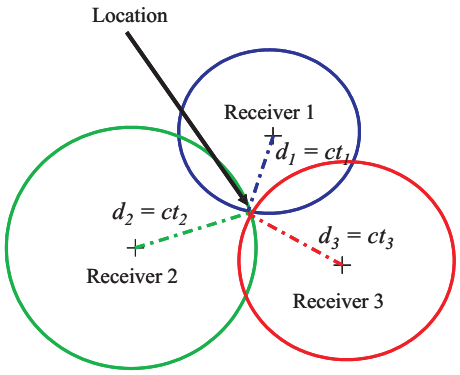

Figure 6.1: TOA localization principle.

localization, at least two pairs of receivers are required; the location is the intersection of the hyperbolas. This technique, known as *multilateration* or *hyperbolic positioning*, requires synchronization of the receivers' clocks; however, knowledge of the absolute transmission time of the emitted signal is no longer required. Here again, multipath propagation effects can influence the accuracy of the location of the receivers. Fig. 6.2 shows an example of TDOA localization. For both TOA and TDOA techniques, the wider the bandwidth of the signal the lower the measurement error becomes. This property allows extremely accurate location estimates using time-based techniques via UWB radios.

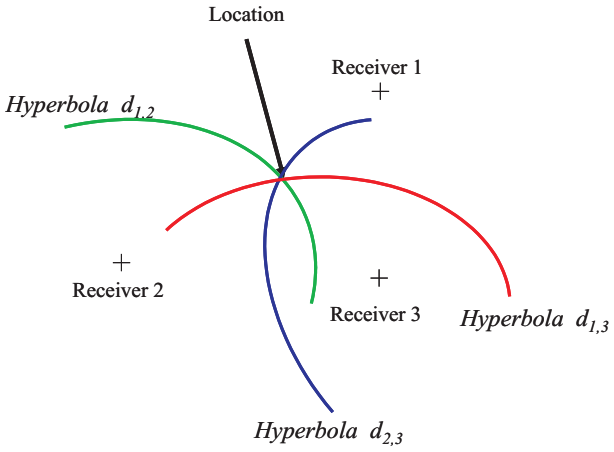

Figure 6.2: TDOA localization principle.

Signal Strength

With this technique the signal strength or energy of the node to be localized is measured at several stationary receivers. Ideally, each measurement will provide a circle of radius representing the distance between the node to be localized and the receiver that made this

measurement, centered at the corresponding receiver. The location of the node is then given by the intersection of these circles. In two-dimensional localization, and assuming no measurement error occurs, at least three circles are required in order to resolve the ambiguities arising from multiple crossings of the circles. The accuracy of the estimated location can be improved by increasing the number of measurements and then averaging the results. However, this approach requires an exact knowledge of the path loss in order to get an accurate estimation of the signal strength at the results.

Our Approach

We proposed a RSS-like technique that uses the statistical analysis of the distance-dependent discrete-time TR-UWB system models, instead of the path loss model, to estimate the distance d between the transmitter and the receiver. Indeed, considering $c = d/\tau$, where c is the speed of light in vacuum, (5.6) can be written as

$$z_s[i] = cz_{e\tau}[i] + cz_{e\tau\nu}[i] = z_{ed}[i] + z_{ed\nu}[i]. \tag{6.1}$$

At a time instant i, $z_{ed}[i]$ is a Gaussian random variable with mean $\mathsf{E}\{z_{ed}[i]\} = c\mathsf{E}\{z_{e\tau}[i]\}$ and variance $c^2\sigma_{ze}^2$. Hence, (5.8) becomes

$$\mathsf{E}\{z_{ed}[i]\} = Ad_i \exp(Bd/c). \tag{6.2}$$

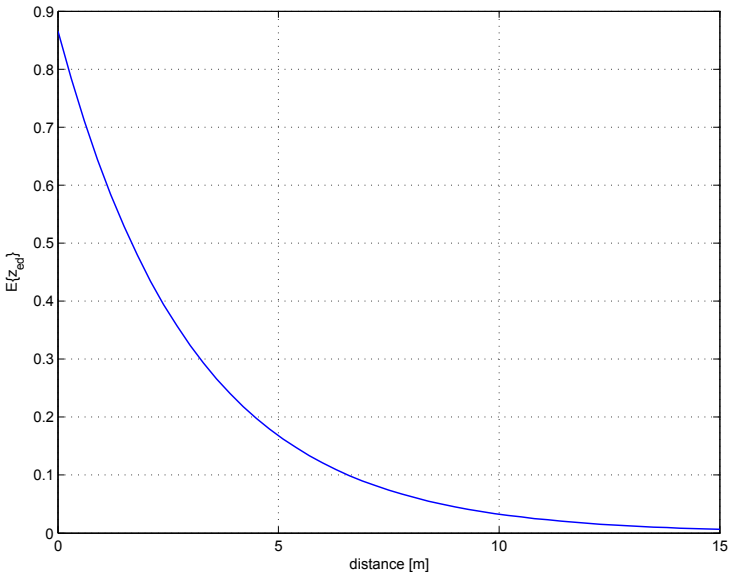

Figure 6.3: Normalized average distance-dependent noise-free decision variable

The distance dependence of $\mathsf{E}\{z_{ed}[i]\}$ is shown in Fig. 6.3, and is obtained by averaging z_{ed} over 1000 channel realizations. The maximum likelihood (ML) estimate of the distance between the transmitter and the receiver can be expressed as

$$\hat{d} = \frac{c}{B} \ln\left(\frac{|\bar{z}_s|}{A}\right). \tag{6.3}$$

The CRLB for the variance of the distance estimates is derived from (5.13) and is given by

$$CRLB(\hat{d}) = \frac{c^2(\sigma_{ze}^2 + \sigma_{\nu e}^2)}{PAB^2 \exp(Bd/c)\left[2A\exp(Bd/c) - |\bar{z}_s|\right]}. \tag{6.4}$$

6.2.2 Directionality-based Systems

Another way of estimating location is to measure the signal direction or angle of arrival (DOA/AOA) of the target node seen by reference nodes by steering the main lobe of a directional antenna or an adaptive antenna array. To determine the location of a node in a two-dimensional plane, it is sufficient to measure the angles of the straight lines that connect the node and two reference nodes, as shown in Fig. 6.4.

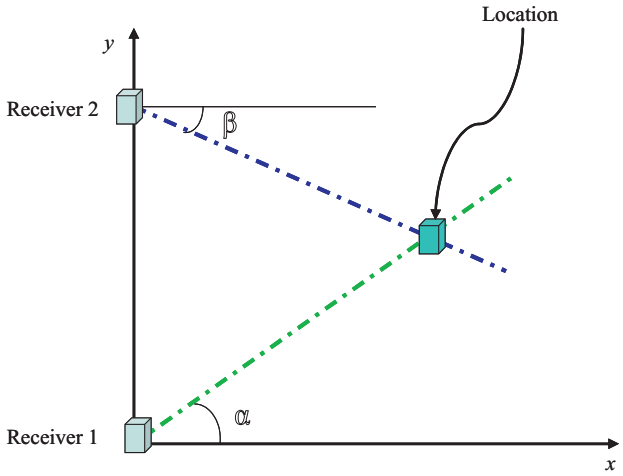

Figure 6.4: AOA localization principle.

This method is also called *triangulation* and it has the advantage of not requiring synchronization of the receivers nor an accurate timing reference. On the other hand, receivers require regular calibration in order to compensate for antenna mismatches.

The AOA approach is not suited to UWB localization for the following reasons:

- The use of antenna arrays increases the system cost, annulling the main advantage of a UWB radio equipped with low-cost transceivers.
- Due to the large bandwidth of a UWB signal, the number of paths may be very large, especially in indoor environments. Therefore, accurate angle estimation becomes very challenging due to scattering from objects in the environment.
- Time-based approaches can provide very precise location estimates, and therefore they are better motivated for UWB over the most costly AOA-based techniques.

Ranging and directionality-based systems can be termed as *Network-based systems*.

6.2.3 System Architecture

Localization systems using similar measurement techniques can differ considerably in their system architecture. We basically have centralized, hierarchical or decentralized architectures. The design of a localization system can also be largely influenced by application requirements. Certain applications require *tightly coupled* systems using beacon nodes that are wired to a centralized controller and placed at fixed positions, whereas for other applications *loosely coupled* systems are more appropriate. They use beacon nodes that are wireless and coordinate in a completely decentralized manner without central control.

Tightly coupled Systems

Several of the traditional localization technologies have a tightly coupled system architecture, motivated by application requirements. These applications generally require high accuracy and real-time tracking. Problems of time synchronization and coordination among beacon nodes are easily resolved because these systems are wired and have a centralized controller. These systems achieve high accuracy, but their drawback is that the centralized location estimation limits the number of devices they can simultaneously track. Secondly, wiring significantly impedes deployment. A key research challenge in these systems is achieving similar performance with outdoor applications, where deployment cannot be controlled and wiring may be infeasible.

Loosely coupled Systems

Motivated by deployment concerns, recently proposed localization systems are decentralized and completely wireless [80] - [84]. From all these systems the three approaches that meet the basic requirements for self-organization, robustness, and energy-efficiency are:

- Ad-hoc positioning [82]
- N-hop multilateration [84]
- Robust positioning [83].

These three algorithms are fully distributed and use local broadcast for communication with immediate neighbors. This last feature allows them to be executed before any multihop routing is in place, hence, they can support efficient location-based routing schemes. They use a three-phase approach for determining the individual node positions:

1. Determination of the distances between nodes and anchor nodes.
2. Derivation for each sensor node of its location from its beacon distances.
3. Refinement of the node locations using information about the range to, and locations of neighboring nodes.

The refinement phase is optional and may be included to obtain more accurate locations.

6.3 Location Estimation

In this section, the standard Least Squares (LS) [81] [82] and spherical-interpolation (SI) [85] methods for location estimation are described. For convenience, we assume that the nodes with known positions, (x_k, y_k, z_k), $k = 1, 2, \ldots, N$, are beacons while the nodes with unknown positions, (x, y, z) are sensors.

6.3.1 The LS algorithm

Let t_i be the TOA of the signal at anchor k, t_0 be the transmit time at the sensor and $d_k = c(t_k - t_0)$ be the range between the sensor and the k^{th} beacon node. Then, we obtain

$$d_k^2 = (x_k - x)^2 + (y_k - y)^2 + (z_k - z)^2. \tag{6.5}$$

Subtracting (6.5) for $k = 2, 3, \ldots, N$ by (6.5) for $k = 1$ produces

$$x_{k,1}x + y_{k,1}y + z_{k,1}z = b_{k,1}, \quad k = 2, \ldots, N, \tag{6.6}$$

where $x_{k,1} = x_k - x_1$, $y_{k,1} = y_k - y_1$, $z_{k,1} = z_k - z_1$ and $b_{k,1} = 0.5[(x_k^2 + y_k^2 + z_k^2) - (x_1^2 + y_1^2 + z_1^2) + d_1^2 - d_k^2]$. Equation (6.6) can be written in a compact form as

$$\mathbf{Ap}=\mathbf{b}, \tag{6.7}$$

where

$$\mathbf{A} = \begin{bmatrix} x_{2,1} & y_{2,1} & z_{2,1} \\ x_{3,1} & y_{3,1} & z_{3,1} \\ \vdots & \vdots & \vdots \\ x_{N,1} & y_{N,1} & z_{N,1} \end{bmatrix}, \quad \mathbf{p} = \begin{bmatrix} x \\ y \\ z \end{bmatrix}, \quad \mathbf{b} = \begin{bmatrix} b_{2,1} \\ b_{3,1} \\ \vdots \\ b_{N,1} \end{bmatrix}. \tag{6.8}$$

The standard LS solution to (6.7) is derived, as shown in Appendix V, as

$$\hat{\mathbf{p}}_{\boldsymbol{LS}} = \left(\mathbf{A}^T\mathbf{A}\right)^{-1}\mathbf{A}^T\mathbf{b}, \tag{6.9}$$

where the matrix inverse is supposed to exist and d_k are replaced by their corresponding estimates.

6.3.2 The SI Method

When the transmit time t_0 is unknown, TDOA measurements can be employed as for centralized networks. In this case, the SI method would be a suitable candidate. First, the spatial origin is mapped to one of the beacon nodes, say receiver 1, as shown in Fig. 6.5.

By defining $R_k = \sqrt{x_k^2 + y_k^2 + z_k^2}$, $\mathbf{p}_k = [x_k, y_k, z_k]^T$, $R = \sqrt{x^2 + y^2 + z^2}$ and $d_{k,l} = d_k - d_l$, d_k can be expressed using the Pythagorean theorem as

$$d_k^2 = R^2 + R_k^2 - 2\mathbf{p}_k^T\mathbf{p}. \tag{6.10}$$

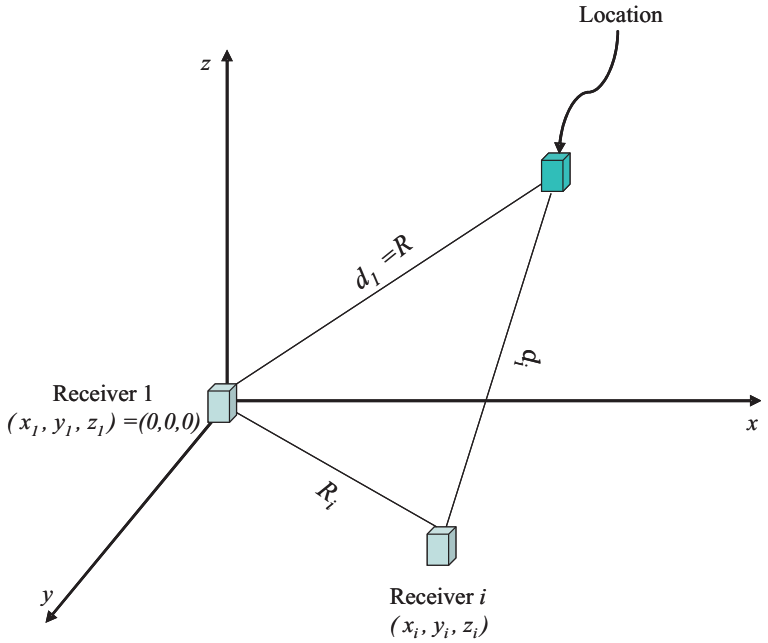

Figure 6.5: Illustration of the spherical interpolation approach.

where $\mathbf{p}$ is the location of the sensor node to be estimated. Since $d_1 = R$, $R - d_1 + d_k = d_k \Rightarrow d_k = R + d_{k1}$. (6.10) can be rewritten as

$$(R + d_{k1})^2 = R^2 + R_k^2 - 2\mathbf{p}_k^T\mathbf{p}, \quad k = 2, 3, \ldots, N. \tag{6.11}$$

In the presence of measurement errors, (6.11) becomes

$$\begin{aligned} (R + d_{k1})^2 + e_k &= R^2 + R_k^2 - 2\mathbf{p}_k^T\mathbf{p} \\ \Rightarrow e_k &= (R_k^2 - d_{k1})^2 - 2Rd_{k1} - 2\mathbf{p}_k^T\mathbf{p}, \end{aligned} \tag{6.12}$$

where e_k is the equation error. (6.12) can be written in compact form as

$$\mathbf{e} = \mathbf{r}_d - 2R\mathbf{d} - 2\mathbf{A}\mathbf{p}. \tag{6.13}$$

$\mathbf{A}$ is given by (6.8), $\mathbf{e}$ is the equation error vector, $\mathbf{r}_d = [R_2^2 - d_{21}^2, R_3^2 - d_{31}^2, \ldots, R_N^2 - d_{N1}^2]^T$ and $\mathbf{d} = [d_{21}, d_{31}, \ldots, d_{N1}]^T$.

The standard LS solution for $\mathbf{p}$, given R, is

$$\hat{\mathbf{p}} = \frac{1}{2}\left(\mathbf{A}^T\mathbf{A}\right)^{-1}\mathbf{A}^T(\mathbf{r}_d - 2R\mathbf{d}). \tag{6.14}$$

A closed-form solution can be derived by substituting (6.14) in (6.13) and minimizing the equation again with respect to R.

Rewriting the equation error (6.13) to eliminate $\mathbf{p}$ by substituting the value from (6.14), we get

$$\tilde{\mathbf{e}} = \mathbf{r}_d - 2R\mathbf{d} - \mathbf{A}\left(\mathbf{A}^T\mathbf{A}\right)^{-1}\mathbf{A}^T(\mathbf{r}_d - 2R\mathbf{d}) = (\mathbf{I}_{N-1} - \mathbf{A}_s)(\mathbf{r}_d - 2R\mathbf{d}), \tag{6.15}$$

where $\mathbf{A}_s = \mathbf{A}\left(\mathbf{A}^T\mathbf{A}\right)^{-1}\mathbf{A}^T$.

The error criterion can be expressed as

$$J(R) = \tilde{\mathbf{e}}^T\tilde{\mathbf{e}} = (\mathbf{r}_d - 2R\mathbf{d})^T\mathbf{B}(\mathbf{r}_d - 2R\mathbf{d}), \tag{6.16}$$

where $\mathbf{B} = (\mathbf{I}_{\mathrm{N}-1} - \mathbf{A}_{\mathrm{s}})^{\mathrm{T}}(\mathbf{I}_{\mathrm{N}-1} - \mathbf{A}_{\mathrm{s}})$ and $\mathbf{I}_{\mathrm{N}-1}$ denotes an identity matrix of size $N-1 \times N-1$. Minimizing J with respect to R is a form of *weighted* LS in which the weighting matrix $\mathbf{B}$ is idempotent of rank $N-4$ [85]. For this reason more than four beacon nodes are needed for the SI method.

Differentiating (6.16) with respect to R and setting $\frac{\partial J}{\partial R} = 0$ we obtain

$$\tilde{R} = \frac{1}{2}\frac{\mathbf{d}^T\mathbf{B}\mathbf{r}_d}{\mathbf{d}^T\mathbf{B}\mathbf{d}}. \tag{6.17}$$

Substituting this solution back into (6.14) yields the sensor node location estimate

$$\hat{\mathbf{p}}_{SI} = \frac{1}{2}\left(\mathbf{A}^T\mathbf{A}\right)^{-1}\mathbf{A}^T(\mathbf{r}_d - \frac{\mathbf{d}^T\mathbf{B}\mathbf{r}_d\mathbf{d}}{\mathbf{d}^T\mathbf{B}\mathbf{d}}). \tag{6.18}$$

6.3.3 Simulation results

The simulation results are presented in this subsection. The performance of the proposed distance estimator is demonstrated for different TR-UWB systems by using the following performance metrics: $\mathrm{rmse}(\hat{d}) = \sqrt{\mathsf{E}\{(\hat{d}-d)^2\}}$ and the distance estimation variance which can be defined from the MSE and the bias of d as $\mathrm{Var}(\hat{d}) = \mathsf{E}\{(\hat{d}-d)^2\} - [\mathrm{Bias}(\hat{d})]^2$.

The IEEE 802.15.4a CM3 channel model for indoor office environment, with RMS delay spread $\tau_{rms} = 12$ ns, is used once again. The different systems used and their simulation parameters are shown in Table 5.1.

Using a training sequence of length $P = 128$ and operating the TR-UWB receivers at a SNR of 30 dB, the rmse of the distance estimator in (6.3) is shown in Fig. 6.6.

It can be observed that, for all TR-UWB systems considered, the rmse increase monotonically with distance. At distance within 15 m the DTR-UWB system has a superior distance measuring performance. The TR-UWB system with relatively worst distance measuring performance is the low duty cycle (LDC) DTR-UWB system. This is because it has the lowest average frame duration, which means it is more affected by IFI. It should also be noted that the DTR-UWB system is able to provide centimeter accuracy for a transmitter-receiver separation up to 10 m. The variance of the distance estimator for the three TR-UWB systems considered is shown in Fig. 6.7.

Next, the localization capability of our three TR-UWB systems is analyzed. For this purpose the proposed simulation setup is shown in Fig. 6.8. A typical laboratory room or field size of 10 m $\times$ 6 m is illustrated. A local 2D reference system is used.

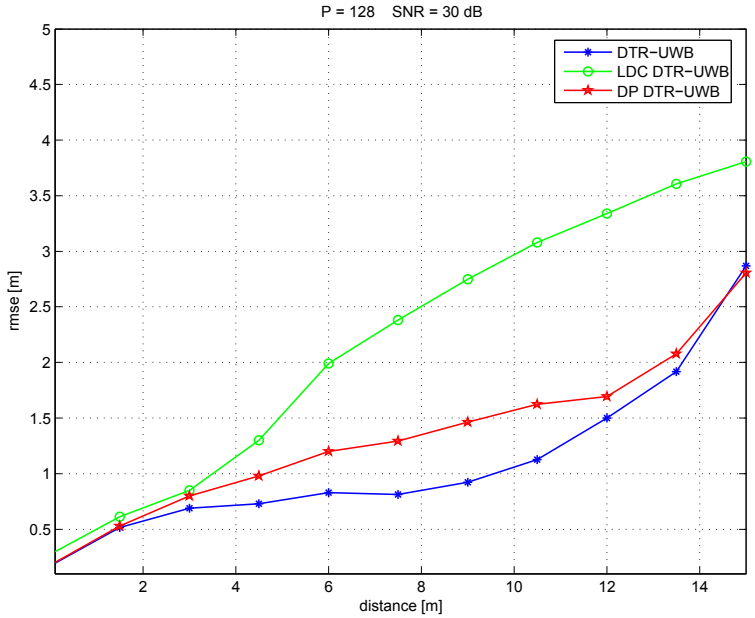

Figure 6.6: Distance estimation rmse vs. distance transmitter-receiver for different TR-UWB systems.

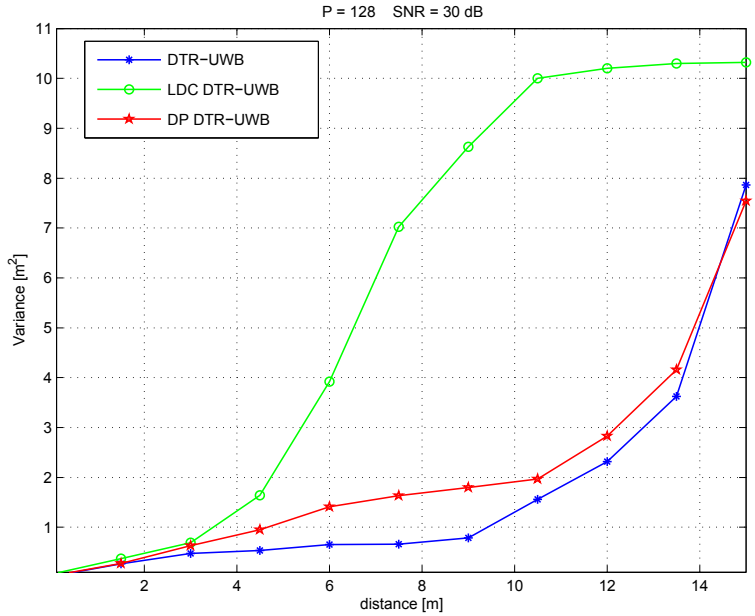

Figure 6.7: Distance estimation variance vs. distance transmitter-receiver for different TR-UWB systems.

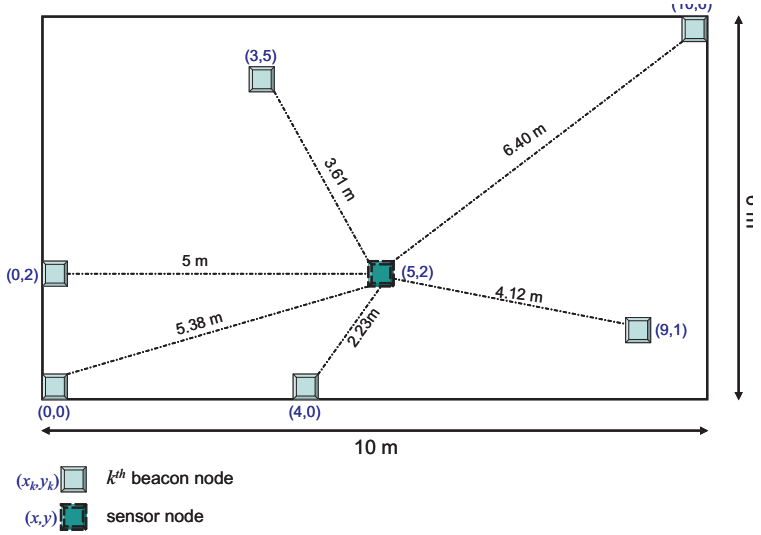

Figure 6.8: 2D localization scenario.

Both location estimation methods described in section 6.3 are used to localize the sensor node. The different beacon nodes are positioned in such a way that the matrix $\mathbf{A}$ is non-singular, hence invertible. This is ensured by not allowing more than two beacon nodes to have the same X or Y coordinates. For simulation purpose, the sensor node is localized at the location $(x = 5, y = 2)$. Using both the LS and SI localization methods, different location estimates for different TR-UWB systems are shown in Fig. 6.9 - Fig. 6.11.

The dots "$\cdot$" represent the location estimates of the sensor node using 100 Monte Carlo runs, whereas the star "$\star$" indicates the true sensor node location. It can be observed, for all TR-UWB systems considered, that the SI method exhibits less dispersion of the location estimates than the LS method. Indeed, with the LS method, more outliers are observed. Thus, the SI method is more precise than the LS method. Moreover, the SI method is more accurate than the LS method as can be seen in Tab. 6.1 where the localization accuracy is illustrated. This is because the SI method is analogous to the weighted LS method. It can also be observed that the DTR-UWB and dual pulse (DP) TR-UWB systems exhibit less outliers than the LDC DTR-UWB system, and they are more suitable for localization. In Tab. 6.1 the localization error is defined by $\epsilon = \sqrt{(\hat{x} - x)^2 + (\hat{y} - y)^2}$, where $\hat{x}$ and $\hat{y}$ are the estimates of the X and Y coordinates of the sensor node, respectively.

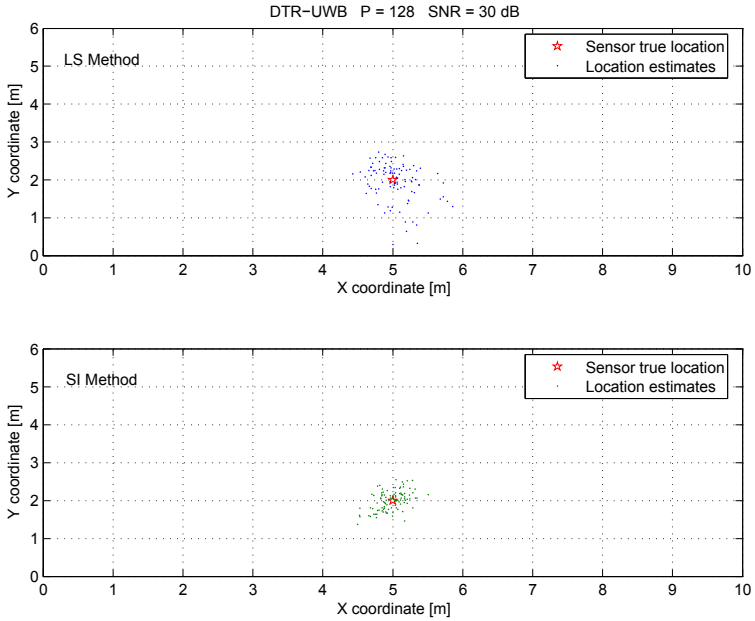

Figure 6.9: Location estimation with DTR-UWB systems.

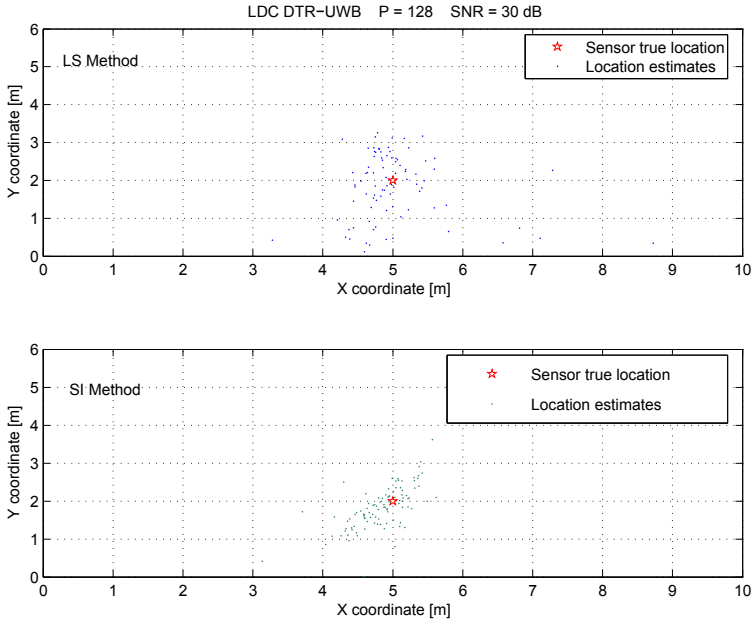

Figure 6.10: Location estimation with LDC DTR-UWB systems.

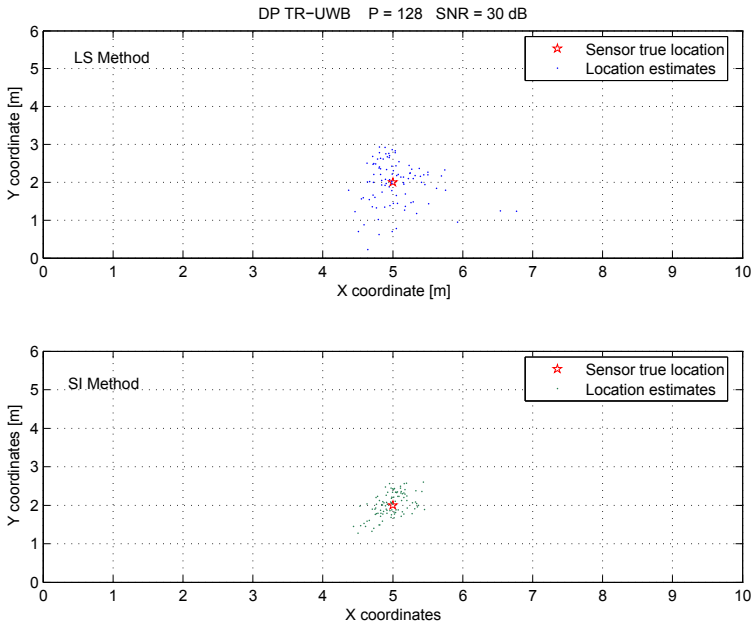

Figure 6.11: Location estimation with DP TR-UWB systems.

TR-UWB systems ⇒ Performance ⇓	**DTR UWB** $\eta = 0$	**LDC DTR-UWB**	**DP TR-UWB**
Average $\hat{\mathbf{p}}_{\boldsymbol{LS}}$	(5.041,1.944)	(4.886,1.341)	(5.035,1.948)
Average $\hat{\mathbf{p}}_{\boldsymbol{SI}}$	(4.982,1.999)	(4.822,1.802)	(4.976,2.015)
Average ϵ_{LS} [cm]	48.43	127.6	59.95
Average ϵ_{SI} [cm]	28.57	58.702	33.60

Table 6.1: Localization accuracy of different TR-UWB systems.

6.4 Summary

Localization with different TR-UWB systems was dealt with in this chapter. Different distance measurement techniques were presented, namely the TOA, TDOA, AOA and RSS methods. A new approach to distance measurement, similar to the RSS technique was introduced. It uses the statistical analysis of the energy collected at the output of the receiver rather than relying on the knowledge of the path loss model in RSS technique. The performance of the proposed distance estimator was demonstrated for different TR-UWB systems. Further, the localization capability of the considered TR-UWB systems were analyzed using the LS and SI localization methods. Simulation results have shown the superiority of the SI method over the LS method. It was also shown that the DTR-UWB and DP TR-UWB are more suitable for localization than LDC DTR-UWB system.

Chapter 7

Conclusions and Outlook

7.1 Conclusions

The main objective of this doctoral thesis is to present the conceptual design and analysis of a transmitted reference (TR)-UWB impulse response (IR) receiver that has dual functionality in providing robust, low power data communication and accurate location information in wireless sensor networks (WSNs). TR signaling in combination with an autocorrelation receiver (AcR) is especially suitable in this context because it allows a lower design complexity compared to coherent receivers. It allows higher accuracy in distance measurement as well.

In this thesis, the theory of polynomial nonlinear systems was revisited. Volterra series expansions were also presented. Further, the Wiener and Hammerstein models, which are the simplified forms of the Volterra model, were discussed.

The efficient design of UWB communications systems requires an appropriate channel model that accurately describes the UWB propagation. The description and discussion of appropriate channel models for mobile radio systems and UWB radio systems, in particular, were provided in this thesis. Emphasis was made on the IEEE 802.15.4a standardized channel model for UWB Communications.

The polynomial nonlinear models and the channel models are important in the simulation and analysis of low complexity TR-UWB systems. The TR-UWB systems considered, in this thesis, are the differential transmitted reference (DTR)-UWB system, the low duty cycle (LDC) DTR-UWB system and the dual pulse (DP) TR-UWB system. Discrete-time equivalent system models for these TR-UWB systems were derived and their delay-dependence studied. TR-UWB receiver statistics were analyzed from two perspectives: Gaussian approximation on the noise terms in the receiver and the analysis using the equivalent system and noise models of the receiver. Both perspectives led to the BER performance analysis.

Synchronization is a particularly acute problem faced by UWB systems due to the fact that they employ low-power ultra-short pulses. Coarse synchronization and fine synchronization algorithms were developed and evaluated in this thesis, utilizing a known training sequence. A novel data-aided timing acquisition technique for frame-level synchronization of DTR-UWB systems was suggested. Furthermore, a simple timing offset estimator for

low complexity TR-UWB systems, assuming no ISI, was considered. Both the classical and bayesian approaches were used for estimating the timing offset. It was shown that both approaches yield the same timing offset estimate. The theoretical performance limit of such timing offset estimation was illustrated through the derived Cramer-Rao Lower Bound (CRLB) for the variance of the timing offset estimates.

Assuming that coarse synchronization has been achieved and hardware clock timing error is known, the proposed timing offset algorithm was used as a new approach for distance measurement. It is a RSS-like technique that uses the statistical analysis of the distance-dependent discrete-time TR-UWB system models, instead of the path loss model, to estimate the distance between the transmitter and the receiver. Different measurement techniques for localization were discussed in this thesis from the viewpoint of UWB systems. The general system architectures of localization systems were presented. Further, the performance of the proposed distance estimator was demonstrated for different TR-UWB systems. Finally, the localization capability of the considered TR-UWB systems were analyzed using the LS and SI localization methods.

7.2 Summary of Contributions

The main contributions of this thesis are summarized below

- **Low complexity TR systems**
  - Systems modelling
  - Performance analysis
    - Gaussian approximation using derived models
  - Average BER derivation
- **Synchronization and Localization**
  - Coarse synchronization
  - Fine synchronization
  - Distance and location estimation

7.3 Discussion and Recommendations

The equivalent system models for TR-UWB systems presented in this thesis constitute an important step towards developing an emulator for TR-UWB systems. Such emulator would be very useful for developing optimal and suboptimal detection algorithms for differential UWB communications systems under ISI or without ISI. It would also be a powerful tool for developing signal processing algorithms for equalization and synchronization.

The performance of the different TR-UWB systems studied is summarized in Tab. 7.1. DTR-UWB systems are recommended for short-range radio location-aware WSN applications with lower data rate requirement but higher localization accuracy requirement. DP TR-UWB systems have lower complexity, but provide higher data rate, when compared to DTR-UWB systems, at the expense of loosing some localization accuracy. Thus, they are recommended for short-range radio location-aware WSN applications with stringent low cost requirements.

TR-UWB systems ⇒ Performance ⇓	**DTR UWB** $\eta = 0$	**LDC DTR-UWB**	**DP TR-UWB**
Symbol rate [Mb/s]	1	5	5
Timing offset rmse [ns] ($\tau = 5$ ns, $P = 256$, SNR = 30 dB)	1.65	1.9	1.7
Mean localization error [cm] (LS method)	48.43	127.6	59.95
Mean localization error [cm] (SI method)	28.57	58.702	33.60

Table 7.1: Performance of different TR-UWB systems.

Sensor network localization has been an active area of research for the last few years. For WSNs, the ability for sensor nodes to determine their position through automatic means is recognized as an essential capability. The research community has made great strides in ranging technologies, systems for infrastructure-based localization, and algorithms and techniques for ad-hoc localization. UWB systems are being investigated for ad-hoc and wireless sensor networks, where it is not necessary to have fixed base stations like with conventional radio systems. Hence, each node need to have a routing function. A multi-hop transmission will also be necessary if the area cover is larger than the permitted distance of communication between nodes.

As already discussed in this thesis, the very large bandwidth of UWB technology, besides providing the possibility to transmit at very high data rate, also provides very accurate temporal and spatial information. This high accuracy allows for new prospectives in terms of synchronization, positioning and tracking. In the case of tracking a mobile sensor node in a wireless system, two recursive tracking algorithms, namely the extended Kalman filter (EKF) and the unscented Kalman filter (UKF), can be employed as smoothing algorithms on the location estimates. The Kalman filter is one of the best optimal recursive Bayesian estimator for linear tracking problems.

The design of an UWB indoor network as a local augmentation to the global navigation satellite system (GNSS) positioning, can be envisaged. It would enable a seamless absolute positioning and ensure a smooth outdoor-indoor transition. It would also help overcoming signal attenuation and extending coverage, by pseudo-ranging from low-level ground based UWB beacon nodes.

Further in this context is the development of a joint UWB-IR/inertial measurement unit (IMU) system for joint communication and positioning/location in industry and logistics scenarios. Such system be based on peer-to-peer mechanisms with network routing functionality. The system elements might be either mobile system elements or fixed system elements. The major difference is that fixed nodes are furnished with their absolute or relative position, whereas mobile nodes use fixed nodes to obtain their absolute or relative. Whether mobile or fixed, systems elements would comprise two loosely coupled parts: the UWB subsystem and the IMU subsystem. Both would provide data into a data fusion module computing enhanced position co-ordinates.

Appendix I
Gaussian Integral

The *Gaussian integral*, or *probability integral*, is an integral of the Gaussian function e^{-x^2}. It is expressed analytically as

$$\int_{-\infty}^{\infty} e^{-x^2} dx = \sqrt{\pi}. \tag{1}$$

The integral of any Gaussian function $ae^{-\left(\frac{bx+c}{f}\right)^2}$ is reducible in terms of the Gaussian integral.
Let make the change of variable $y = bx + c \Rightarrow dx = dy/b$,

$$\int_{-\infty}^{\infty} ae^{-\left(\frac{bx+c}{f}\right)^2} dx = \frac{a}{b} \int_{-\infty}^{+\infty} e^{-\left(\frac{y}{f}\right)^2} dy. \tag{2}$$

Substituting y with fz, and using (1) gives

$$\begin{aligned} \int_{-\infty}^{\infty} ae^{-\left(\frac{bx+c}{f}\right)^2} dx &= \frac{af}{b} \int_{-\infty}^{\infty} e^{-z^2} dz \\ &= \frac{af}{b}\sqrt{\pi}. \end{aligned} \tag{3}$$

The integrals of the exponential functions $x^2e^{-bx^2}$ and $x^ne^{-bx^2}$ are definite and are expressed analytically as

$$\int_{-\infty}^{\infty} x^2 e^{-bx^2} dx = \tfrac{1}{2}\sqrt{\tfrac{\pi}{b^3}} \quad b > 0, \tag{4}$$

$$\int_{-\infty}^{\infty} x^n e^{-bx^2} dx = \begin{cases} \frac{(2k-1)!!}{2^{k+1}b^k}\sqrt{\frac{\pi}{b}} & b > 0, n = 2k, k \in \mathbb{Z} \\ \\ \frac{k!}{2b^{k+1}} & n = (2k+1) \end{cases}, \tag{5}$$

where $\mathbb{Z}$ is the field of integers, $n!!$ denotes the double factorial of n and is defined recursively by

$$n!! = \begin{cases} 1 & \text{if} n \in \{-1, 0, 1\} \\ n(n-2)!! & \text{if} n \geq 2 \end{cases} . \tag{6}$$

For example, $8!! = 2 \cdot 4 \cdot 6 \cdot 8 = 384$ and $9!! = 1 \cdot 3 \cdot 5 \cdot 7 \cdot 9 = 945$. Some identities involving double factorials are

$$\begin{aligned} (2n)!! &= 2^n n! \\ (2n+1)!! &= \tfrac{(2n+1)!}{2^n n!}. \end{aligned} \tag{7}$$

Following the same change of variables as in (2) and (3), in this thesis, more general analytical expressions to (2) and (3) are given as

$$\int_{-\infty}^{\infty} ax^2 e^{-\left(\frac{bx+c^2}{f}\right)} dx = \tfrac{a}{2} \left(\tfrac{f}{b}\right)^3 \sqrt{\pi} \quad b > 0, \tag{8}$$

$$\int_{-\infty}^{\infty} ax^n e^{-\left(\frac{bx+c}{f}\right)^2} dx = \begin{cases} a \frac{(2k-1)!!}{2^{k+1} b^k} \left(\tfrac{f}{b}\right)^{2k+1} \sqrt{\pi} & n = 2k \\ a \frac{k!}{2} \left(\tfrac{f}{b}\right)^{2k+2} & n = 2k+1 \end{cases} . \tag{9}$$

Appendix II
Energy of Gaussian pulses

$$E_g = \int_{-\infty}^{\infty} \omega_g^2(t)dt = \int_{-\infty}^{\infty} K_1^2 e^{-4\pi(t/t_m)^2} dt. \tag{10}$$

Using (3) with $a = K_1^2$, $b = 2\sqrt{\pi}$ and $f = t_m$, we have

$$E_g = \frac{K_1^2 t_m}{2}. \tag{11}$$

$$E_{g_1} = \int_{-\infty}^{\infty} \omega_{g_1}^2(t)dt = \int_{-\infty}^{\infty} K_1^2 \frac{16\pi^2}{t_m^4} e^{-4\pi(t/t_m)^2} dt. \tag{12}$$

Using (8) with $a = \frac{16\pi^2 K_1^2}{t_m^4}$, $b = 2\sqrt{\pi}$ and $f = t_m$, we have

$$E_{g_1} = \frac{K_1^2 \pi}{t_m}. \tag{13}$$

$$\begin{aligned} E_{g_2} &= \int_{-\infty}^{\infty} \omega_{g_2}^2(t)dt = \int_{-\infty}^{\infty} \frac{16\pi^2 K_1^2}{t_m^4} \left(1 - \frac{4\pi t^2}{t_m^2}\right)^2 e^{-4\pi(t/t_m)^2} dt \\ &= \int_{-\infty}^{\infty} \frac{16\pi^2 K_1^2}{t_m^4} e^{-4\pi(t/t_m)^2} dt - \int_{-\infty}^{\infty} \frac{128\pi^3 K_1^2}{t_m^6} t^2 e^{-4\pi(t/t_m)^2} dt \\ &\quad + \int_{-\infty}^{\infty} \frac{16^2\pi^4 K_1^2}{t_m^8} t^4 e^{-4\pi(t/t_m)^2} dt \\ &= \frac{16\pi^2}{t_m^4} E_g - \frac{8\pi}{t_m^2} E_{g_1} + E_{g_{21}}. \end{aligned} \tag{14}$$

$E_{g_{21}}$ is computed using (9) with $a = \frac{16^2\pi^4 K_1^2}{t_m^8}$, $b = 2\sqrt{\pi}$, $f = t_m$, $n = 4$ and $k = 2$.

$$E_{g_{21}} = \frac{6\pi^2 K_1^2}{t_m^5}. \tag{15}$$

Since $\frac{16\pi^2}{t_m^4} E_g - \frac{8\pi}{t_m^2} E_{g_1} = 0$, we finally have

$$E_{g_2} = \frac{6\pi^2 K_1^2}{t_m^5}. \tag{16}$$

Appendix III
Posterior Probability Density Function

Using the Bayes' rule, we can express $p(z_{e\tau}|\mathbf{z}_s)$ as

$$\begin{aligned} p(z_{e\tau}|\mathbf{z}_s) &= \frac{p(\mathbf{z}_s|z_{e\tau})p(z_{e\tau})}{p(\mathbf{z}_s)} \\ &= \frac{p(\mathbf{z}_s|z_{e\tau})p(z_{e\tau})}{\int_{-\infty}^{\infty} p(\mathbf{z}_s|z_{e\tau})p(z_{e\tau})dz_{e\tau}}. \end{aligned} \tag{17}$$

Using (5.14) and (5.15), (17) can be expressed as

$$p(z_{e\tau}|\mathbf{z}_s) = \frac{\exp\left[-\frac{1}{2\sigma_{\nu e}^2}\sum_{i=0}^{P-1}(z_s[i]-z_{e\tau})^2\right]\exp\left[-\frac{1}{2\sigma_{ze}^2}(z_{e\tau}-\theta(\tau))^2\right]}{\int_{\infty}^{\infty}\exp\left[-\frac{1}{2\sigma_{\nu e}^2}\sum_{i=0}^{P-1}(z_s[i]-z_{e\tau})^2\right]\exp\left[-\frac{1}{2\sigma_{ze}^2}(z_{e\tau}-\theta(\tau))^2\right]dz_{e\tau}}, \tag{18}$$

where $\theta(\tau) = Ad_i\exp(B\tau)$. After simplification, we obtain

$$\begin{aligned} p(z_{e\tau}|\mathbf{z}_s) &= \frac{\exp\left[\frac{-1}{2}\left(\frac{1}{\sigma_{\nu e}^2}(Pz_{e\tau}^2-2Pz_{e\tau}\bar{z}_s)+\frac{1}{\sigma_{ze}^2}(z_{e\tau}-\theta(\tau))^2\right)\right]}{\int_{\infty}^{\infty}\exp\left[\frac{-1}{2}\left(\frac{1}{\sigma_{\nu e}^2}(Pz_{e\tau}^2-2Pz_{e\tau}\bar{z}_s)+\frac{1}{\sigma_{ze}^2}(z_{e\tau}-\theta(\tau))^2\right)\right]dz_{e\tau}} \\ &= \frac{\exp\left[\frac{-1}{2}f(z_{e\tau})\right]}{\int_{\infty}^{\infty}\exp\left[\frac{-1}{2}f(z_{e\tau})\right]dz_{e\tau}}. \end{aligned} \tag{19}$$

$f(z_{e\tau}) = \left(\frac{P}{\sigma_{\nu e}^2}+\frac{1}{\sigma_{ze}^2}\right)z_{e\tau}^2 - 2\left(\frac{P\bar{z}_s}{\sigma_{\nu e}^2}+\frac{\theta(\tau)}{\sigma_{ze}^2}\right)z_{e\tau}+\frac{\theta(\tau)^2}{\sigma_{ze}^2}$. This function is quadratic in $z_{e\tau}$. Let $v = \left(\frac{P}{\sigma_{\nu e}^2}+\frac{1}{\sigma_{ze}^2}\right)^{-1}$ and $m = \left(\frac{P\bar{z}_s}{\sigma_{\nu e}^2}+\frac{\theta(\tau)}{\sigma_{ze}^2}\right)v$, then we have

$$\begin{aligned} f(z_{e\tau}) &= \frac{1}{v}z_{e\tau}^2 - 2\frac{m}{v}z_{e\tau}+\frac{\theta^2(\tau)}{\sigma_{ze}^2} \\ &= \frac{1}{v}(z_{e\tau}^2-2mz_{e\tau}^2+m^2)-\frac{m^2}{v}+\frac{\theta^2(\tau)}{\sigma_{ze}^2} \\ &= \frac{1}{v}(z_{e\tau}-m)^2-\frac{m^2}{v}+\frac{\theta^2(\tau)}{\sigma_{ze}^2}. \end{aligned} \tag{20}$$

Putting the expression of (20) back into (17), we have

$$p(z_{e\tau}|\mathbf{z}_s) = \frac{\exp\left[-\frac{1}{2v}(z_{e\tau}-m)^2\right]\exp\left[-\frac{1}{2}\left(\frac{\theta^2(\tau)}{\sigma^2_{ze}}-\frac{m^2}{v}\right)\right]}{\int_{\infty}^{\infty}\exp\left[-\frac{1}{2v}(z_{e\tau}-m)^2\right]\exp\left[-\frac{1}{2}\left(\frac{\theta^2(\tau)}{\sigma^2_{ze}}-\frac{m^2}{v}\right)\right]dz_{e\tau}}. \quad (21)$$

Following the requirement that $p(z_{e\tau}|\mathbf{z})$ integrate to 1 [72], we finally have

$$p(z_{e\tau}|\mathbf{z}_s) = \frac{1}{\sqrt{2\pi v}}\exp\left[-\frac{1}{2v}(z_{e\tau}-m)^2\right]. \quad (22)$$

This shows that $z_{e\tau}$ conditioned on $\mathbf{z}_s$ is a Gaussian random variable with mean $m_{z_{e\tau}|z_s} = \left(\frac{P\bar{z}_s}{\sigma^2_{\nu e}}+\frac{\theta(\tau)}{\sigma^2_{ze}}\right)\left(\frac{P}{\sigma^2_{\nu e}}+\frac{1}{\sigma^2_{ze}}\right)^{-1}$ and variance $\sigma^2_{z_{e\tau}|z_s} = \left(\frac{P}{\sigma^2_{\nu e}}+\frac{1}{\sigma^2_{ze}}\right)^{-1}$.

Appendix IV
Least Squares Exponential Fitting

Let $\mathsf{E}\{z_{e\tau}\} = \bar{z}_e(n) = A\exp(Bn)$, where $n \in \{0, 1, \ldots, N-1\}$ are the different delay values in ns, as shown in Fig. 4.8 for $N = 51$.
Since $\ln(\bar{z}_e(n)) = \ln(A) + Bn = \varepsilon + \gamma n$, to determine A and B we start by minimizing the function

$$\chi^2(\varepsilon, \gamma) = \sum_{n=0}^{N-1} \bar{z}_e(n)[\ln(\bar{z}_e(n)) - \varepsilon - \gamma n]^2. \tag{23}$$

Applying least squares fitting gives

$$\begin{cases} \varepsilon \sum\limits_{n=0}^{N-1} \bar{z}_e(n) + \gamma \sum\limits_{n=0}^{N-1} n\bar{z}_e(n) = \sum\limits_{n=1}^{N} \bar{z}_e(n)\ln(\bar{z}_e(n)) \\ \varepsilon \sum\limits_{n=0}^{N-1} n\bar{z}_e(n) + \gamma \sum\limits_{n=0}^{N-1} n^2\bar{z}_e(n) = \sum\limits_{n=1}^{N} n\bar{z}_e(n)\ln(\bar{z}_e(n)) \end{cases} \tag{24}$$

The system of equation in (24) can be rewritten in matrix format

$$\begin{bmatrix} \sum\limits_{n=0}^{N-1} \bar{z}_e(n) & \sum\limits_{n=0}^{N-1} n\bar{z}_e(n) \\ \sum\limits_{n=0}^{N-1} n\bar{z}_e(n) & \sum\limits_{n=0}^{N-1} n^2\bar{z}_e(n) \end{bmatrix} \begin{bmatrix} \varepsilon \\ \gamma \end{bmatrix} = \begin{bmatrix} \sum\limits_{n=0}^{N-1} \bar{z}_e(n)\ln(\bar{z}_e(n)) \\ \sum\limits_{n=0}^{N-1} n\bar{z}_e(n)\ln(\bar{z}_e(n)) \end{bmatrix} \tag{25}$$

or

$$\mathbf{M}\begin{bmatrix} \varepsilon \\ \gamma \end{bmatrix} = \mathbf{m}. \tag{26}$$

ε and γ are obtained by solving (26).

$$\begin{bmatrix} \varepsilon \\ \gamma \end{bmatrix} = \mathbf{M}^{-1}\mathbf{m}. \tag{27}$$

Finally, A and B are expressed as

$$\begin{aligned} A &= \exp(\varepsilon) \\ B &= \gamma. \end{aligned} \tag{28}$$

Appendix V
Linear Least Squares

Let us consider a data model expressed as

$$x[n] = s[n] + w[n], \quad n = 0, 1, \cdots, N-1. \tag{29}$$

$w[n]$ is a zero mean noise process and $s[n]$ is the signal model. (29) can be expressed in compact form as

$$\mathbf{x} = \mathbf{s} + \mathbf{w}. \tag{30}$$

Let us consider a unknown vector parameter $\boldsymbol{\theta}$= $[\theta_1, \theta_2, \ldots, \theta_p]$ of dimension $p \times 1$ to be estimated. For the signal $\mathbf{s}$=$[s[0], s[1], \ldots, s[N-1]]^T$ to be linear in the unknown parameters, it is assumed, using matrix notation, that

$$\mathbf{s} = \mathbf{H}\boldsymbol{\theta}, \tag{31}$$

where $\mathbf{H}$ is a known $N \times p$ matrix ($N > p$) of rank p. The matrix $\mathbf{H}$ is known as the *observation matrix*. The *least square error* (LSE) is found by minimizing

$$\begin{aligned} J(\boldsymbol{\theta}) &= \sum_{n=0}^{N-1} (x[n] - s[n])^2 \\ &= (\mathbf{x} - \mathbf{H}\boldsymbol{\theta})^T (\mathbf{x} - \mathbf{H}\boldsymbol{\theta}) \\ &= \mathbf{x}^T\mathbf{x} - \mathbf{x}^T\mathbf{H}\boldsymbol{\theta} - \boldsymbol{\theta}^T\mathbf{H}^T\mathbf{x} + \boldsymbol{\theta}^T\mathbf{H}^T\mathbf{H}\boldsymbol{\theta} \\ &= \mathbf{x}^T\mathbf{x} - \mathbf{x}^T - 2\mathbf{x}^T\mathbf{H}\boldsymbol{\theta} + \boldsymbol{\theta}^T\mathbf{H}^T\mathbf{H}\boldsymbol{\theta}. \end{aligned} \tag{32}$$

It is important noting that $\mathbf{x}^T\mathbf{H}\boldsymbol{\theta}$ is a scalar and J is a quadratic function of $\boldsymbol{\theta}$. The gradient $\partial J(\boldsymbol{\theta})/\partial\boldsymbol{\theta}$ is expressed as

$$\frac{\partial J(\boldsymbol{\theta})}{\partial \boldsymbol{\theta}} = -2\mathbf{H}^T\mathbf{x} + 2\mathbf{H}^T\mathbf{H}\boldsymbol{\theta}. \tag{33}$$

Setting the gradient equal to zero yields the LSE

$$\hat{\boldsymbol{\theta}} = (\mathbf{H}^T\mathbf{H})^{-1}\mathbf{H}^T\mathbf{x}. \tag{34}$$

Appendix VI
Design of ZESS wireless sensor nodes

Design of sensor nodes

1. *Hardware Selection*
   In our completed experimental implementation of a sensor node we feed the digital input data from a digital source such as a personal computer (PC) via a USB interface to an 8051-compatible microcontroller. The sensor module is represented by a GPS module.
   The signal processing and network protocol functions are handled by the Cypress Semiconductor's EZ-USB which is an enhanced 8051 core with fast execution time and added features. It uses internal RAM for program and data storage, making it a *soft* solution. The EZ-USB chip operates at 3.3V.
   The radio module used is a single chip 2.4 GHz Gaussian Frequency Shift Keying (GFSK) transceiver based on the HomeRF technology and capable of delivering data rate up to 1 Mbps.
   An illustration of the experimental design of a sensor node with wireless communication capabilities is shown in Fig. 1.

2. *Firmware Development*
   Generally, a firmware is software (programs or data) that is embedded in a hardware device, allowing reading and execution of the software, but does not allow modification, as for example, writing or deleting data by an end user. A great feature of the firmware we developed is that it can be modified. This is because of the soft (RAM-based) feature of the EZ-USB microcontroller that allows unlimited configuration and upgrades.

Integration of GPS data

The main objective of this work is to provide our sensor nodes with positioning information for localization purposes in WSN. This work consists of three tasks:

1. *Serial Interface of a Handheld GPS Receiver*
   Based on the strictly low energy consumption requirements of sensor nodes, we have decided to select the *Lassen*® IQ GPS module whose main features are: ultra low power consumption - economical price - Aided GPS (A-GPS) capability through TSIP

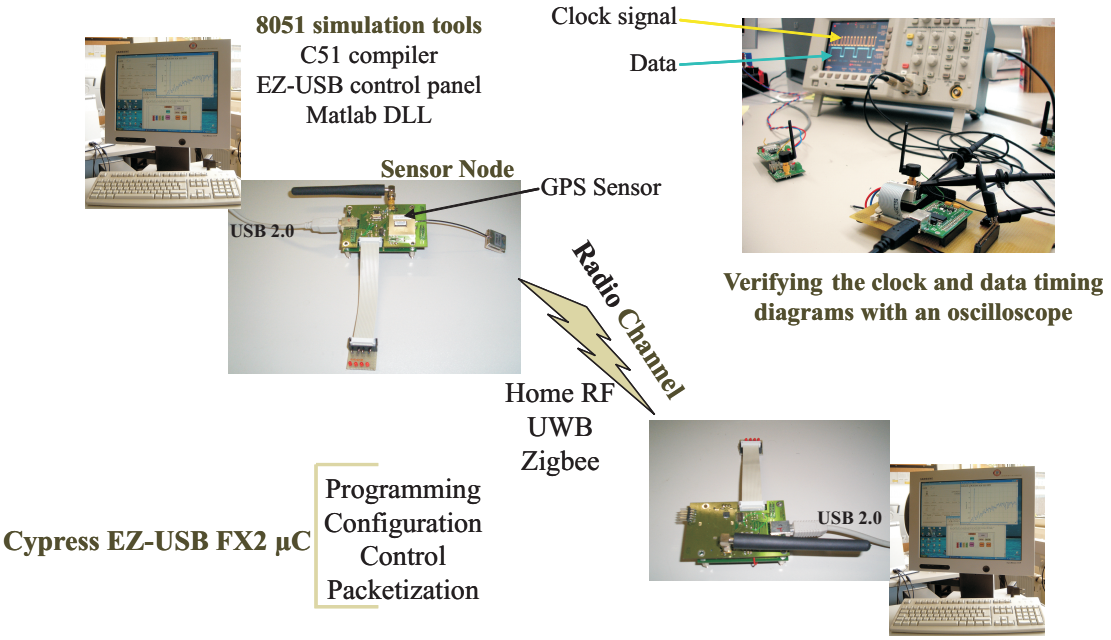

Figure 1: Experimental design of wireless sensor nodes

(Trimble Standard Interface Protocol) for faster acquisition - possibility to switch the module automatically to higher sensitivity when satellite signals are week - 12 channel simultaneous operation for complete position, velocity and time (PVT) solutions - supports standards NMEA (National Marine Electronics Association) 0183, TSIP, TAIP (Trimble ASCII Interface Protocol) and Differential GPS (DGPS).
As an embedded design, the *Lassen*® IQ GPS module provides direct CMOS compatible TTL level serial I/O. The RX and TX signals are driven directly by the dual universal asynchronous receiver/transmitter (UART) on the *Lassen*® IQ GPS receiver. Interfacing these signals directly to the UART of our 8051-Microcontroller provides direct serial communication without the complication of RS-232 or RS-422 line drivers.

2. *The NMEA Protocol*
The hardware interface for GPS units is designed to meet the NMEA requirements. The *Lassen*® IQ GPS receiver normally operates using one of the three protocols - TSIP, TAIP or NMEA 0183. Our program to dissect the desired GPS message string and extract the required information is based on the NMEA 0183 which is an industry standard protocol common to marine applications. The signal characteristics of NMEA 0183 serial data transmission are: Baud rate=4800, Data bits=8, Stop bits=1, Parity bits=none.
The entire protocol encompasses over 50 messages, but only a subset of these messages apply to a particular GPS receiver. Indeed, at 4800 baud we can only send 480 characteres per seconds. Since NMEA 0183 messages can have up to 79 characters,

we are limited to 6 different messages.

3. *Dissection of the desired GPS message*
   The NMEA protocol is designed to run as a process in the background spitting out messages which are then captured as needed by a program. Thus our program, written in C51, will sample the data stream, use that data for screen display, and then sample the data again, based on our information requirements. Depending on the time needed to use the data there can be easily a lag of 4 seconds in the responsiveness to changed data.
   As an example, a dissected NMEA message structure, based on some GPS measurements (June 11th 2005) at ZESS is shown and explained below:

   `$ GPGGA,215354.463,5054.2113,N,00801.7561, E,1,07,1.1,370.4,M,,,1.1, 0000*2A`

   The "$" sign indicates the start of a message.
   The GP talker identification signifies a GPS source (source of navigation information.
   The GGA message identification describe the message content and the number and order of the data fields. GGA describes the Global Positioning System fixed data
   The "," serve as delimiters for the data fields.
   215354.463 is a specific data field in the GPGGA message. In fact it describes the UTC Time given as 21h53mn54.463s. The other following fields describe, respectively, the latitude, the North/South indicator, the longitude, the East/West indicator, the position fix indicator, the satellites used (Range 0 to 12), the Horizontal Dilution of Precision (HDOP), the Mean Sea Level (MSL) altitude, the unit used (M=meters).
   0000 is the differential referential station ID.
   The "*" sign serves as a checksum delimiter and 2A are the two ASCII characters which indicates the hexadecimal value of the checksum.
   Not seen in the message above are the carriage return [CR] and line feed [LF] whose combination terminate the message.

4. *Extraction of the required information*
   Upon dissection of the required GPS message, our C51 program extract the desired fields of interest (UTC Time, Position etc...) and store the data in dedicated buffers for further use including data display, localization solutions, Aided GPS experiments, emulation of position-based routing algorithms, etc...
   The algorithm flowchart for extracting the required position information is shown in Fig. 2.

Communication Radio Module - Personal Computer

A dynamic-link library (DLL) named `USB_HRF_DLL` and its corresponding source-code for the microcontroller were developed with the objective of enabling a relatively simple communication capability between the Home RF hardware and a Personal Computer (PC) via the USB interface. Since the USB Framework in the microcontroller exhibits a relatively complex interrupt processing system, it was advantageous to make a change on the hardware. This concerns the Interrupt signal INT0 for signaling that Home RF has received data. This was set to INT5 (Trigger_in). This change is absolutely necessary for the signaling of a receive packet to occur.

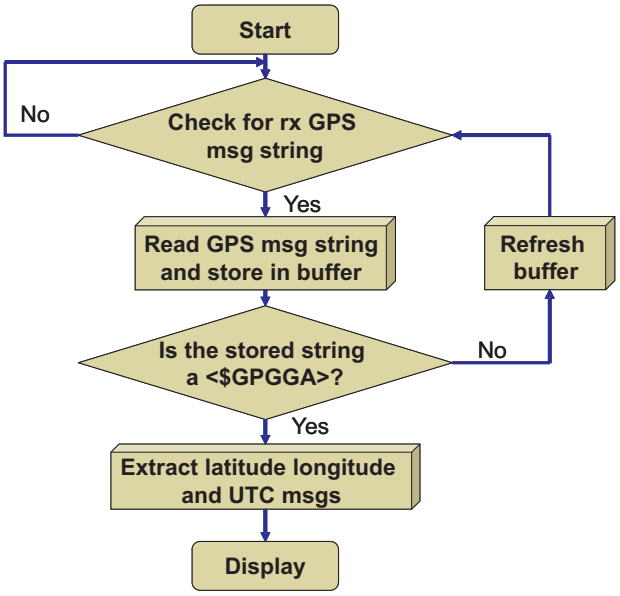

Figure 2: Algorithm flowchart

A special driver for the USB system must be installed. It can be found in the folder `Treiber_USB_CAM` of the provided CD. Loading the DLL and corresponding microcontroller programs, will allow the so-called renumeration to take place. This causes the PC to detect the microcontroller as a new sensor interface. It is important noting that the hardware and the DLL can be utilized fully only after the driver is correctly installed.

Two types of DLL can be exported, one for use under Matlab (Macro "Matlab" in `USB_HRF_DLL.h`) and the other one under C++. Using the Matlab environment, the program `HomeRF_Matlab.m` was written as a test-program which depicts the DLL principal functionality.

Home RF Functionalities

The DLL and the programs which run on the microcontroller are closely interrelated to each other. Each exported DLL function calls certain functions in the microcontroller via the USB Protocol. Thus it is possible for the source code of the microcontroller to adapt itself to new tasks without knowledge of the USB protocols or the entire USB Frameworks. The basic idea in implementing the functions in the microcontroller is to try to separate the USB specific functions from the Home RF functions. In this way, for any user of the DLL and the frameworks in the microcontroller, only two files are important: `HRF.c` and `HRF.h`. Both can be found in the directory `.../Config_USB_HRF/Control8051` (see provided CD), including also all relevant functions addressed by the HomeRF radio module. The block diagram in Fig. 3 shows the communication between the Home RF device, the microcontroller, the DLL and the software application.

For the communication between the DLL and the Home RF hardware via the microcontroller four DLL functions with different tasks are provided:

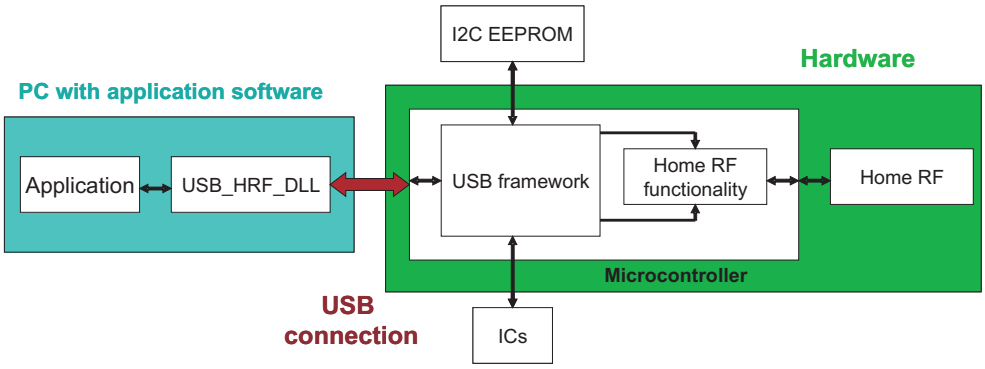

Figure 3: Interaction between the application and the microcontroller functions used by the radio module.

- `USB_Dll_HRF_Set_Config`: this function allows for the configuration settings to be sent to the Home RF device (length of data payload, address width, destination address for received data, enable/disable cyclic redundancy check (CRC), communication mode (Direct or ShockBurst^{TM}), RF data rate, crystal frequency, RF output power, frequency channel and receive/transmit operation).

- `USB_Dll_HRF_Transfer_Data`: this function allows the Home RF radio module to operate in Active Receive/Transmit modes (Direct or ShockBurst^{TM}). The ShockBurst technology uses on-chip FIFO (First In, First Out) to clock in data at a low data rate and transmit at a high rate (1 Mbps) thus enabling extremely power reduction. In direct mode the radio module functions like a traditional RF device. Data must be sent at 1Mbps or 250kbps at low data rate setting, for the receiver to detect the signals.

- `USB_Dll_HRF_Receive_Init`: this function prepares the microcontroller programs to accept data from the Home RF chip, at the rising edge of the DR signal, and to store it internally. No data are passed on to the DLL and thus to the PC.

- `USB_Dll_HRF_Receive_Data`: this function allows to read in the received data via the DLL.

These four DLL functions are related to the following three functions:
`HomeRF_Set_Config`, `HomeRF_Transmit_Data` and `HomeRF_Receive_Data` in the microcontroller, as shown in Fig. 4. When the exported functions of the DLL are called (through the framework of the microcontroller), the necessary Home RF functions belonging to them are activated.

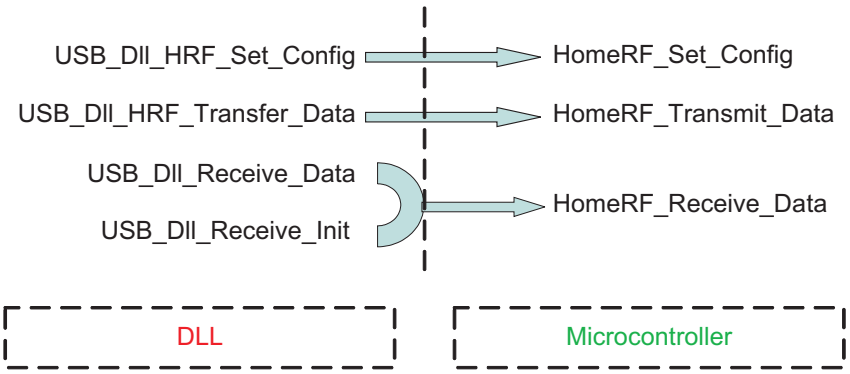

Figure 4: Relation between the DLL functions and the HomeRF functions in the microcontroller

List of Publications

Journal Papers

1. **G.F. Tchere**, P. Ubolkosold, S. Knedlik, O. Loffeld., "*Timing Offset Estimation for Transmitted-Reference Impulse Radio UWB Systems*", IEEE Journal of Communications and Networks, submitted October 2008.

Conference Papers

1. P. Ubolkosold, **G. F. Tchere**, S. Knedlik, O. Loffeld, "*A New Closed-Form Frequency Estimator in the Presence of Fading-Induced Multiplicative Noise*", 67th IEEE Vehicular Technology Conference, Singapore, May 2008.

2. P. Ubolkosold, **G. F. Tchere**, S. Knedlik, O. Loffeld, "*An Improved Frequency Offset Estimator for SIMO-OFDM with Maximum Estimation Range*", 67th IEEE Vehicular Technology Conference, Singapore, May 2008.

3. P. Ubolkosold, **G.F. Tchere**, S. Knedlik, O. Loffeld, "*Simple Carrier Frequency Offset Estimators in Frequency Flat-fading Channels*", IEEE International Conference on Communications (ICC 2007), Glasgow, Scotland, June 2007.

4. **G.F. Tchere**, P. Ubolkosold, S. Knedlik, O. Loffeld, "*Bit Error Performance of Differential Impulse Radio UWB systems*", 65th IEEE Vehicular Technology Conference, VTC Spring 2007, Dublin, Ireland, April 2007.

5. **G.F. Tchere**, P. Ubolkosold, S. Knedlik, O. Loffeld, "C*ommunication and Localization in Wireless Sensor Networks using Differential Impulse Radio UWB systems*", 4th Workshop on Positioning, Navigation and Communication (WPNC 2007), Hannover, Germany, March 2007.

6. **G.F. Tchere**, P. Ubolkosold, S. Knedlik, O. Loffeld, "*Bit Error Performance of UWB Differential Transmitted Reference systems*", IEEE International Symposium on Communications an Information Technologies (ISCIT), Bangkok, Thailand, October 2006.

7. **G.F. Tchere**, P. Ubolkosold, S. Knedlik, O. Loffeld, K. Witrisal, "*Data-Aided Timing Acquisition in UWB Differential Transmitted Reference systems*", IEEE International Symposium on Personal, Indoor and Mobile Radio Communications (PIMRC), Helsinki, Finland, September 2006.

8. P. Ubolkosold, **G.F. Tchere**, S. Knedlik, O. Loffeld, "*Nonlinear Least-Squares Frequency Offset Estimation and its Simplified Versions for Flat fading Channels* ", IEEE International Symposium on Communications an Information Technologies (ISCIT), Bangkok, Thailand, October 2006.

9. P. Ubolkosold, **G.F. Tchere** S. Knedlik , O. Loffeld, "*Data-Aided Joint estimation of Phase and Doppler Parameters using an Extended Kalman Filter*", IEEE International Symposium on Control, Communications and Signal Processing (ISCCSP 2006), Marrakech, Morocco, March 2006.

10. P. Ubolkosold, O. Loffeld, S. Knedlik, **G.F. Tchere**, "*A Robust Data-Aided Frequency Offset Estimation for Single Frequency Signals* ", IEEE Sarnoff Symposium, Princeton, New Jersey, USA, 2006

Bibliography

[1] FCC, "First report and order: In the matter of revision of part 15 of the commission's rules regarding ultra-wideband transmission systems," FCC, Tech. Rep. 02-48, April 2002.

[2] T. W. Barret, "History of ultra-wideband (UWB) radar & communications: pioneers and innovators," *Progress In Electromagnetics Symposium 2000*, July 2000.

[3] T. E. McEwan, "Ultra-wideband radar motion sensor," US Patent 5,361,070, November 1994.

[4] Electronic Communications Committee (ECC), "ECC decision of 2006 on the harmonized conditions for the use of UWB devices below 10.6 ghz," ECC, Tech. Rep., September 2005.

[5] H. Schantz; and L. Fullerton, "The diamond dipole: A gaussian impulse antenna," *Proceedings IEEE Int. Symposium Antennas and Propagation Society*, vol. 4, pp. 100–103, 2001, Boston, MA.

[6] R. A. Scholtz; "Multiple access with time-hopping impulse modulation," *Proceedings IEEE Military Communications Conference, MILCOM 1999*, pp. 447–450, 1993, boston,MA.

[7] H. Zhang; and T. Gulliver, "Biorthogonal pulse position modulation for time-hopping multiple access UWB communications," *IEEE Trans. on Wireless Communications*, vol. 4, no. 3, pp. 1154 – 1162, May 2005.

[8] M. Z. Win; and R. A. Scholtz, "Ultra wide bandwidth time-hopping spread-spectrum impulse radio for wireless mutiple access communications," *IEEE Trans. on Communications*, vol. 48, no. 4, pp. 679–691, 2000.

[9] S. Gecizi; Z. Tian; G. B. Giannakis; H. Kobayashi; A. F. Molisch, H. V. Poor; and Z. Sahinoglu, "Localization via ultra-wideband radios: a look at positioning aspects for future sensor networks," *IEEE Signal Processing Magazine*, vol. 22, no. 4, pp. 70–84, July 2005.

[10] L. Yang; and G. Giannakis, "Ultra-wideband communications: an idea whose time has come," *IEEE Signal Processing Magazine*, vol. 21, no. 6, pp. 26–54, November 2004.

[11] J. Taylor, *Ultra Wideband Radar Technology.* New York: CRC Press, 2001.

[12] I. Opperman; M. Hämäläinen; and J. Iinatti, *UWB Theory and Applications.* Wiley, 2004.

[13] J. Borras; P. Hatrack; and N. B. Mandayam, "Decision theoretic framework for NLOS identification," *48th IEEE Vehicular Technology Conference*, vol. 2, pp. 1583 – 1587, July 1998, Ottawa, Canada.

[14] H. Shimizu; H. Masui; M. Ishii; and K. Sakawa, "LOS and NLOS path-loss and delay characteristics at 3.35 GHz in a residential environment," *IEEE Antennas and Propagation Society International Symposium*, vol. 2, pp. 1142 – 1145, 2000.

[15] K. Witrisal; G. Leus; M. Pausini; and C. Krall, "Equivalent system model and equalization of differential impulse radio UWB systems," *IEEE Journal Selected Areas in Communications*, vol. 23, no. 9, pp. 1851 – 1862, September 2005.

[16] V. Mathews; and G. Sicuranza, *Polynomial Signal Processing.* New York: Wiley, 2000.

[17] T. G. Stockham Jr., "Image processing in the context of a visual model," *Proceedings of the IEEE*, vol. 60, no. 7, pp. 828 – 842, July 1972.

[18] J. Astola; and P. Kuosmanen, *Fundamentals of Nonlinear Digital Filtering.* Boca Ranta, New York: CRC Press, 1997.

[19] L. Yin; R. Yang; M. Gabbouj; and Y. Neuvo, "Weighted median filters: a tutorial," *IEEE Transaction on Circuits and Systems II: Analog Digital Signal Processing*, vol. 43, no. 3, pp. 157 – 192, March 1996.

[20] J. Serra, "Introduction to mathematical morphology," *Computer Vision, Graphics Image Processing*, vol. 35, pp. 283 – 305, 1986.

[21] P. Maragos; and R. W. Schafer, "Morphological skeleton representation and coding of binary images," *IEEE Transactions on Acoustics Speech and Signal Processing*, vol. ASSP-34, no. 5, pp. 1228 – 1244, October 1986.

[22] S. Haykin, *Neural Networks.* Macmillan, 1993.

[23] W. J. Rugh, *Nonlinear System theory. The Volterra-Wiener Approach.* Baltimore, Maryland: Johns Hopkins University Press, 1981.

[24] E. Eskinat; S. H. Johnson; and W. L. Luyben, "Use of Hammerstein models in identification of nonlinear systems," *AIChE Journal*, vol. 37, no. 2, pp. 255 – 268, 1991.

[25] W. Greblicki, "Nonparametric identification of Wiener systems by orthogonal series," *IEEE Transactions on Automatic Control*, vol. 39, no. 10, 1994.

[26] T. Wigren, "Convergence analysis of recursive identification algorithms based on the nonlinear Wiener model," *IEEE Transactions on Automatic Control*, vol. 39, no. 11, pp. 2191–2206, November 1994.

[27] N. J. Bershad; P. Celka and S. McLaughlin, "Analysis of stochastic gradient identification of Wiener-Hammerstein systems for nonlinearities with hermite polynomial expansions," *IEEE Transactions on Signal Processing*, vol. 49, 2001.

[28] M. Pottmann; and R. K. Pearson, "Block-oriented NARMAX models with output multiplicities," *AIChE Journal*, vol. 44, pp. 131 – 140, 1998.

[29] J. C. Stapleton; and S. C. Bass., "Adaptive noise cancellation for a class of nonlinear dynamic reference channels," *IEEE Transactions on Circuits and Systems*, vol. CAS-32, pp. 143 – 150, February 1985.

[30] K. P Fruzzetti; A. Palazoglu; and K. McDonald, "Nonlinear model predictive control using Hammerstein models," *Journal of Process Control*, vol. 7, no. 1, pp. 31 – 41, 1997.

[31] W. C. Jakes Jr., *Microwave Mobile Communications*. New York: Wiley-Interscience, 1974.

[32] K. Witrisal, "OFDM air-interface design for wireless multimedia communications," Ph.D. dissertation, Delft University of Technology, April 2002.

[33] T. S. Rappaport, *Wireless Communications: Principles and Practice*. Upper Saddle River: Prentice-Hall, 1996.

[34] S. A. Mohamed; G. Lœvnes; E. Antonsen; R. Rækken; B. Nigeon; and J. J. Reis, "Report on propagation measurements," RACE Central Office, European Commission, Brussels, Tech. Rep. Deliverable R2067/BTL/2.2.2/DS/P/ 035.b1, December 1994, RACE 2067.

[35] A. M. Saleh; and R. Valenzuela, "A statistical model for indoor multipath propagation," *IEEE Journal Selected Areas in Communications*, vol. 5, no. 2, pp. 128 – 137, February 1987.

[36] J. Foerster, "Channel modeling sub-committee report final," IEEE P802.15 working group for WPAN, Tech. Rep. P802.15-02/368r5-SG3a, October 2002.

[37] A. F. Molisch; K. Balakrishnan; C. Chong; S. Emami; A. Fort; J. Karedal; J. Kunisch; H. Schantz; U. Schuster; and K. Siwiak, "IEEE 802.15.4a channel model-final report," IEEE 802.15.4a channel modeling subgroup, Tech. Rep. IEEE 802.15.4a 04/662r0, November 2004.

[38] G. Kadel; and R. Lorenz, "Impact of the radio channel on the performance of digital mobile communication systems," *Sixth IEEE Int. Symp. on Personal, Indoor and Mobile Radio Communications PIMRC95*, p. 419423, 1995.

[39] R. Qiu; and I. Lu, "Multipath resolving with frequency dependence for broadband wireless channel modeling," *IEEE Transactions on Vehicular Technology*, vol. 48, no. 1, pp. 273 – 285, January 1999.

[40] G. L. Stueber, *Principles of Mobile Communication.* Kluwer, 1996.

[41] T. Quek; and M. Win, "Ultrawide bandwidth transmitted-reference signaling," *IEEE Int. Conference on Communications*, vol. 6, pp. 3409 – 3413, June 2004.

[42] M. Weisenhorn; and W. Hirt, "Robust non-coherent receiver exploiting UWB channel properties," *IEEE Trans. on Communications*, pp. 156–160, May 2004.

[43] R. Hoctor; and H. Tomlinson, "Delay-hopped transmitted-reference RF communications," *Proc. IEEE Conference on UWB Systems and Technologies*, pp. 265 – 270, May 2002.

[44] Y. Chao; and R. Scholtz, "Optimal and suboptimal receivers for ultra-wideband transmitted reference systems," *IEEE Global Telecommunications Conference, GLOBECOM'03*, vol. 2, pp. 759–763, December 2003.

[45] S. Franz; and U. Mitra, "Generalized UWB transmitted reference systems," *IEEE Journal on Selected Areas in Communications*, vol. 24, no. 4, pp. 780–786, April 2006.

[46] S. Gecizi; F. Tufvesson; H. Poor and A. Molisch, "On the performance of transmitted-reference impulse radio," *IEEE Signal Processing Magazine*, pp. 2874–2879, December 2004.

[47] T. Quek; and M. Win, "Analysis of UWB transmitted-reference communication systems in dense multipath channels," *IEEE Journal on Selected Areas in Communications*, vol. 23, no. 9, pp. 1863 – 1874, September 2005.

[48] J. Romme; and K. Witrisal, "Transmitted-reference UWB systems using weighted autocorrelation receivers," *IEEE Transactions on Microwave Theory and Techniques*, vol. 54, no. 4, pp. 1754–1761, June 2006.

[49] T. Zasowksi; F. Althaus; and A. Wittneben, "An energy efficient transmitted-reference scheme for performance analysis for ultra-wideband communications," *Proceedings IEEE Joint UWBST & IWUWBS conferences*, no. 146-150, pp. 780–786, May 2004, Kyoto, Japan.

[50] K. Witrisal; M. Pausini; and A. Trindade, "Multiuser interference and inter-frame interference in UWB transmitted reference systems," *Proceedings IEEE Joint UWBST & IWUWBS Conferences*, pp. 96 – 100, May 2004, Kyoto, Japan.

[51] K. Witrisal; and Y. Alemseged, "Narrowband interference mitigation for differential UWB systems," *Proceedings Asimolar Conf. Signals, Systems and Computers*, October 2005, Pacific Grove, CA.

[52] K. Witrisal; and M. Pausini, "Statistical analysis of transmitted-reference UWB systems on multipath channels," *IEEE Int. Conference on Ultra-Wideband*, pp. 303 – 308, September 2006.

[53] S. Franz; and U. Mitra, "Integration interval optimization and performance analysis for UWB transmitted reference systems," *IEEE Journal on Selected Areas in Communications*, pp. 26 – 30, May 2004, Kyoto, Japan.

[54] J. Romme; and K. Witrisal, "Oversampled weighted autocorrelation receivers for transmitted-reference uwb systems," *IEEE Vehicular Technology Conference*, vol. 2, pp. 1375 – 1380, June 2005, Stockholm, Sweden.

[55] J. Choi; and W. Stark, "Performance of ultra-wideband communications with suboptimal receivers in multipath channels," *IEEE Journal on Selected Areas in Communications*, vol. 20, no. 9, pp. 1754 – 1776, December 2002.

[56] S. Kay, *Fundamentals of Statistical Processing, Volume II: Detection Theory.* Prentice Hall, Februar 1998.

[57] G. F. Tchere; P. Ubolkosold; S. Knedlik; and O. Loffeld, "Bit error performance of differential impulse radio UWB systems," *IEEE Vehicular Technology Conference*, pp. 1569 – 1573, April 2007, Dublin, Ireland.

[58] B. Denis; J.-B. Pierrot; and C. Rjeily, "Joint distributed synchronization and positioning in UWB ad hoc networks using TOA," *IEEE Trans. on Microwave Theory and Techniques, Special issue on Ultrawideband*, vol. 54, no. 4, pp. 1896 – 1911, June 2006.

[59] Z. Tian; and G. Giannakis, "BER sensitivity to mistiming in ultrawideband impulse radios - part II: fading channels," *IEEE Trans. on Signal Processing*, vol. 53, no. 5, pp. 1897 – 1907, May 2005.

[60] R. Blazquez; M. Newaskar; and A. Chandrakasan, "Coarse acquisition for UWB digital receivers," *IEEE Intl. Conf. Acoustics, Speech and Signal Processing*, vol. 4, pp. 137 – 140, April 2004.

[61] J. Furukawa, Y. Sanada; and T. Kuroda, "Novel initial acquisition scheme for impulse-based UWB systems," *proc. Intl. Workshop UWB Systems*, pp. 278 – 282, May 2004.

[62] S. Gecizi; E. Fishler; H. Kobayashi; H. Poor; and A. Molisch, "A rapid acquisition technique for impulse radio," *Proceedings Pacific Rim Comm., Comp. and Signal Processing*, pp. 627 – 630, August 2003.

[63] S. Soderi; J. Iinatti, and M. Hamalainen "CLPDI algorithm in UWB synchronization," *Intl. Workshop on UWB Systems*, pp. 759 – 763, November 2003.

[64] S. Vijayakumaran; T. Wong; and S. Aedudodla, "On the asymptotic performance of threshold-based acquisition systems in multipath fading channels," *IEEE Information Theory Workshop*, 2004, San Antonio.

[65] H. Zhang; S. Wei; D. L. Goeckel; and M. Win, "Rapid acquisition of ultra-wideband radio signals," *36th Asimolar Conference on Signals, Systems and Computers*, vol. 1, pp. 712 – 716, November 2002.

[66] C. Carbonelli; U. Mengali; and U. Mitra, "Synchronization and channel estimation for UWB signals," *IEEE Global Telecommunications Conference, GLOBECOM'04*, vol. 6, pp. 764 – 768, December 2003.

[67] Z. Tian; L. Yang; and G. Giannakis, "Symbol timing estimation in ultrawideband communications," *Proceedings Asimolar Conference on Signals, Systems and Computers*, pp. 1924–1928, 2002.

[68] Z. Tian; and G. Giannakis, "A GLRT approach to data-aided timing acquisition in UWB radios-part I: Algorithms," *IEEE Trans. Wireless Communications*, vol. 4, no. 6, pp. 2956 – 2967, November 2005.

[69] L. Yang; Z. Tian; and G. Giannakis, "Non-data aided timing acquisition of ultra-wideband transmissions using cyclostationarity," *IEEE Intl. Conference Acoustics, Speech and Signal Processing*, vol. 4, pp. 121 – 124, 2003.

[70] L. Yang; and G. Giannakis, "Timing ultra-wideband signals with dirty templates," *IEEE Transaction on Communications*, vol. 53, no. 11, pp. 1952 – 1963, November 2005.

[71] G. F. Tchere; P. Ubolkosold; S. Knedlik; O. Loffeld; and K. Witrisal, "Data-aided timing acquisition in UWB differential transmitted reference systems," *17th International Symposium on Personal, Indoor and Mobile Radio Communications*, pp. 1 – 5, September 2006, Helsinki, Finland.

[72] S. Kay, *Fundamentals of Statistical Processing, Volume I: Estimation Theory*. Prentice Hall Signal Processing Series, April 1993, vol. I.

[73] P. Lancaster; and K. Salkauskas, *Curve and Surface Fitting: An Introduction*. London: Academic Press, 1986.

[74] G. Kadel; and R. Lorenz, "Curve fitting made easy," *Industrial Physicist*, vol. 9, pp. 24 – 27, April/May 2003.

[75] R. J. Fontana; E. Richley; and J. Barney, "Commercialization of an ultra wideband precision asset location system," *Proc. IEEE Conference on UWB Systems and Technologies*, 2003.

[76] J. Schroeder; S. Galler; and K. Kyamakya, "A low-cost experimental ultra-wideband positioning system," *IEEE International Conference on Ultra-Wideband*, pp. 632 – 637, September 2005.

[77] M. Mauve; J. Widmer; and H. Hartenstein, "A survey on position based routing in mobile ad-hoc networks," *IEEE Network Magazine*, vol. 15, pp. 30 – 39, November 2001.

[78] W. Horie; and Y. Sanada, "Novel packet routing scheme based on location information for UWB ad-hoc network," *Proc. IEEE Conference on UWB Systems and Technologies*, pp. 185 – 189, November 2003.

[79] L. De Nardis; G. Giancola; and M.-G. D. Benedetto, "A position based routing strategy for UWB networks," *Proc. IEEE Conference on UWB Systems and Technologies*, pp. 185 – 189, November 2003.

[80] N. Bulusu; J. Heidemann; and D. Estrin, "GPS-less low-cost outdoor localization for very small devices," *IEEE Personal Communications Magazine*, vol. 7, no. 5, p. 28 34, October 2000.

[81] K. Langendoen; and N. Reijers, "Distributed localization in wireless sensor networks: a quantitative comparison," *Int. Journal of Computer and Telecommunications Networking*, vol. 43, no. 4, pp. 499 – 518, November 2003.

[82] D. Niculescu; and B. Nath, "Ad hoc positioning system," *IEEE Global Telecommunications Conference, GLOBECOM*, vol. 5, pp. 2926 – 2931, 2001.

[83] C. Savarese; J. M. Rabaey; and K. Langendoen, "Robust positioning algorithms for distributed ad-hoc wireless sensor networks," *USENIX Annual Technical Conference*, pp. 317 – 327, June 2002.

[84] A. Savvides; H. Park; and M. B. Srivastava, "The bits and flops of the n-hop multilateration primitive for node localization problems," *Proc. of the 1st ACM int. workshop on Wireless sensor networks and applications*, pp. 317 – 327, September 2002, Atlanta, Georgia, USA.

[85] J. Abel; and J. Smith, "The spherical interpolation method for closed-form passive source localization using range difference measurements," *IEEE International Conference on Acoustics, Speech, and Signal Processing, ICASSP*, vol. 12, pp. 471 – 474, April 1987.